Research Square

Preprints are preliminary reports that have not undergone peer review.
They should not be considered conclusive, used to inform clinical practice,
or referenced by the media as validated information.

Fc_{95}, a next-generation Fc variant, achieves exceptional ADCC potency by linking affinity enhancement to intrinsic afucosylation

longlong Luo

luolong_long@126.com

Institute of Basic Medical Sciences

Yangyihua Zhou

State Key Laboratory of National Security Specially Needed Medicines

Yaowei Ma

State Key Laboratory of National Security Specially Needed Medicines

Yi Zhou

Department of Neurosurgery, the First Medical Center of Chinese PLA General Hospital, Beijing 100853, China

Min Zhang

College of Life and Environmental Sciences, Minzu University of China, Beijing, 100081, China.

Ning Shi

Xiangya School of Basic Medical Sciences, Central South University, Changsha, 410078, China.

Pinnan Zhao

State Key Laboratory of National Security Specially Needed Medicines, Beijing 100039, China.

Liang Zhang

State Key Laboratory of National Security Specially Needed Medicines, Beijing 100039, China.

Chaoyan Yao

Xiangya School of Basic Medical Sciences, Central South University, Changsha, 410078, China.

Juan Tian

Hunan Normal University School of medicine, Changsha, 410200, China.

Chunxia Qiao

Institute of Immunology, Henan University

Xinying Li

Institute of Basic Medical Sciences

Guojiang Chen

Beijing Institute of Pharmacology and Toxicology

Yuting Zhang

Inner Mongolia Key Lab of Molecular Biology, School of Basic Medical Sciences, Inner Mongolia Medical University, Hohhot, Inner Mongolia 010058, P. R. China

Jiannan Feng
Institute of Basic Medical Sciences

Xiang Gao
Beijing Institute of Biotechnology, Beijing, 100071, China.

Article

Keywords: Fc engineering, ADCC, afucosylation, glycosylation, NK cells, immunotherapy, protein design, tumor microenvironment

Posted Date: June 15th, 2026

DOI: https://doi.org/10.21203/rs.3.rs-9897374/v1

License: This work is licensed under a Creative Commons Attribution 4.0 International License.
Read Full License

Additional Declarations: (Not answered)

Fc_{95}, a next-generation Fc variant, achieves exceptional ADCC potency by linking affinity enhancement to intrinsic afucosylation.

Authors: Yangyihua Zhou[1,†], Yaowei Ma[1,†], Yi Zhou[3], Min Zhang[1,4], Ning Shi[1,5], Pinnan Zhao[1], Liang Zhang[1], Chaoyan Yao[1,5], Juan Tian[1,6], Chunxia Qiao[1], Xinying Li[1], Guojiang Chen[1], Yuting Zhang[1], Xiang Gao[1,2*], Jiannan Feng[1,*], Longlong Luo[1,*].

†These authors made equal contributions to this work.

*Corresponding authors. Email: gaoxiang609@163.com (X.G.); fengjiannan1970@qq.com (J.N.F); luolong_long@126.com (L.L.L.). **Lead Contact:** Longlong Luo.

Affiliations:

[1]State Key Laboratory of National Security Specially Needed Medicines, Beijing 100039, China.

[2]Beijing Institute of Biotechnology, Beijing, 100071, China.

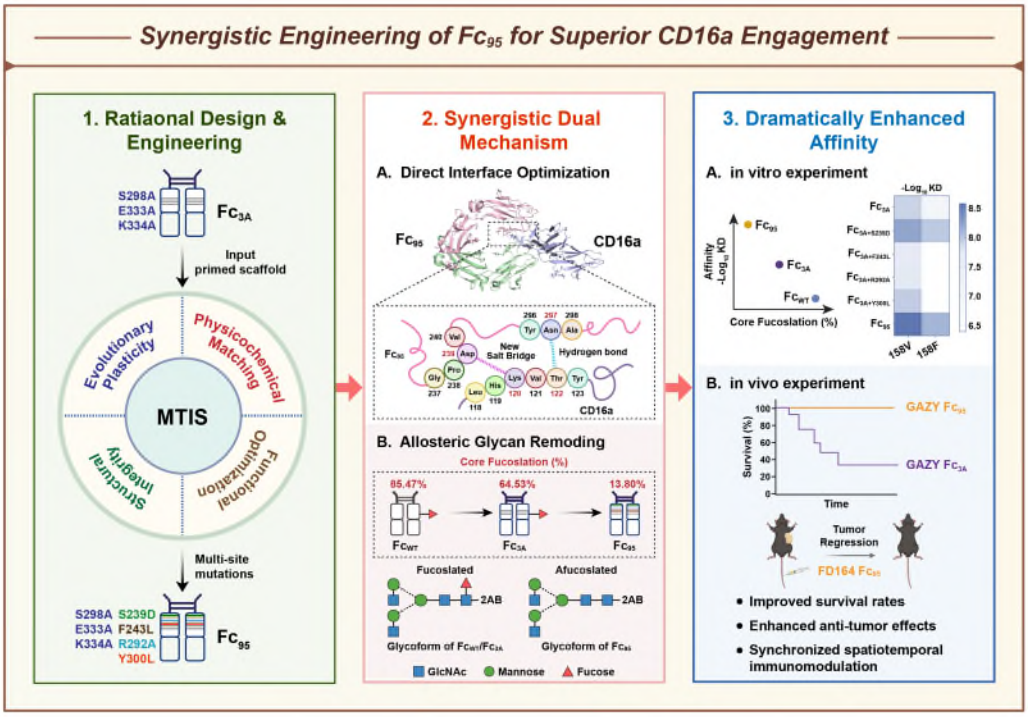
[3]Department of Neurosurgery, the First Medical Center of Chinese PLA General Hospital, Beijing 100853, China.

[4]College of Life and Environmental Sciences, Minzu University of China, Beijing, 100081, China.

[5]Xiangya School of Basic Medical Sciences, Central South University, Changsha, 410078, China.

[6]Hunan Normal University School of medicine, Changsha, 410200, China.

Graphical abstract



The MTIS (Microenvironment-Tuned Interface Sculpting) design strategy is used to rationally engineer the Fc variant Fc_{95} for superior CD16a engagement. This approach creates a synergistic dual mechanism: direct interface optimization *via* new atomic contacts and localized microenvironment tuning that intrinsically promotes afucosylation. Consequently, Fc_{95} exhibits dramatically enhanced binding affinity *in vitro*. This translates to superior anti-tumor efficacy and improved survival rates in a preclinical *in vivo* model, demonstrating a powerful method for engineering next-generation antibody therapeutics.

Abstract

Enhancing antibody-dependent cellular cytotoxicity (ADCC) is a central goal for immunotherapy, yet current strategies face a persistent engineering trade-off between potency, stability, and manufacturability. Here, we report Fc_{95}, an IgG1 Fc variant developed using Microenvironment-Tuned Interface Sculpting (MTIS), a design philosophy that systematically co-optimizes these competing parameters. This rational design process led to an unexpected and powerful discovery: a dual-action mechanism where four synergistic mutations not only directly remodel the FcγRIIIa binding interface for hyper-affinity, but also, through profound local physicochemical alterations, instruct the host cell's machinery to achieve near-complete afucosylation (<15% fucose). This effectively translates a complex cell-line engineering challenge into an elegant problem of protein sequence design. Across five molecular formats targeting oncology and infectious disease, Fc_{95} consistently surpassed clinical afucosylated antibodies and the Fc_{3A} variant, leading to potency gains of several orders of magnitude in primary cell assays and demonstrating superiority against both high- and low-affinity FcγRIIIa allotypes. *In vivo*, Fc_{95} conferred complete, durable protection in a disseminated lymphoma model and mediated robust tumor control and regression in solid tumor settings. Mechanistically, Fc_{95} acts as a pivotal regulator, inducing comprehensive reprogramming of the tumor microenvironment—driving NK and $CD8^+$ T cell infiltration, M1 macrophage polarization, and regulatory T cell depletion—more effectively than benchmark controls. By unifying intentional interface engineering with microenvironment-directed afucosylation, Fc_{95} emerges as a robust, manufacturable platform that resolves the long-standing efficacy-manufacturability trade-off, paving the way for next-generation immunotherapies.

Keywords: Fc engineering, ADCC, afucosylation, glycosylation, NK cells, immunotherapy, protein design, tumor microenvironment

Introduction

The clinical impact of therapeutic antibodies is significant and expanding, with applications spanning from oncology and autoimmunity to emerging frontiers in infectious, metabolic, and neurodegenerative diseases[1-6]. In many of these settings, efficacy is dictated by antibody effector functions, including antibody-dependent cell-mediated cytotoxicity (ADCC), antibody-dependent cellular phagocytosis (ADCP), and complement-dependent cytotoxicity

(CDC). These functions are mediated by the Fragment crystallizable (Fc) domain through its interaction with Fc gamma receptors (FcγRs) expressed on various immune effector cells[7-14]. The FcγR family comprises both activating and inhibitory receptors that tightly regulate immune responses. The key activating FcγRs include FcγRI (CD64) on monocytes and macrophages, FcγRIIa (CD32a) on myeloid cells such as macrophages and neutrophils, and FcγRIIIa (CD16a) primarily on natural killer (NK) cells and macrophages[14]. Conversely, immune activation is counterbalanced by the inhibitory receptor, FcγRIIb (CD32b), which is broadly expressed on B cells, macrophages, and dendritic cells. Among the various effector mechanisms, ADCC is often the most prominent driver of therapeutic efficacy, playing a critical role in both anti-tumor and anti-viral immune clearance[15-17]. ADCC is predominantly initiated by the binding of the antibody Fc domain to the activating receptor FcγRIIIa on NK cells. However, the net cytotoxic outcome is also heavily influenced by the inhibitory receptor FcγRIIb, making the ratio of activating-to-inhibitory (A/I) receptor binding a critical determinant of overall efficacy[18-20]. Among these receptors, the fucose-sensitive FcγRs are strictly limited to human FcγRIIIa and FcγRIIIb (expressed on neutrophils), as well as their mouse ortholog, FcγRIV[21]. The removal of core fucose (afucosylation) from the Fc N-glycan dramatically increases the binding affinity specifically to these receptors, thereby markedly enhancing ADCC potency. In addition, other glycan adducts, such as terminal galactosylation, can act synergistically with afucosylation to further modulate and optimize ADCC activity[22]. For decades, enhancing this Fc-FcγRIIIa interaction has been a major goal, representing a direct path to superior immunotherapies[16, 23-25]. However, this pursuit has historically split the field onto two parallel paths[26].

The first path, glycoengineering, eliminates core fucose from the Fc's N-glycan to substantially increase FcγRIIIa affinity[27-32]. While clinically validated by approved drugs like Gazyva® and Poteligeo®[28, 33-37], this gain in efficacy comes at the cost of manufacturing complexity, demanding proprietary, engineered cell lines that impose substantial cost and accessibility barriers. The alternative path, protein engineering, introduces targeted amino acid substitutions within the Fc domain to optimize the receptor-binding interface. Extensive efforts in rational design and directed evolution have generated a plethora of Fc variants—ranging from early foundational mutants (e.g., 'DI' and '3A')[38] to the clinically approved margetuximab[39-43]. Yet,

this strategy has remained a significant biophysical challenge, often limited by an affinity-stability trade-off where potent mutations often compromise developability and disrupt the finely tuned selectivity across other Fc receptors required for optimal pharmacokinetics and safety[44, 45].

To address the persistent affinity-stability trade-off in Fc engineering, we employed a rational design framework termed 'Microenvironment-Tuned Interface Sculpting' (MTIS). Rather than focusing on isolated mutations, MTIS treats the expansive Fc-FcγRIIIa binding surface as an integrated system, systematically modeling atomic-level polar and electrostatic networks to optimize receptor engagement while preserving thermodynamic stability and developability. Here, we describe the application of this structure-guided strategy to engineer novel Fc variants. Furthermore, through comprehensive biophysical and functional characterization of the resulting candidates, we sought to elucidate the precise mechanisms driving their enhanced ADCC activity. Notably, this investigation revealed an unanticipated interplay between the rationally designed protein backbone and intrinsic host-cell processing: specific conformational changes introduced by the mutations allosterically instructed standard CHO cells to produce highly afucosylated glycoforms. By detailing both the structural design process and this unexpected dual-mechanism phenomenon, we aim to provide a novel perspective on generating potent, ADCC-enhanced therapeutics without the need for specialized cell line engineering.

Results

MTIS Enables Rational Design of a Next-Generation Fc Variant with Superior Predicted Properties

A central challenge in therapeutic antibody engineering is the inherent trade-off between enhancing receptor affinity and maintaining protein stability and developability. To overcome this limitation, we implemented Microenvironment-Tuned Interface Sculpting (MTIS), a hierarchical computational-aided drug design (CADD) workflow. MTIS deconstructs the engineering challenge into a four-dimensional optimization framework: 1) Evolutionary Plasticity, to define a viable engineering canvas; 2) Physicochemical Matching, for structure-guided atomic-level sculpting; 3) Functional Optimization, to elicit superior effector activity; and 4) Structural Integrity, to preserve stability and developability.

The rational design of Fc-receptor interfaces relies on a detailed understanding of its interaction

hotspots. Previous studies on the Fc-FcγRIII complex[46-49], alongside extensive subsequent research[41, 50-52], have delineated these critical regions—primarily within the lower hinge (e.g., residues 234-239) and the proximal CH2 domain (e.g., 243, 265, 292, 297-298, 300, 330-334)—as essential for mediating CD16a binding, Visualized on the complex crystal structure (PDB: 1E4K) (Fig. 1A). Informed by this established map, we initiated our MTIS workflow by applying its first principle, Evolutionary Plasticity, which serves to define a viable engineering canvas. We selected the Fc_{3A} (S298A/E333A/K334A) variant as our initial scaffold. This choice was deliberate: the alanine substitutions effectively neutralize the native interaction landscape, removing specific steric and electrostatic features to reset the interface to a structurally permissive foundation, ideal for *de novo* interaction design.

Following scaffold selection, we transitioned to structure-guided rational design to quantify atomic-level mismatches within the Fc-FcγRIIIa complex (PDB: 1E4K). Our design strategy hierarchically prioritized the introduction of high-energy electrostatic interactions to drive affinity, while systematically optimizing short-range Van der Waals packing and minimizing desolvation penalties. Utilizing PyMOL, Discovery Studio, and PDBePISA, we analyzed interatomic distances, electrostatic potentials, and solvent accessible surface area (SASA) to identify specific "physicochemical liabilities" (Fig. S1A-B).

Structural interrogation revealed that the bulky F243 lacks stabilizing π-π interactions in its predominantly aliphatic microenvironment (Fig. 1B). Geometric measurements (with a *Cα-Cζ* distance of 5.1 Å) showed it exceeds the pocket's spatial capacity, causing suboptimal Van der Waals packing. To resolve this steric congestion, we introduced the F243L substitution. Leucine's streamlined side chain (with Cα-Cδ1 /Cδ2 distances of 3.9 Å and 3.1 Å, respectively) provides a superior geometric fit, reducing side-chain volumetric occupancy by 25.89% and optimizing local hydrophobic density (Fig. S1C). Similarly, the Y300 side chain buried an unsatisfied polar hydroxyl group within a hydrophobic pocket, incurring a significant desolvation penalty (Fig. S1D). The Y300L substitution eliminated this unpaired polar moiety and provided notable structural decompression. The original Y300 side chain extended ~6.5 Å from the backbone, while L300 reduced this to ~3.9 Å. This led to deeper burial (SASA decreased from 37.19 $Å^2$ to 9.68 $Å^2$) and formation of a dense hydrophobic cluster with ~12 carbon-atom contacts within 4.0 Å, enhancing structural enthalpy.

To further bolster interfacial affinity *via* long-range electrostatics, we introduced S239D. This charge-swap positions a de novo carboxylate group to bridge two prominent cationic centers on CD16a (K120 and K161), facilitating multivalent salt-bridge formation (Fig. 1B). Concurrently, the R292A mutation was implemented for structural de-bulking at the CH2–CH3 junction. Replacing the expansive native arginine with alanine drastically reduced the side-chain extension from ~7.3 Å to 1.5 Å (Fig. S1E). This eliminated spatial constraints and reconfigured the local topology to better accommodate the S239D carboxylate group.

Together, these four targeted mutations rationally assembled onto the Fc_{3A} scaffold constitute the Fc_{95} variant (Fig. 1C). While these individual point mutations have been previously reported[38], their synergistic combination and comprehensive functional validation represent a novel optimization of interface complementarity.

Crucially, to ensure the viability of our sculpted interface, we returned to the foundational principle of Evolutionary Plasticity. The ConSurf analysis (Fig. 1D) acted as an orthogonal validation, confirming that all targeted residues (239, 243, 292, 300) occupy an intermediate conservation state (scores 3-7). This ensured our modifications were focused on regions malleable enough for functional gain without compromising the deeply conserved structural architecture of the Fc domain.

The subsequent stages of the MTIS framework served to rigorously validate our design *in silico* against its final two pillars. To assess Functional Optimization, molecular dynamics simulations predicted a profound energetic advantage. The calculated binding free energy (ΔG) for the Fc_{95}-CD16a complex was -250.7 kJ/mol, a quantum leap in predicted affinity over both Fc_{WT} (-179.1 kJ/mol) and the parent Fc_{3A} scaffold (-167.9 kJ/mol) (Fig. 1E). This energetic gain translated into a remarkably stable complex, exhibiting minimal RMSD fluctuations around a tight equilibrium ($\approx$ 0.2-0.4 nm) (Fig. S1F). In parallel, to assess Structural Integrity, we calculated the change in folding free energy ($\Delta\Delta G$) for the Fc_{95} monomer, which was negligible ($\approx$ 0.5 kJ/mol) (Fig. 1F). This result is central to our thesis, demonstrating that the MTIS framework successfully decouples affinity enhancement from the degradation of intrinsic stability—a long-standing goal in the field.

Finally, we conducted a comprehensive developability and risk mitigation assessment, a key component of the Structural Integrity pillar. Immunogenicity predictions revealed no creation

of novel linear B-cell epitopes (Fig. 1G) and, more significantly, predicted a reduced conformational epitope surface for Fc_{95} relative to its Fc_{3A} precursor (Fig. S1G). T-cell epitope analysis against representative high-prevalence MHC alleles confirmed that the engineered mutations did not introduce any significant liabilities, with predicted binding affinities remaining unchanged or even slightly reduced (Fig. S1H–I). Furthermore, we assessed aggregation propensity, a critical developability parameter. The computed Na4vSS scores for Fc_{WT}, Fc_{3A}, and Fc_{95} were -7.6, -6.4, and -6.7, respectively (Fig. 1H). This data is revealing: the modest increase in aggregation risk is explicitly attributed to the E333A/K334A substitutions inherited from the Fc_{3A} scaffold. Crucially, our subsequent sculpting in Fc_{95} partially mitigated this effect. All scores remain well within the established low-risk threshold (Less than -5), and the implicated hydrophobic patch is known to be effectively shielded by N-glycans in the native state, indicating a minimal practical risk that is overwhelmingly outweighed by the profound gains in affinity.

In summary, the MTIS framework provides a rational *in silico* strategy to balance the inherent trade-offs between affinity, stability, and developability in Fc engineering. By applying this holistic approach, we designed Fc_{95} as a theoretical candidate computationally predicted to achieve significantly enhanced FcγRIIIa binding without compromising structural integrity or immunogenicity. These computational predictions established a strong foundation for Fc_{95}, which we next subjected to rigorous empirical validation.

The Fc_{95} Scaffold is a Versatile and Robust Platform for Engineering Potent Effector Molecules

To determine if Fc_{95} could serve as a versatile engineering platform, we integrated it into five distinct molecular formats alongside fully fucosylated (Fc_{WT}, Fc_{3A}) and afucosylated (Gazyva, MARV Fc_{LZ01}) controls. These included three full-length monoclonal antibodies (anti-Claudin18.2, anti-CD20, anti-MARV GP), a nanobody-Fc fusion (anti-H1N1 HA), and a SIRPα-Fc fusion (anti-CD47) (Fig. 2A). All proteins were successfully expressed in CHO-S systems with therapeutically relevant yields (100–1000 mg/L) and high purity (>90%) (Table S1, Fig. 2B, Fig. S2A), demonstrating the modularity of the Fc_{95} scaffold.

We next assessed the physicochemical stability of the engineered variants. As expected from the rational electrostatic remodeling, Fc_{95} variants exhibited a minor, predictable decrease in

overall isoelectric point (pI) by 0.2–0.3 units (**Fig. 2C**). This was accompanied by a modest reduction in thermal stability (T_m) relative to their WT counterparts, a general trend observed across the aggregated data (**Fig. 2D**) and consistently within each of the five individual target frameworks (**Fig. S2B**). Despite this slight shift, the T_m values of Fc_{95} variants remained well within the acceptable range for therapeutic developability (typically >55°C). Crucially, the aggregation onset temperature (T_{agg})—a primary metric for predicting long-term colloidal stability—was well-maintained. The Fc_{95} variants showed overall T_{agg} profiles comparable to Fc_{WT} and Fc_{3A} (**Fig. 2E**), maintaining this robust colloidal stability across all specific antibody backbones tested (**Fig. S2C**). Together, these data confirm that the Fc_{95} mutations do not compromise fundamental structural integrity, establishing it as a highly stable and broadly compatible platform for therapeutic development.

To further confirm that Fc_{95} maintains robust stability under real-world handling and storage conditions, we subjected three representative backbones (4A7, GAZY, and FD164) to accelerated stress testing, including ten freeze-thaw cycles, prolonged heat (40 ℃ for 14 days), and intense light exposure (4200 lx for 5 or 14 days). As detailed in **Fig. 2G**, across all three antibody backbones, Fc_{95} demonstrated physical stability comparable to, or even exceeding, the wild-type (Fc_{WT}) and Fc_{3A} controls. As anticipated for accelerated antibody stress testing, prolonged thermal stress (40 ℃ for 14 days) exerted the most pronounced impact on physical stability across the tested molecules. While this condition caused a noticeable decrease in main peak purity for GAZY variants (dropping to approximately 80%), the Fc_{95} mutation did not exacerbate degradation relative to Fc_{WT}. Under light stress and freeze-thaw cycles, main peak purity for 4A7 Fc_{95} and GAZY Fc_{95} remained high (>90%), outperforming the clinical benchmark Gazyva, which showed greater sensitivity to thermal and prolonged light conditions. Notably, in the FD164 backbone, Fc_{95} exhibited superior physical stability, maintaining near-baseline main peak purity across all stress conditions, whereas Fc_{WT} showed noticeable degradation under heat and prolonged light exposure.

Chemical stability was similarly preserved, as assessed by the change in acidic charge variants *via* iCIEF (**Fig. 2H**). Consistent with the SEC-HPLC results, exposure to 40 ℃ drove the most significant accumulation of acidic variants across all tested molecules, aligning with typical antibody degradation profiles. For 4A7 and GAZY, the increase in acidic peaks under heat and

light stress for Fc_{95} generally mirrored the trends of the Fc_{WT} controls, indicating no significant new liabilities. In the FD164 backbone, Fc_{95} exhibited a superior baseline chemical profile and maintained lower acidic peak levels than Fc_{WT} across standard, light stress, and freeze-thaw conditions, while showing comparable levels under severe thermal stress. Collectively, these data underscore that the Fc_{95} mutations do not introduce new degradation pathways or exacerbate existing ones, establishing it as a highly robust platform for therapeutic antibody development.

Taken together, these results confirm the holistic integrity of the Fc_{95} scaffold. It not only possesses robust physicochemical properties comparable to its wild-type counterpart, but also demonstrates exquisite biological selectivity. This selectivity profile confirms that MTIS successfully re-sculpted the FcγRIIIa interface without perturbing other critical Fc-mediated biological interactions, achieving a level of precision that is a hallmark of rational design. This dual validation—of both fundamental stability and functional specificity—provides a solid foundation for the subsequent analyses of its enhanced effector activity.

Fc_{95} Platform Selectively Enhances FcγRIIIa Affinity While Preserving Antigen Binding and Broader Fc Receptor Interactions

A prerequisite for any Fc platform is the preservation of antigen-binding activity. We first confirmed that our engineering did not perturb Fab-mediated binding, as all Fc_{95} variants retained binding activities identical to their wild-type counterparts across all five targets (Fig. 3A).

With antigen-binding integrity confirmed, we proceeded to benchmark Fc_{95}'s potency against current state-of-the-art technologies. As detailed in Table S2, the introduction of the Fc_{95} mutations yielded robust increases ranging from ~10- to 100-fold increase in FcγRIIIa binding affinity relative to the wild-type Fc (Fc_{WT}) across all tested antibodies. Furthermore, when compared against the conventional Fc_{3A} engineered mutant, the Fc_{95} scaffold consistently delivered superior affinity enhancement for both the high-affinity (158V) and low-affinity (158F) allotypes of FcγRIIIa. Specifically, across the five constructs (4A7, GAZY, MARV, 13H8, and FD164), Fc_{95} exhibited substantially greater affinity gains, outperforming Fc_{3A} by a range of 4- to 15-fold (Fig. 3B).

Building on this, we positioned Fc_{95} against afucosylation, the current gold standard for ADCC

enhancement. Our anti-CD20 GAZY Fc_{95} surpassed the commercial afucosylated antibody, Gazyva, exhibiting 7.6-fold and 3.7-fold higher affinity for the 158V and 158F allotypes, respectively. This superiority was even more pronounced for our anti-Marburg GP antibody, MARV Fc_{95}. To create a stringent benchmark, we generated an afucosylated control, MARV Fc_{LZ01}, by expressing it in our laboratory's FUT8 knockout CHO-S cell line, which potently enhances ADCC activity by ensuring a fucose content below 10%. Our MARV Fc_{95} variant then outperformed this potent control by a striking 19.5-fold for 158V and 22.4-fold for 158F (Fig. 3C). This analysis provides unambiguous evidence that our structure-guided design achieves an affinity enhancement demonstrably superior to key clinical technologies.

Crucially, this potent enhancement was highly selective. As hypothesized, our engineering strategy skewed the Activating/Inhibitory (A/I) receptor affinity ratio—which balances signaling from FcγRIIIa against the inhibitory FcγRIIb—decisively toward activation. Fc_{95} variants consistently displayed the highest A/I ratios, significantly outperforming both Fc_{3A} and afucosylated formats for both the 158V and 158F allotypes (Fig. 3D). This superior A/I ratio is a direct result of targeted affinity gains, as binding to the inhibitory receptor FcγRIIb and other activating receptors (FcγRI, FcγRIIa) was not significantly altered (ns). This functional profile suggests that Fc_{95}-based therapeutics are poised to elicit a more robust and potent effector cell response.

Finally, we assessed the platform-wide consistency of these effects. An analysis of the mean K_D values across all five constructs confirmed a robust and predictable pattern: the Fc_{95} platform universally and significantly enhanced affinity for both FcγRIIIa allotypes (Fig. 3E, Fig.S3A−F, Table S2). A calculation based on these mean K_D values shows that, on average, Fc_{95} enhanced affinity by approximately 64-fold for FcγRIIIa-158V and 50-fold for FcγRIIIa-158F when compared to Fc_{WT}. Importantly, this enhancement remained highly selective across the platform, as binding to the neonatal Fc receptor (FcRn) also remained unchanged. This consistent and selective profile underscores the robustness of the Fc_{95} modification, confirming it as a true platform technology.

The Fc_{95} Platform Translates Superior Affinity into Potent and Broad *in vitro* Effector Function

To determine if the superior binding affinity of the Fc_{95} platform translates into enhanced

effector function, we conducted a systematic, multi-tiered assessment of its *in vitro* activity. Our strategy involved three key stages: (1) a direct, mechanistic comparison of antibody-dependent cell-mediated cytotoxicity (ADCC) using a Jurkat reporter system expressing either the high-affinity (158V) or low-affinity (158F) allotype of FcγRIIIa, which is critical for evaluating efficacy across the genetically diverse human population; (2) a validation in more physiologically complex co-culture assays using an engineered NK92 cell line overexpressing CD16a (hereinafter referred to as NK92) and peripheral blood mononuclear cells (PBMCs); and (3) a mechanistic investigation into the activation status of primary human NK cells following target engagement.

In the initial Jurkat reporter assays, a clear and consistent functional hierarchy emerged across five distinct therapeutic candidates (Fig. 4A−G and Fig. S4A−B). As expected, the isotype control IgG was inert, while the wild-type (Fc_{WT}) molecules showed minimal activity. The Fc_{95} platform robustly outperformed both the previous-generation Fc_{3A} mutant and the afucosylated clinical benchmarks. For instance, GAZY Fc_{95} demonstrated a 3- to 7-fold greater potency than GAZY Fc_{3A} and was 2- to 8-fold more potent than the commercial afucosylated antibody Gazyva (Fig. 4B-C). Similarly, MARV Fc_{95} was significantly more potent than MARV Fc_{3A} (7- to 78-fold) and achieved both a ~2-fold increase in potency and a markedly higher maximal response compared to its afucosylated counterpart (Fig. 4D−E). This pattern of superiority over Fc_{3A} was consistently observed, with the anti-CD47 fusion protein FD164 Fc_{95} being approximately 11-fold more potent on low-affinity 158F reporter cells (Fig. 4G), and the supplementary candidates, anti-Claudin18.2 (4A7 Fc_{95}) and anti-H1N1 (13H8 Fc_{95}), inducing a higher maximal luminescence or an increase in potency by 2- to 3-fold (Fig. S4A−B). These data establish that the Fc_{95} platform's functional advantage is conserved across multiple targets and is effective against both major FcγRIIIa allotypes.

Crucially, these functional advantages were not only maintained but were substantially amplified in the more stringent primary human effector cell systems (Fig. 4H−M and Fig. S4C−E). In these assays, the superiority of Fc_{95} over both Fc_{3A} and afucosylated comparators was even more pronounced. This was most strikingly demonstrated with the CD20-targeting antibody: the performance gap for GAZY Fc_{95} widened to a ~100-fold (NK92 cells) and ~250-fold (PBMCs) improvement in potency when compared to the afucosylated Gazyva (Fig. 4I−J).

Likewise, for MARV GP, MARV Fc_{95} was approximately 15-fold more potent than the afucosylated MARV Fc_{LZ01} in NK92-mediated lysis assays (Fig. 4K). These results underscore that the benefits of the Fc_{95} platform are most profound in complex, physiologically relevant biological environments.

This amplification effect is further exemplified by challenging molecules like the anti-CD47 fusion protein, FD164, illustrating the substantial improvement potential of the Fc_{95} platform. While the Fc_{95} variant already conferred a potent ~10,000-fold enhancement in the 158V reporter line (Fig. 4F), this effect was non-linearly amplified in the PBMC co-culture system. Here, the Fc_{95} variant catalyzed a dramatic shift leap in potency: the dose-response curve shifted from a nanomolar baseline (EC_{50} > 0.79 ng/mL for Fc_{3A}) to the low attomolar range (EC_{50} ≈ 0.51 fM), corresponding to a staggering >10^9-fold increase in potency (Fig. 4M). This extraordinary gain, attributable solely to the Fc_{95} scaffold, suggests that the ultra-high affinity Fc_{95}-CD16a interaction establishes a highly stable immunological synapse, enabling sustained, serial killing at extremely low concentrations. This mechanism explains how Fc engineering alone can convert a molecule with limited activity into one with profound, attomolar-range therapeutic potential.

To further probe the mechanism underlying this enhanced ADCC, we assessed the activation of primary human NK cells. Upon co-culture with target cells, MARV Fc_{95} significantly outperformed all controls in triggering effector responses. Specifically, MARV Fc_{95} induced the highest level of degranulation, as measured by CD107a-positive NK cells (Fig. 4N, Fig. S4L). More strikingly, it triggered a robust release of Granzyme B (GZMB), with ~77% of NK cells becoming GZMB-positive, compared to ~63% for the afucosylated control and less than 60% for all other variants (***P < 0.001) (Fig. 4O, Fig. S4L). This demonstrates that the Fc_{95} platform directly enhances the activation and armament of primary human NK cells, providing a mechanistic basis for the observed functional superiority.

Finally, to ensure a balanced profile, we assessed the impact of Fc_{95} modifications on other Fc-mediated functions. While Fc_{95} mutants increased ADCP activity relative to Fc_{3A} analogs (Fig. S4F−J), a critical distinction emerged when compared to afucosylation. The commercial afucosylated antibody Gazyva, despite high ADCP potency, showed almost completely abrogated complement-dependent cytotoxicity (CDC) activity. In stark contrast, CDC activity

by GAZY Fc_{95} was fully retained, even showing a modest ~10% increase over the wild-type antibody (Fig. S4K). This suggests the Fc_{95} platform enhances ADCC without the functional trade-offs associated with afucosylation, resulting in a more balanced and potentially safer effector profile.

In summary, these comprehensive in vitro data establish the Fc_{95} platform as a functionally superior technology. It robustly outperforms wild-type, previous-generation engineering (Fc_{3A}), and the clinical gold standard (afucosylation) across multiple therapeutic targets and both major FcγRIIIa allotypes. The amplification of this advantage in primary cell assays, culminating in its ability to unlock exceptional levels of potency for challenging molecules like fusion proteins, provides a solid foundation for its continued development as a next-generation immunotherapy platform.

GAZY Fc_{95} Induces a Multi-layered Transcriptional Reprogramming that Drives NK Cell Effector Differentiation and Function

To elucidate the mechanistic underpinnings of the enhanced cytotoxicity mediated by GAZY Fc_{95}, we performed single-cell RNA sequencing on human NK cells stimulated *in vitro* with GAZY Fc_{95} or an isotype control (a non-targeting, wild-type human IgG1 antibody directed against SEB). Stimulation with GAZY Fc_{95} induced a profound transcriptional reprogramming, with 1,593 genes upregulated and 1,095 genes downregulated compared to the control (Fig. S5A). The most immediate and striking effect was a profound remodeling of the NK cell population structure. Unbiased clustering identified three major NK cell subsets—NK1 (*CX3CR1*$^{+}$*PRF1*$^{+}$), NK2 (*IL7R*$^{+}$*TCF7*$^{+}$), and NK3 (*CCL5*$^{+}$*GZMH*$^{+}$), consistent with established phenotypes (Fig. S5B). While control-stimulated cells maintained a balanced distribution, GAZY Fc_{95} stimulation dramatically reshaped this landscape, driving a significant expansion of the terminally cytotoxic NK1 population at the expense of the NK3 subset (Fig. 5A−B). This result provides the first layer of explanation for the platform's enhanced function: GAZY Fc_{95} actively sculpts the effector population by enriching for its most potent cytotoxic constituents.

Having observed this population shift, we next dissected the molecular machinery driving the heightened cytotoxicity within these cells. A detailed analysis of differentially expressed genes revealed that GAZY Fc_{95} installs a robust, pan-subset activation program (Fig. 5C). Focusing on the dominant NK1 effector subset, we identified a dual-axis remodeling of the cellular state.

Upregulated gene modules were strongly enriched for "offensive" cellular functions, including canonical lymphocyte activation pathways (TCR/BCR signaling), cytoskeletal remodeling for immune synapse formation (focal adhesion), and deep transcriptional rewiring (nuclear speck, histone deacetylase complex) (Fig. 5D−E). This core activation program was headlined by master regulators like *IL21R* and *STAT5B*, immediate-early transcription factors (*JUN*, *NR4A2*), and the activation marker *CD38*. Concurrently, a large module of downregulated genes, primarily ribosomal proteins, pointed to a strategic suppression of "basal homeostasis" functions like cytoplasmic translation (Fig. 5C, E). This deliberate reallocation of cellular resources—boosting immune activation machinery while curtailing non-essential biosynthesis—primes the cell for maximal and sustained effector function. Importantly, these transcriptional signatures were conserved across all NK subsets, indicating a unified activation strategy (Fig. S5C−L).

To connect the macroscopic population shift with the underlying transcriptional program, we performed pseudotime trajectory analysis. This reconstructed a clear, directed differentiation path originating from the NK3 state and progressing toward the terminally differentiated NK1 phenotype (Fig. 5F), providing a direct mechanistic explanation for the observed enrichment of NK1 cells. This developmental trajectory was underpinned by the dynamic regulation of specific gene modules. Notably, the final transition into the highly cytotoxic NK1 state was marked by a significant upregulation of key transcription factors like *FOSB* and a network of heat shock proteins (*HSPA1A*, *HSPA1B*, *HSPH1*) (Fig. S5M). The induction of this chaperone network likely represents a critical quality control mechanism to manage the proteotoxic stress associated with rapid armament, ensuring the fidelity of the effector response.

Finally, we investigated whether this profound cellular reprogramming translated into a more coordinated collective response. Cell-cell interaction analysis revealed that GAZY Fc_{95} stimulation quantitatively amplified the strength of communication networks among all three NK subsets, particularly enhancing signals sent from the dominant NK1 population (Fig. 5G and Fig. S5N). This indicates that beyond enhancing individual cell potency, GAZY Fc_{95} fosters a more integrated and synergistic response across the entire NK cell compartment.

In summary, these single-cell analyses paint a detailed, multi-layered picture of how GAZY Fc_{95} orchestrates a superior NK cell response. The mechanism is four-fold: it (1) reshapes the

effector landscape by driving the differentiation of NK cells toward a terminally cytotoxic phenotype; (2) installs a potent, pan-subset transcriptional program that reallocates cellular resources for maximal activation; (3) guides this maturation along a defined developmental trajectory supported by a robust quality-control network; and (4) enhances intercellular communication to orchestrate a powerful, collective attack. This multi-faceted mechanism, summarized in Fig. 5H, provides a deep mechanistic rationale for the profound cytotoxicity observed.

GAZY Fc_{95} Directs Exogenous NK Cells to Mount an Enhanced Anti-Tumor Response in Immunodeficient Mice

To evaluate our molecular engineering strategy, we tested the hypothesis of whether the enhanced FcγRIIIa engagement engineered into GAZY Fc_{95} translates into a significant therapeutic advantage *in vivo*. To answer this, we first utilized immunodeficient mice reconstituted with human NK92 cells—a controlled system designed to isolate the antibody's intrinsic ability to recruit a defined effector population. The results demonstrate that GAZY Fc_{95} effectively mediates an anti-tumor response that results in durable protection against systemic disease and significant control over established solid tumors.

Our first validation was in a disseminated B-cell lymphoma model, a stringent test of systemic disease control (Fig. 6A). Here, GAZY Fc_{95} demonstrated strong efficacy: a single administration conferred complete and durable protection, with 100% of mice remaining tumor-free for the entire 80-day study (Fig. 6B). This efficacy compared favorably with the clinical benchmark Gazyva (90% survival) and other variants (GAZY Fc_{3A}: 60%; GAZY Fc_{WT}: 80%). This improved survival was underpinned by rapid and comprehensive tumor clearance from both circulation and deep lymphoid tissues, as evidenced in Figure 6C by a significant reduction of $hCD20^+$ cells in peripheral blood to approximately 10% in the GAZY Fc_{95} group—a level1- to 2-fold lower than that observed in all other treatment groups (Fig. S6A). By day 30, GAZY Fc_{95} had reduced the splenic tumor burden to ~2%, a 5-fold greater reduction than Gazyva (~10%) (Fig. 6D). This potent anti-tumor activity was accompanied by a pronounced splenomegaly (Fig. S6B), a hallmark characteristic of the infiltration and proliferation of antibody-directed effector cells, reflecting a robust on-target immune response rather than a pathological event.

Building on this success in a systemic setting, we next investigated whether GAZY Fc_{95} could mediate efficacy against an established solid tumor (Fig. 6E)? The result was a clear success. GAZY Fc_{95} was the only agent capable of imposing dominant control, achieving a remarkable 73.7% tumor growth inhibition (TGI) (Fig. 6F, 6G, S6C). This stood in stark contrast to both the GAZY Fc_{3A} and GAZY Fc_{WT} groups, which exhibited minimal efficacy (TGI $\approx$ 0), underscoring the enhanced activity of the Fc_{95} platform in this challenging context. This was achieved without compromising tolerability, as indicated by stable body weights (Fig. S6D).

This potent efficacy against a solid mass prompted us to dissect the underlying cellular mechanisms within the tumor microenvironment. Immunofluorescence analysis revealed the answer: GAZY Fc_{95} treatment led to a substantial influx of $hCD56^+$ NK cells into the tumor core (Fig. 6I, 6L, S6F). This infiltration correlated with increased tumor cell apoptosis (increased $TUNEL^+$ cells) while simultaneously reducing proliferation (decreased $Ki67^+$ cells) (Fig. 6H, 6J, 6K, S6E).

The observation of this NK cell influx immediately raised a critical question of kinetics and trafficking: how quickly did GAZY Fc_{95} facilitate this infiltration? To visualize this directly, we tracked DIR-labeled NK92 cells in real-time. The result was a stunning confirmation of therapeutic command. Within a mere 3 hours, GAZY Fc_{95} promoted the rapid accumulation of NK cells at the tumor site—a clear kinetic advantage over the slower recruitment by GAZY Fc_{3A} and the background levels of other controls (Fig. 6M, 6N). This was not a transient effect; GAZY Fc_{95} established a sustained localization, with the NK cell signal remaining significantly elevated for at least seven days.

Finally, to compare these findings against a direct, clinically relevant benchmark, we performed a head-to-head therapeutic comparison against Gazyva (Fig. 6O). Using the NK92-only group as a baseline, GAZY Fc_{95} achieved a significantly higher TGI of ~60% compared to ~40% for Gazyva ($P < 0.05$), resulting in substantially smaller final tumor volumes (Fig. 6P, 6Q, S6G). This demonstrates that the Fc_{95} platform provides a statistically significant and therapeutically meaningful improvement over the afucosylated benchmark. And the absence of significant body weight changes in all treatment groups suggests that the administered therapies were well-tolerated by the mice (Fig. S6H).

Similarly, consistent with our previous findings, this head-to-head model comparison

reaffirmed the mechanistic superiority of the Fc_{95} platform. GAZY Fc_{95} again demonstrated a significantly enhanced ability to recruit cytotoxic $hCD56^+$ NK cells into the tumor microenvironment and to induce extensive tumor cell apoptosis ($TUNEL^+$), outperforming Gazyva. Furthermore, both antibody-treated groups (GAZY Fc_{95} and Gazyva) exhibited a pronounced and equivalent suppression of tumor cell proliferation ($Ki67^+$), reducing it by 4- to 5-fold compared to the NK92-only control. This confirms that the enhanced efficacy of GAZY Fc_{95} is driven by its increased NK cell recruitment and potent induction of apoptosis, building upon a shared ability to inhibit tumor proliferation (Fig. S6I).

In conclusion, these studies in a reconstituted immune system unequivocally demonstrate that GAZY Fc_{95} effectively directs NK cell trafficking, facilitates their infiltration into the tumor core, and enhances their cytotoxic activity. Having established this principle, we next investigated whether GAZY Fc_{95} could mobilize the host's own, endogenous NK cell repertoire in a more physiologically relevant system, setting the stage for our investigations in humanized mouse models.

Fc_{95} Enhances the Anti-Tumor Efficacy of a High-Affinity SIRPα Variant by Orchestrating Comprehensive Immunity in hCD16a Transgenic Mice

Having demonstrated the efficacy of the Fc_{95} platform in hematological malignancies (Fig. 6), we next sought to evaluate its performance against solid tumors within a more comprehensive immune context. To achieve this, we utilized hCD16a transgenic mice and targeted the CD47-SIRPα axis using FD164, a fusion protein that binds human CD47 but lacks cross-reactivity with murine CD47[53, 54]. Because optimal anti-CD47 therapy requires both SIRPα blockade and FcγR engagement[11], engrafting human CD47-expressing solid tumors into these mice ensures that FD164 acts exclusively as a tumor-targeting agent without binding to host tissues. This design cleanly isolates the Fc-FcγR interaction as the sole variable, allowing for a controlled *in vivo* assessment of the engineered Fc variants (Fc_{WT}, Fc_{3A}, and Fc_{95}) (Fig. 7A).

The therapeutic impact of the Fc_{95} modification in this stringent model was immediate and profound. Treatment with FD164 Fc_{95} led to near-complete tumor stasis, achieving a remarkable 95.7% tumor growth inhibition (TGI). This efficacy was dramatically superior to the modest control exerted by FD164 Fc_{WT} (54.2% TGI; $P < 0.01$) and the partial response from the clinical-stage mutant FD164 Fc_{3A} (73.3% TGI; $P < 0.05$) (Fig. 7B, 7C). At the study's

endpoint, this translated into near-complete tumor eradication in the Fc_{95} group, leaving only tumors of negligible size and weight. This outcome stood in stark contrast to the substantial tumor burdens in all other groups, underscoring that enhanced FcγR engagement is critical for achieving a complete anti-tumor response (Fig. 7D, 7E). Importantly, all treatments were well-tolerated, with no overt signs of toxicity as indicated by stable body weights throughout the study (Fig. S7A).

To understand the immunological mechanisms driving this superior efficacy, we investigated how Fc_{95} reshapes the entire tumor immune ecosystem. Our data reveal a clear mechanistic blueprint: Fc_{95} first ignites a superior innate immune firestorm, which in turn fuels a qualitatively and quantitatively superior adaptive immune assault, ultimately leading to a complete reversal of the immunosuppressive tumor microenvironment (TME).

This cascade began with the potent mobilization and activation of innate immunity, as revealed by both flow cytometry and spatial immunofluorescence analysis (Fig. 7F−I, Fig. S7B−P). While this analysis revealed no significant inter-group differences in the overall infiltration of total lymphocytes ($CD45^+$), total macrophages, NKT cells, B cells, or $CD4^+$ T cells (Fig. S7B). The detailed flow cytometry gating strategies are shown in Fig. S7C−E. Fc_{95} orchestrated a more robust influx of NK cells into the tumor compared to Fc_{3A} ($P<0.01$ *vs* PBS) and profoundly "supercharged" them, elevating their expression of GZMB and IFN-γ (Fig. 7F−G, S7F). This was complemented by a dramatic reshaping of the myeloid compartment. Both Fc_{3A} and Fc_{95} acted as potent repolarizing agents, driving a massive >10-fold increase in pro-inflammatory M1 macrophages and a concurrent reduction in immunosuppressive M2 cells, shifting the M1/M2 ratio to a pro-inflammatory state (Fig. 7H, S7G−I). However, only Fc_{95} induced a statistically significant influx of neutrophils, highlighting its unique inflammatory signature (Fig. 7F). Crucially, Fc_{95} was also superior in recruiting and maturing dendritic cells ($CD11c^+MHCII^+$), the critical link to the adaptive response (Fig. S7N).

The culmination of this potent innate activation was a decisive and powerful adaptive immune assault, where the superiority of Fc_{95} was most pronounced. It orchestrated a profound re-engineering of the T-cell compartment, inducing a dramatic surge in total T-cell frequency to ~40-45%, an effect far more potent than that observed with Fc_{3A} (Fig. 7F). This T-cell surge was also qualitatively superior, being significantly enriched with cytotoxic $CD8^+$ T cells, which

increased nearly 6-fold over PBS and more than double the effect of Fc_{3A} (Fig. 7I, S7J). Perhaps the most striking mechanistic divergence was Fc_{95}'s unique ability to dismantle the tumor's primary immunosuppressive shield. While other groups maintained high levels of immunosuppressive Tregs, Fc_{95} profoundly depleted this population (Fig. 7F, S7K, 7L). This two-pronged strategy of simultaneously boosting cytotoxic effectors while culling suppressors catapulted the critical $CD8^+$/Treg ratio to a value over 20—more than double that of any other group (Fig. S7M). These findings, consistently observed in both quantitative flow cytometry and spatial immunofluorescence, paint a vivid portrait: Fc_{95}'s superiority stems from its unique ability to translate a broad innate response into a qualitatively superior adaptive assault, defined by overwhelming cytotoxic T-cell dominance and the targeted dismantling of the regulatory T-cell shield.

This profound local remodeling was the epicenter of a systemic immunological shift. Analyses of the spleen and draining lymph nodes (dLNs) revealed a body-wide response orchestrated by FD164 Fc_{95} (Fig. S7O, 7P). In both compartments, Fc_{95} demonstrated superior activation of NK cells and dendritic cells, and a more profound depletion of Tregs compared to Fc_{3A}. This indicates that Fc_{95} establishes a potent baseline of systemic immune activation that is then escalated into an aggressive, polarized anti-tumor phenotype within the TME.

Finally, to unequivocally confirm that superior FcγRIIIa engagement on NK cells is the foundational driver of this entire cascade, we returned to the Raji tumor model in an immunodeficient setting, isolating the therapeutic axis to the FD164 proteins and co-injected human NK92 cells (Fig. 7J). In this stringent test, FD164 Fc_{95} demonstrated profound and sustained tumor control, culminating in complete tumor regression (CR) in 40% of mice (2/5). This result markedly surpassed the single CR (20%) achieved with FD164 Fc_{3A} and the complete lack of regression in the Fc_{WT} group, providing definitive evidence that enhanced affinity for FcγRIIIa is the primary mechanistic trigger for the comprehensive immune response orchestrated by Fc_{95} (Fig. 7K−M). Importantly, this potent anti-tumor effect was achieved without any signs of toxicity, as evidenced by stable body weights across all groups (Fig. S7Q).

In conclusion, we demonstrate that superior FcγRIIIa engagement is the critical design principle for unlocking the full potential of SIRPα-targeted immunotherapy. Our Fc_{95} variant does not simply enhance a single effector function; it acts as a master orchestrator, remodeling

the entire tumor immune ecosystem. By igniting a coordinated, multi-lineage attack that converts a suppressive haven into a hostile landscape, this Fc engineering strategy provides a powerful and translatable blueprint for developing next-generation antibodies capable of achieving deep and durable anti-tumor responses.

Fc_{95} Enhances Therapeutic Efficacy While Ensuring a Favorable Safety Profile

Having established the potent *in vivo* anti-tumor efficacy of the Fc_{95} platform (Figs. 6 and 7), we next sought to address two critical questions for its advancement as a broad therapeutic platform. First, to expand its applicability beyond oncology, we evaluated its function in a stringent *in vivo* Marburg virus pseudovirus infection model. Second, and most crucially, we conducted comprehensive safety and tolerability studies to verify that the platform's elite potency is successfully decoupled from toxicity risks, a common barrier to clinical translation. Here, we demonstrate that Fc_{95} not only extends its therapeutic impact to an infectious disease model but does so while maintaining a favorable safety profile, thereby breaking the classic efficacy-safety trade-off.

Accordingly, we first sought to extend these potent *in vivo* findings to a non-oncology setting, employing a stringent Marburg virus pseudovirus model, which serves as a high bar for demonstrating antibody-mediated effects. The *in vivo* imaging and corresponding quantification revealed a stark divergence in antiviral activity among the variants (Fig. 8A−C). Crucially, treatment with the control antibodies—including wild-type (Fc_{WT}), the clinical-stage mutant (Fc_{3A}), and an afucosylated variant (Fc_{LZ01}) expressed from a fucosyltransferase-knockout cell line—yielded a viral load that was not statistically distinguishable from that of the PBS control group (ns, Fig. 8C). In stark contrast, MARV Fc_{95} was singularly effective, exhibiting a profound and statistically significant reduction in viral load compared to PBS ($P < 0.01$, Fig. 8C) and MARV Fc_{3A} ($P < 0.05$, Fig. 8C) control groups. This result thus provides a powerful *in vivo* validation, demonstrating that the Fc_{95} design confers a level of biological potency unattainable through conventional engineering strategies.

With the platform's potent, cross-indication efficacy established, we then turned to the second, and more critical, question: safety. A crucial test for any highly active immunotherapy is its tolerability. We first assessed this *in vivo* through a high-dose acute toxicity study using a representative CD20 antibody, GAZY Fc_{95}. The platform demonstrated a favorable safety

profile, with no adverse effects on body weight or significant histopathological changes in key organs (Fig. 8D−E, Supplementary Table S3). Notably, its safety profile of hepatic congestion and renal inflammatory cell infiltration were even superior to the alternative engineered variant, GAZY Fc_{3A}, suggesting the Fc_{95} design is inherently better tolerated. To further explore the platform's immunotoxicity profile, we assessed its potential to induce cytokine release syndrome (CRS) using human PBMCs from three individual donors. The assay's sensitivity was first validated by a positive control (Anti-CD3/CD28), which triggered a massive release of key pro-inflammatory cytokines (IFN-γ, TNF-α, IL-6, etc.). In stark contrast, none of the tested antibody variants—GAZY Fc_{95}, Fc_{WT}, or Fc_{3A}—induced any significant cytokine release (Fig. 8F-G). This result is particularly compelling, as it demonstrates that the profound enhancement in effector function conferred by the Fc_{95} design does not come at the cost of increased immunotoxicity.

Taken together, these findings provide a dual validation of the Fc_{95} platform's core principle: demonstrating its broad therapeutic applicability beyond oncology, while simultaneously confirming that this elite potency is achieved without compromising safety. This successful decoupling of efficacy from toxicity solidifies Fc_{95} as a robust and clinically-translatable platform technology.

Fc_{95}'s Superiority is Driven by a Dual Mechanism: Direct Interface Engineering and Concurrently Optimized Glycoform Profile

Through integrated structural and biochemical analyses, we reveal that the superior efficacy of Fc_{95} is driven by a synergistic, dual-action mechanism. Our primary design strategy was validated at the atomic level by the 2.81 Å Cryo-EM structure of the Fc_{95}-CD16a 158F complex. The structure reveals an asymmetric 2:1 (Fc chain: receptor) stoichiometry (Fig. 9A, 9B). The atomic model's accuracy is supported by high-resolution density maps (Fig. 9C) and its strong agreement with AlphaFold3 predictions (0.671 Å RMSD; Fig. 9D). At the binding interface, the structure unequivocally confirms our core engineering hypothesis (Fig. 9E, Fig. S8A). Specifically, it reveals a *de novo* salt bridge between S239D on Fc_{95} and K120 on CD16a, acting as a powerful electrostatic anchor designed *via* our MTIS approach. This anchor works synergistically with the "depolarization and hydrophobic repacking" driven by the Y300L substitution. Furthermore, this stabilized architecture enables a previously unobserved

hydrogen bond between the N297 glycan and CD16a's T122.

To rigorously validate the functional relevance of these structural observations, we introduced disruptive mutations targeting these specific atomic contacts. Size-exclusion chromatography (SEC) confirmed that these mutant proteins exhibited normal profiles, ensuring the mutations did not cause global misfolding. However, BLI analysis demonstrated profound functional losses (Fig. S8B−D). Disrupting the N297-T122 hydrogen bond (T122M on CD16a) reduced affinity by approximately one order of magnitude. More strikingly, breaking the S239D-K120 salt bridge *via* charge reversal (D239K on Fc_{95} or K120D on CD16a) decreased affinity by two orders of magnitude or abolished binding entirely. This progressive loss of affinity confirms that the atomic contacts observed in our Cryo-EM model are the critical determinants of high-affinity engagement. Collectively, these structurally and experimentally verified features constitute the first component of Fc_{95}'s enhanced function: the direct optimization of the binding interface.

Beyond direct structural optimization, Fc_{95} exhibits profound, microenvironment-driven afucosylation. When produced in standard CHO cells, Fc_{95} retains a core fucose content of only 13.8%. This is substantially lower than Fc_{WT} (85.5%), Fc_{3A} (64.5%), and the clinical benchmark Gazyva (41.3%), approaching the levels achieved by specialized FUT8-knockout cell lines (Fig. 9F−G, Fig. S8E−K, Table S4). To deconvolute how a single variant achieves both interface optimization and glycan remodeling, we systematically dissected its constituent mutations (Fig. 9H−J). A clear functional segregation emerged: S239D acts as the primary structural anchor, driving a >10-fold increase in affinity. Conversely, F243L and R292A act synergistically as interior microenvironment-tuning mutations, intrinsically slashing fucose content to 13.8% without independently affecting affinity. Our surface electrostatic potential distribution map reveals that the Fc_{95} scaffold exhibits a distinctly more positive electrostatic microenvironment at the 5 Å heavy-atom radius surrounding N297 compared to the wild-type and Fc_{3A} (Fig. S8L), which may electrostatically repel the fucosyltransferase FUT8 during biosynthesis.

To dissect the specific contribution of glycan remodeling from direct interface binding, we evaluated 4A7 Fc_{95} alongside the highly fucosylated 4A7 $Fc_{3A+S239D}$ variant (77.1% fucose). Strikingly, despite both variants exhibiting nearly identical high affinities for FcγRIIIa (Fig. 9I), their cellular functionalities diverged significantly. Across all cellular assays (Fig. 9K−N), the

low-fucosylated Fc_{95} (13.8% fucose) exhibited vastly superior ADCC performance. Specifically, Fc_{95} not only demonstrated a distinct leftward shift in the dose-response curves (indicating heightened pharmacological potency) but also achieved a several-fold increase in maximal killing efficacy (E_{max}). This functional decoupling demonstrates that high receptor affinity alone is insufficient for optimal cellular activation; rather, the intrinsic afucosylation in Fc_{95} likely alleviates steric hindrance at the receptor interface, thereby translating high-affinity engagement into superior immune synapse formation and maximized ADCC.

Given the elevated high-mannose content in Fc_{95} (Fig. S8J), which typically accelerates in vivo clearance, we rigorously evaluated its pharmacokinetic (PK) profile in Tg-hFcRn mice (Fig. S9). For the GAZY scaffold, GAZY Fc_{95} exhibited a modest 21.6% reduction in circulatory half-life compared to GAZY Fc_{WT} (36.95 h *vs.* 47.13 h). Importantly, its total systemic exposure (AUC) remained statistically comparable to WT (8907.27 *vs.* 10269.06 μg×h/mL) and was significantly higher (1.48-fold) than that of the clinical control Gazyva (6022.15 μg×h/mL, $P < 0.01$). A similar trend was observed in the MARV scaffold: while MARV Fc_{95} showed a 23.4% decrease in half-life (36.53 h *vs.* 47.67 h) relative to MARV Fc_{WT}, it still maintained a robust systemic exposure (AUC = 4511.70 μg×h/mL) that, despite being lower than WT (7189.14 μg×h/mL), outperformed the MARV Fc_{LZ01} control (3856.99 μg×h/mL). Collectively, these data demonstrate that the high-mannose profile of Fc_{95} does not severely impair drug metabolism; the overall pharmacokinetic integrity is well-preserved. This indicates that the slight PK compromise is a highly worthwhile trade-off for the substantial enhancements in ADCC potency and *in vivo* tumor suppression.

In conclusion, Fc_{95} represents a new paradigm in rational antibody engineering. By elegantly integrating direct interface optimization (S239D/Y300L) and localized microenvironment tuning (F243L/R292A) that inherently promotes favorable glycan remodeling, this synergistic design provides a powerful blueprint for creating next-generation immunotherapies with precisely tailored potency.

Discussion

The central finding of this work is the discovery of a powerful synergy between rational protein design and emergent biological function, culminating in an antibody Fc platform, Fc_{95}, that unifies the two most potent strategies for enhancing ADCC. Our project began with the goal of

solving a classic protein engineering problem: achieving hyper-affinity for FcγRIIIa without the typical penalties in stability and manufacturability. We succeeded, but the source of Fc_{95}'s exceptional potency revealed a far more profound principle. We found that computationally designed mutations at the protein interface can act as an intrinsic structural switch, instructing the host cell's machinery to produce a profoundly afucosylated glycoform. It is well established that a low fucose content dramatically amplifies ADCC activity, a mechanism we and others have successfully exploited to combat targets ranging from the Ebola virus to various malignancies[55-58]. To elucidate the biophysical basis of this phenomenon, electrostatic mapping revealed a distinct positive charge enrichment within 5 Å of the Fc_{95} N297 site (Fig. S8L). We propose a "charge-charge repulsion" mechanism: this local positive microenvironment repels both the positively charged FUT8 catalytic pocket and the Ca^{2+} ions essential for mannosidases[59, 60], thereby driving afucosylation and high-mannose accumulation simultaneously. Crucially, this intrinsic glycan remodeling is functionally indispensable. When comparing the low-fucosylated Fc_{95} with a highly fucosylated $Fc_{3A+S239D}$ variant—both sharing identical hyper-affinity for FcγRIIIa (Fig. 9I)—Fc_{95} exhibited vastly superior ADCC potency and maximal efficacy (Emax) (Fig. 9K−N). This functional decoupling confirms that high receptor affinity alone is insufficient; intrinsic afucosylation[61, 62] is essential to alleviate steric hindrance and translate high-affinity engagement into maximized cellular activation.

This dual-action mechanism has profound immunological consequences, recasting our understanding of ADCC enhancement. Conventional ADCC-enhancing antibodies are viewed through the narrow lens of NK cell-mediated lysis. Our deep *in vivo* immune-profiling (Fig. 7) reveals a far more sophisticated reality. The profound efficacy of Fc_{95} is not merely a result of more efficient killing but of a fundamental reprogramming of the tumor immune microenvironment. The most striking feature of this remodeling is the profound and selective depletion of immunosuppressive regulatory T cells (Tregs), an effect not observed with our benchmarks. This capacity to simultaneously boost effector arms (M1 macrophages, $CD8^+$ T cells) while systematically dismantling the primary immunosuppressive barrier represents a highly sought-after goal of immunotherapy. We posit that the hyper-affinity of Fc_{95} for FcγRIIIa, a receptor also expressed on myeloid cells, forges exceptionally stable immunological synapses, which transduce signals of a distinct quality and duration, thereby creating a powerful bridge

between the innate and adaptive immune systems.

Furthermore, although the accumulation of high mannose structures inherently incurs a minor penalty in *in vivo* pharmacokinetics (PK) *via* slightly accelerated systemic clearance, this modest trade-off is vastly outweighed by the profound amplification of therapeutic efficacy, rendering Fc_{95} a highly promising candidate for clinical development. This underscores a powerful paradigm in antibody design, where targeted sequence optimization inadvertently but advantageously influences downstream cellular glycosylation profiles.

Crucially, MTIS should be understood not as a singular computational tool or algorithm, but as a design strategy that embodies a systems-engineering approach to protein interface optimization. This strategy is the crystallization of a design philosophy honed through a decade of research. Our initial efforts in protein engineering, which focused on single-point mutations at key interfacial sites like PD-1 and SIRPα, revealed the limitations of localized optimization and compelled a critical evolution in our thinking. This led to the integration of mammalian cell display and deep mutational scanning, enabling us to comprehensively map and re-sculpt entire energetic landscapes rather than isolated positions. This mastery of 'Interface Sculpting'[53, 54, 63] was further refined when confronting the formidable challenge of rapidly mutating targets like SARS-CoV-2[64]. These foundational studies established the core tenet of MTIS: anchoring designs within structurally conserved, functionally indispensable 'microenvironments', and utilizing first principles to architect novel interfaces with precisely complementary physicochemical properties. MTIS integrates multiple analytical layers—from evolutionary conservation to in silico energetic calculations—to preemptively resolve steric clashes, desolvation penalties, and biophysical liabilities prior to synthesis. The success of Fc_{95} is a direct validation of this philosophy, achieving a >50-fold affinity enhancement for FcγRIIIa while retaining native-like thermal stability (Fig. 2B−H) and eliminating historical biophysical compromises (e.g., F243 steric clashes). Notably, an analysis of human IgG allotypes confirms that these engineered sites do not overlap with natural polymorphisms, highlighting the structural novelty of our design.

Importantly, the versatility of the MTIS platform extends beyond ADCC enhancement. Applying our microenvironment-targeted philosophy, our preliminary studies suggest that MTIS can be adapted to address other major engineering challenges. For instance, we have

utilized this framework to design Fc variants with potentially extended half-lives through optimized FcRn interactions, as well as variants aimed at complete Fc silencing *via* precise structural wedging to abolish residual CD64 binding. These ongoing efforts underscore the potential of MTIS as a universal framework capable of tailoring diverse antibody effector functions.

The defining attributes of Fc_{95}—extreme potency, a superior safety profile, and a clear, synergistic mechanism—position it as a transformative platform for clinical translation. Its modular, "plug-and-play" nature has been validated across multiple molecular formats, including full-length mAbs, Nanobody-Fc fusions, and receptor-Fc traps, demonstrating efficacy in both oncology and infectious disease models (Fig. 6−8). This versatility offers a direct path to highly potent therapeutics, circumventing the complexities and patent barriers associated with bespoke cell-line engineering and establishing a new paradigm for antibody development.

While this work establishes a new benchmark, it also opens up exciting new frontiers of inquiry. The immediate translational path involves validating the safety and efficacy profile of Fc_{95} in non-human primate (NHP) models and initiating IND-enabling studies. Applying the Fc_{95} platform to complex modalities like bispecific antibodies and ADCs could dramatically widen their therapeutic windows. Biologically, our findings underscore a fascinating area for future exploration: deciphering the precise intracellular cascade—such as the potential allosteric modulation of FUT8 expression or localization—that links rationally designed interfacial mutations to host-cell glycan synthesis.

In conclusion, Fc_{95} exemplifies a novel paradigm in antibody engineering, elegantly bridging rational protein design with emergent biological function. By demonstrating that targeted interfacial mutations can organically dictate optimal host-cell glycosylation, this work overcomes the traditional reliance on complex cell-line engineering for afucosylation. The resulting synergistic enhancement of receptor affinity and glycan remodeling unlocks profound immunological control, establishing the MTIS platform as a robust, versatile framework for developing next-generation immunotherapies with maximized efficacy.

Materials and Methods

Computational Modeling and Structure Preparation

Computational modeling was based on high-resolution crystal structures of human IgG1 Fc in complex with various receptors: the Fc-FcγRIIIa (CD16a) complex (PDB ID: 1E4K) for ADCC enhancement. Initial structures were prepared using the Discovery Studio (version 2025, Dassault Systèmes) on a SUN graphic workstation. The structural preparation protocol included the automated addition of missing hydrogen atoms, the assignment of appropriate protonation states for titratable residues at physiological pH (7.4), and the optimization of side-chain orientations. To relieve local steric clashes and relax the 3D coordinates prior to quantitative energy evaluation, a restrained energy minimization was performed using the CVFF (Consistent Valence Force Field) algorithm.

MTIS-Guided Design of Functional Variants and In Silico Analysis

All variants were engineered through the Microenvironment-Tuned Interface Sculpting (MTIS) framework, which utilizes structure-guided, atomic-level analysis to identify and resolve "physicochemical liabilities" at protein-protein interfaces. To execute this structure-guided design, the high-resolution crystal structure of the human IgG1 Fc-FcγRIIIa complex (PDB: 1E4K) was employed as the structural template. Structural visualization, in silico mutagenesis, and precise geometric measurements (e.g., interatomic distances and side-chain extensions) were performed using PyMOL (version 3.0, Schrödinger, LLC). Microenvironment physicochemical properties, including electrostatic potential mapping and Van der Waals (vdW) overlap analysis, were evaluated using Discovery Studio (version 2025, Dassault Systèmes). Furthermore, solvent-accessible surface area (SASA) and desolvation penalties were rigorously quantified utilizing the PDBePISA server and the DSSP algorithm. As an orthogonal validation of the engineering canvas, the evolutionary conservation states of targeted residues were assessed using the ConSurf web server.

Based on the quantitative computational interface diagnosis, in silico mutagenesis was performed to construct the engineered Fc variants. Specific point mutations (including S239D, F243L, R292A, and Y300L) were introduced into the Fc_{3A} scaffold using the mutagenesis tools in PyMOL. Following the insertion of mutations, local structural refinement and energy minimization of the mutated interfaces were conducted using Discovery Studio to resolve potential steric clashes and optimize side-chain conformations. The finalized in silico designs,

which aimed to maximize receptor recruitment through optimized hydrophobic packing and electrostatic interactions, were subsequently synthesized and advanced to empirical testing (detailed in the following *in vitro* expression and functional validation sections).

Evolutionary Conservation Analysis

The evolutionary plasticity of mutation sites was assessed using the ConSurf Web Server. The human IgG1 Fc sequence (PDB: 1E4K, chain A) was used as a query against the UniRef90 database with HMMER (E-value < 0.0001) to collect homologous sequences. Conservation scores, on a scale of 1 (variable) to 9 (highly conserved), were calculated from a multiple sequence alignment generated by MAFFT, using the empirical Bayesian method implemented in Rate4Site.

Molecular Dynamics Simulations and Free Energy Calculations

All-atom MD simulations (100 ns) were performed on Fc/CD16a complexes using GROMACS 2021.5 with the CHARMM36m force field. Each complex was solvated in a TIP3P water box with 0.15 M NaCl. The protocol included energy minimization, followed by NVT (1 ns) and NPT (5 ns) equilibration prior to the production run. Binding free energies (ΔG_MMPBSA) were calculated from 20 snapshots extracted from the final 20 ns of each trajectory using the gmx MMPBSA toolkit.

Surface Electrostatic Potential Distribution Calculation

Based on 3-D spatial protein structures， setting protein boundary as full colombic energy, the protein charges as Delphi program charge, the radius as Van der Waal Radii, the solvent dielectric as 80, ionic strength as 0.145, ionic radius as 2.0, and then all calculations was carried out using DELPHI program.

Developability and Stability Predictions

The impact of mutations on monomer stability (ΔΔG folding) was predicted using Wemol software. To assess potential immunogenicity, linear B-cell epitopes were predicted with BepiPred-2.0, conformational B-cell epitopes with DiscoTope 2.0, and T-cell epitope binding to representative MHC-I and MHC-II alleles with NetMHCpan-4.1. The intrinsic aggregation propensity was evaluated by calculating the global solubility score (Na4vSS) using the CamSol server.

Structural Modeling and Visualization

Three-dimensional models of the Fc_{3A}-CD16a 158F and Fc_{95}-CD16a 158F complexes were generated using AlphaFold3 and energy-minimized with Wemol (AMBER14SB force field). All structural figures were rendered using the PyMOL Molecular Graphics System, Version 3.0.

Cell Lines and Reagents

The following human cancer cell lines were used: NUGC4, Raji, A549, MC38(hCD47), MC38(PD-L1), and 293T cells, along with engineered 293T (MARV GP) and NK92 ($CD16a^+$) cells. Cells were maintained in their respective recommended media (RPMI 1640, DMEM, or MEMα), supplemented with 10% FBS and antibiotics. ADCC Jurkat reporter cell lines (158V and 158F) were from Genomeditech (Shanghai, China). Human PBMCs were isolated from healthy donors following institutional guidelines.

Antibody and Fusion Protein Production and Purification

Construction and Expression of Antibody and Fusion Protein Variants

Antibody and fusion protein variants were constructed using various targeting moieties, including anti-Claudin 18.2 (4A7), anti-CD20 (GAZY), anti-MARV GP (MARV), anti-H1N1 (13H8), and anti-CD47 (FD164). GAZY denotes constructs utilizing the variable domain sequences of the Type II anti-CD20 antibody obinutuzumab (Gazyva®).

To systematically evaluate effector functions and address the impact of glycosylation, the engineered Fc scaffolds were strictly categorized as follows:

- **Fucosylated Baseline and Controls:** Fc_{WT} serves as the baseline, fully fucosylated parental IgG1. Fc_{3A} is a conventional, fully fucosylated Fc-engineered control containing three specific amino acid mutations without any glyco-engineering.
- **Afucosylated Benchmark Controls:** We utilized two afucosylated wild-type (WT) benchmark controls with distinct afucosylation profiles: Gazyva (anti-CD20), a widely used clinical antibody with a typical afucosylation rate of 50%–60%, and MARV Fc_{LZ01} (anti-MARV), an in-house preclinical candidate. To achieve a more thorough afucosylation, MARV Fc_{LZ01} was expressed in a proprietary *FUT8*-knockout cell line, yielding an afucosylation efficiency of >95%.
- **Novel ADCC-Enhanced Series:** Fc_{95} is our novel engineered variant designed to intrinsically reduce core fucose through amino acid mutations alone. Intermediate mutants ($Fc_{3A+S239D}$, $Fc_{3A+F243L}$, $Fc_{3A+R292A}$, $Fc_{3A+Y300L}$) were also generated to dissect synergistic effects.

- **Structural Validation Mutants:** Targeted interface disruptions, including Fc_{95} (D239K), CD16a (K120D), and CD16a (T122M), were generated to verify the Cryo-EM structural findings.
- **Isotype IgG Control:** A recombinant human IgG1 antibody targeting Staphylococcal enterotoxin B (anti-SEB isotype control), which lacks cognate antigens in all tested systems, was utilized as the universal non-targeting isotype control for all *in vitro* experiments.

Genes encoding the heavy chains, light chains, and antigen constructs were synthesized and cloned into pcDNA3.4 expression vectors. To achieve the distinct glycosylation profiles required for our comparative analysis, two different expression systems were employed. The afucosylated benchmark Gazyva was purchased from *Roche* and MARV $Fc_{LZ01}$was specifically produced using a FUT8-knockout CHO cell line to ensure a minimal fucose background. In contrast, all other constructs—including the fully fucosylated Fc_{WT} and Fc_{3A}, as well as the intrinsically afucosylated novel Fc_{95} variant—were transiently expressed in standard wild-type CHO-S cells (Gibco).

Protein Purification and Quality Control

Fc-containing antibodies and fusion proteins were purified *via* Protein A affinity chromatography (MabSelect PrismA, Cytiva). His-tagged antigens and CD16a variants were purified using immobilized metal affinity chromatography (IMAC) *via* Ni-NTA agarose (Cytiva). Purity and assembly integrity were confirmed using HPLC-SEC and SDS-PAGE to ensure >95% purity for all utilized proteins.

N-Glycan Analysis by HILIC-UPLC

N-linked glycans were enzymatically released from purified antibodies (100 µg) using PNGase F (New England Biolabs) according to the manufacturer's instructions. The released glycans were fluorescently labeled with 2-aminobenzamide (2-AB) via reductive amination. The 2-AB labeled glycan library was then analyzed using a Waters ACQUITY UPLC system equipped with a Glycan BEH Amide Column (1.7 µm, 2.1 × 150 mm). Separation was performed using a linear gradient of [50 mM ammonium formate, pH 4.4] and [100% acetonitrile] at a flow rate of [0.4 mL/min] at [60°C]. Fluorescence was detected at an excitation wavelength of 330 nm and an emission wavelength of 420 nm. Glycan species were identified by matching glucose unit (GU) values to the GlycoStore database and

quantified by integrating relative peak areas using Empower 3 software.

Biophysical Characterization

Thermal stability (Tm, Tagg) was determined by monitoring intrinsic fluorescence during a thermal ramp (25-95°C) on an UNCLE instrument (Unchained Labs). Isoelectric points (pI) were measured by imaged capillary isoelectric focusing (iCIEF) on an iCE3 instrument (ProteinSimple).

Cryo-EM Structure Determination

The Fc_{95}-CD16a complex was purified by size-exclusion chromatography and vitrified on Quantifoil R1.2/1.3 gold grids using a Vitrobot Mark IV (Thermo Fisher Scientific). Cryo-EM data were collected on a 300 kV Titan Krios G4 microscope with a Falcon 4 detector. Data processing, including motion correction (MotionCor2), CTF estimation (SMART), particle picking (Topaz), and multiple rounds of refinement in cryoSPARC, yielded a final map at 2.81 Å resolution. The model was built by docking AlphaFold3 predictions into the density, followed by manual rebuilding in Coot and real-space refinement in PHENIX. The final map and coordinates are deposited under accession codes EMD-66494 and PDB-9X35.

Target Recognition and Fc Receptor Affinity Analysis

To evaluate target recognition, cell-based binding of the engineered variants to target-positive cells (NUGC4, Raji, and MC38(CD47)) was quantified by flow cytometry (BD FACSCalibur™) using fluorophore-conjugated secondary antibodies. Antigen-binding ELISA was performed by coating plates with recombinant antigens (MARV GP, H1N1 HA) and detecting bound Fc variants with an HRP-conjugated anti-human IgG secondary antibody. To further characterize Fc-mediated interactions, kinetic and steady-state affinity analyses for various Fc receptors were performed using biolayer interferometry (BLI) on an Octet RED96e system (Sartorius). Sensorgrams were evaluated using a 1:1 Langmuir binding model where appropriate to determine the association rate (k_a), dissociation rate (k_d), and equilibrium dissociation constants K_D.

***In Vitro* Functional Assays**

ADCC and ADCP activities were measured using engineered Jurkat reporter cells expressing FcγRIIIa or FcγRIIa, respectively, which report activation *via* luciferase expression. Primary

cell cytotoxicity was assessed by co-culturing target cells with human PBMCs or NK92 cells and quantifying LDH release. CDC was measured by LDH release from Raji cells incubated with antibodies and human serum complement. Primary NK cell activation was determined by flow cytometric analysis of CD107a and intracellular Granzyme B expression after co-culture with antibody-opsonized target antigen.

Human Cytokine Release Assay

Human PBMCs were incubated with test molecules for 72 h. Supernatants were analyzed for a panel of 10 proinflammatory cytokines (IFN-γ, IL-6, TNF-α, etc.) using a V-PLEX kit on a MESO QuickPlex SQ 120 instrument.

Single-cell RNA sequencing

Single-cell suspensions from NK cells in a mixed *in vitro* culture system, stimulated with either GAZY Fc_{95} or an isotype control (a non-targeting, wild-type human IgG1 anti-Staphylococcal enterotoxin B (SEB) antibody, anti-SEB isotype control), were processed using the 10x Genomics Chromium platform. Libraries were sequenced on an Illumina NextSeq 500. Data were processed with Cell Ranger, and downstream analysis (filtering, integration, clustering, and visualization) was performed using Seurat and other R packages.

Animal Studies

All experiments were approved by the Institutional Animal Care and Use Committee (IACUC) of the Beijing Institute of Pharmacology and Toxicology (IACUC-DWZX-2025-625). Six- to 8-week-old female NOD-SCID, BALB/c, Nude, hCD16a transgenic, and hFcRn transgenic mice were used. Tumor models included a Raji disseminated lymphoma model, Raji and MC38(hCD47) subcutaneous xenograft models. Treatments involved intravenous (i.v.) or intraperitoneal (i.p.) administration of antibodies, effector cells, or pseudovirus. Tumor growth, survival, and *in vivo* fluorescence (IVIS Spectrum) were monitored. Pharmacokinetics were studied in hFcRn transgenic mice, and acute toxicity was evaluated in BALB/c mice.

Histological and Immunofluorescence Analysis

Drainage of lymph nodes and spleen tissues were fixed, sectioned, and analyzed by immunohistochemistry (IHC) for CD20. Tumor tissues were fixed, sectioned, and analyzed by immunofluorescence (IF) for a panel of markers including Ki67, TUNEL, and various immune cell markers (CD56, CD49b, CD11b, F4/80, etc.). Images were acquired on a confocal

microscope and quantified using ImageJ.

Pharmacokinetic (PK) Analysis in Humanized FcRn Transgenic Mice

Six to 8-week-old hFcRn female transgenic (C57BL/6Smoc-Fcgrt$^{em2(hFCGRT)Smoc}$) mice were randomly assigned to experimental groups (n = 3–4 per group) and administered a single intravenous (i.v.) dose of 10 mg/kg antibody (e.g., GAZY-Fc, MARV-Fc). Following administration, blood samples were collected into heparinized microcentrifuge tubes at 0.083 (5 min), 2, 6, 12, 24, 48, 72, 96, 120, 144, 168, 192, and 216 hours post-injection. Plasma was immediately separated by centrifugation at 4,000 rpm for 10 min at 4°C. For quantification, plasma antibody concentrations were determined using a standard colorimetric sandwich ELISA. Briefly, microtiter plates were coated with a Goat anti-Human IgG (H+L) capture antibody (SeraCare, Cat# 5210-0159), followed by the addition of diluted plasma samples. Bound antibodies were subsequently detected using an HRP-conjugated Goat anti-Human IgG (H+L) secondary antibody (Thermo Fisher-Novex, Cat# A18805). Antibody concentrations at each time point were calculated based on a standard calibration curve and the respective dilution factors. Finally, pharmacokinetic parameters were derived from the concentration-time data using Phoenix WinNonlin software, with results presented as mean ± standard deviation (SD).

Flow Cytometry Analysis of Tissues

Tissue Processing

Spleens and lymph nodes were mechanically dissociated through 70-μm cell strainers. Splenocytes were additionally treated with ACK lysis buffer (Solarbio) to remove red blood cells. Tumors were excised, minced, and digested in DMEM containing 2% fetal bovine serum (FBS) and 1 mg/mL collagenase IV (Sigma) for 1 h at 37°C with agitation, followed by filtration through a 70-μm cell strainer.

Cell Staining and Data Acquisition

(Note: All fluorophore-conjugated antibodies targeted mouse antigens and were purchased from BioLegend unless otherwise specified).

Single-cell suspensions were washed and resuspended in FACS buffer (PBS supplemented with 2% BSA). To exclude dead cells, samples were first stained with the Zombie Aqua™ Fixable Viability Kit (Cat# 423102). To block non-specific Fc receptor binding, cells were incubated with anti-CD16/CD32 (BD Pharmingen, clone 2.4G2, 1:100) in 25 μL FACS buffer for 15 min

at room temperature.

For surface staining, cells were incubated for 30 min on ice with a cocktail of antibodies targeting surface markers: Alexa Fluor® 700 anti-CD45 (Cat# 157210), PerCP/Cy5.5 anti-CD3 (Cat# 100218), FITC anti-CD4 (Cat# 100406), PE anti-CD25 (Cat# 102008), PE/Cy7 anti-CD8a (Cat# 100702), APC/Cy7 anti-CD19 (152412), PE anti-CD49b (Cat# 103506), APC anti-CD11b (Cat# 101212), Brilliant Violet 711™ (Cat# BV711) anti-CD11c (Cat# 117349), BV421 anti-MHC-II (I-A/I-E, Cat# 107632), PE/Dazzle™ 594 anti-F4/80 (Cat# 123146), BV605 anti-CD86 (Cat# 105037), BV711 anti-CD206 (Cat# 141727), and BV570 anti-Ly-6G (Cat# 127629).

For intracellular staining, following surface staining and two washes, cells were fixed and permeabilized according to the manufacturer's instructions. The Cyto-Fast™ Fix/Perm Solution (Cat# 426803) was used for cytokines, followed by staining with PerCP/Cy5.5 anti-Granzyme B (Cat# 372212) and BV421 anti-IFN-γ (Cat# 505830). The True-Nuclear™ Transcription Factor Buffer Set (Cat# 424401) was utilized for nuclear targets, followed by staining with Alexa Fluor® 647 anti-Foxp3 (Cat# 126408).

Finally, cells were washed twice, resuspended in 150 μL FACS buffer, and acquired on a BD FACSCalibur flow cytometer (BD Biosciences). Data were analyzed using FlowJo software.

Statistical Analysis

Data are presented as mean ± SEM. Statistical analyses were performed using GraphPad Prism (v8.0). Survival curves were compared using the log-rank (Mantel-Cox) test. Comparisons between groups were made using one-way or two-way ANOVA with appropriate post-hoc tests. Significance was denoted as $*P < 0.05$, $**P < 0.01$, $***P < 0.001$, and $****P < 0.0001$.

Statement on AI-generated content: The authors confirm that no artificial intelligence generated content (AIGC) tools, such as ChatGPT or other large language model (LLM) based tools, were used in the preparation of any part of this manuscript.

References

1. Paul S, Konig MF, Pardoll DM, Bettegowda C, Papadopoulos N, Wright KM*, et al.* Cancer therapy with antibodies. **Nat Rev Cancer 2024**, 24(6)**:** 399-426.
2. Corti D, Purcell LA, Snell G, Veesler D. Tackling COVID-19 with neutralizing monoclonal antibodies. **Cell 2021**, 184(12)**:** 3086-3108.
3. van Lengerich B, Zhan L, Xia D, Chan D, Joy D, Park JI*, et al.* A TREM2-activating antibody with a blood-brain barrier transport vehicle enhances microglial metabolism in Alzheimer's

disease models. **Nat Neurosci 2023**, 26(3)**:** 416-429.
4. Carter PJ, Rajpal A. Designing antibodies as therapeutics. **Cell 2022**, 185(15)**:** 2789-2805.
5. Strohl WR. Current progress in innovative engineered antibodies. **Protein Cell 2018**, 9(1)**:** 86-120.
6. Sneed SL, Reese BB, Laureano AF, Ratnapriya S, Fraschilla I, Jeffrey KL*, et al.* An engineered immunomodulatory IgG1 Fc suppresses autoimmune inflammation through pathways shared with i.v. immunoglobulin. **J Clin Invest 2024**, 134(4).
7. Bournazos S, Wang TT, Dahan R, Maamary J, Ravetch JV. Signaling by Antibodies: Recent Progress. **Annu Rev Immunol 2017**, 35**:** 285-311.
8. Gunn BM, Lu R, Slein MD, Ilinykh PA, Huang K, Atyeo C*, et al.* A Fc engineering approach to define functional humoral correlates of immunity against Ebola virus. **Immunity 2021**, 54(4)**:** 815-828.e815.
9. Zhang A, Stacey HD, D'Agostino MR, Tugg Y, Marzok A, Miller MS. Beyond neutralization: Fc-dependent antibody effector functions in SARS-CoV-2 infection. **Nat Rev Immunol 2023**, 23(6)**:** 381-396.
10. Grace PS, Peters JM, Sixsmith J, Lu R, Irvine EB, Luedeman C*, et al.* Antibody-Fab and -Fc features promote Mycobacterium tuberculosis restriction. **Immunity 2025**, 58(6)**:** 1586-1597.e1585.
11. Osorio JC, Smith P, Knorr DA, Ravetch JV. The antitumor activities of anti-CD47 antibodies require Fc-FcγR interactions. **Cancer Cell 2023**, 41(12)**:** 2051-2065.e2056.
12. Yamin R, Jones AT, Hoffmann HH, Schäfer A, Kao KS, Francis RL*, et al.* Fc-engineered antibody therapeutics with improved anti-SARS-CoV-2 efficacy. **Nature 2021**, 599(7885)**:** 465-470.
13. Kang TH, Jung ST. Boosting therapeutic potency of antibodies by taming Fc domain functions. **Exp Mol Med 2019**, 51(11)**:** 1-9.
14. Pyzik M, Kozicky LK, Gandhi AK, Blumberg RS. The therapeutic age of the neonatal Fc receptor. **Nat Rev Immunol 2023**, 23(7)**:** 415-432.
15. Pinto S, Pahl J, Schottelius A, Carter PJ, Koch J. Reimagining antibody-dependent cellular cytotoxicity in cancer: the potential of natural killer cell engagers. **Trends Immunol 2022**, 43(11)**:** 932-946.
16. Yu Y, Wang M, Zhang X, Li S, Lu Q, Zeng H*, et al.* Antibody-dependent cellular cytotoxicity response to SARS-CoV-2 in COVID-19 patients. **Signal Transduct Target Ther 2021**, 6(1)**:** 346.
17. Von Holle TA, Moody MA. Influenza and Antibody-Dependent Cellular Cytotoxicity. **Front Immunol 2019**, 10**:** 1457.
18. Nimmerjahn F, Ravetch JV. Divergent immunoglobulin g subclass activity through selective Fc receptor binding. **Science 2005**, 310(5753)**:** 1510-1512.
19. Bulliard Y, Jolicoeur R, Windman M, Rue SM, Ettenberg S, Knee DA*, et al.* Activating Fc γ receptors contribute to the antitumor activities of immunoregulatory receptor-targeting antibodies. **J Exp Med 2013**, 210(9)**:** 1685-1693.
20. Edgar JE, Bournazos S. Fc-FcγR interactions during infections: From neutralizing antibodies to antibody-dependent enhancement. **Immunol Rev 2024**, 328(1)**:** 221-242.
21. Golay J, Andrea AE, Cattaneo I. Role of Fc Core Fucosylation in the Effector Function of IgG1 Antibodies. **Front Immunol 2022**, 13**:** 929895.

22. Oosterhoff JJ, Larsen MD, van der Schoot CE, Vidarsson G. Afucosylated IgG responses in humans - structural clues to the regulation of humoral immunity. **Trends Immunol 2022**, 43(10)**:** 800-814.
23. Park JE, Kim SE, Keam B, Park HR, Kim S, Kim M*, et al.* Anti-tumor effects of NK cells and anti-PD-L1 antibody with antibody-dependent cellular cytotoxicity in PD-L1-positive cancer cell lines. **J Immunother Cancer 2020**, 8(2).
24. Stefańczyk SA, Hagelstein I, Lutz MS, Müller S, Holzmayer SJ, Jarjour G*, et al.* Induction of NK cell reactivity against acute myeloid leukemia by Fc-optimized CD276 (B7-H3) antibody. **Blood Cancer J 2024**, 14(1)**:** 67.
25. Mössner E, Brünker P, Moser S, Püntener U, Schmidt C, Herter S*, et al.* Increasing the efficacy of CD20 antibody therapy through the engineering of a new type II anti-CD20 antibody with enhanced direct and immune effector cell-mediated B-cell cytotoxicity. **Blood 2010**, 115(22)**:** 4393-4402.
26. Musolino A, Gradishar WJ, Rugo HS, Nordstrom JL, Rock EP, Arnaldez F*, et al.* Role of Fcγ receptors in HER2-targeted breast cancer therapy. **J Immunother Cancer 2022**, 10(1).
27. Gerdes CA, Nicolini VG, Herter S, van Puijenbroek E, Lang S, Roemmele M*, et al.* GA201 (RG7160): a novel, humanized, glycoengineered anti-EGFR antibody with enhanced ADCC and superior in vivo efficacy compared with cetuximab. **Clin Cancer Res 2013**, 19(5)**:** 1126-1138.
28. García-Alija M, van Moer B, Sastre DE, Azzam T, Du JJ, Trastoy B*, et al.* Modulating antibody effector functions by Fc glycoengineering. **Biotechnol Adv 2023**, 67**:** 108201.
29. Burton DR, Dwek RA. Immunology. Sugar determines antibody activity. **Science 2006**, 313(5787)**:** 627-628.
30. Stelter S, Paul MJ, Teh AY, Grandits M, Altmann F, Vanier J*, et al.* Engineering the interactions between a plant-produced HIV antibody and human Fc receptors. **Plant Biotechnol J 2020**, 18(2)**:** 402-414.
31. Bowden TA, Baruah K, Coles CH, Harvey DJ, Yu X, Song BD*, et al.* Chemical and structural analysis of an antibody folding intermediate trapped during glycan biosynthesis. **J Am Chem Soc 2012**, 134(42)**:** 17554-17563.
32. Li T, DiLillo DJ, Bournazos S, Giddens JP, Ravetch JV, Wang LX. Modulating IgG effector function by Fc glycan engineering. **Proc Natl Acad Sci U S A 2017**, 114(13)**:** 3485-3490.
33. Pereira NA, Chan KF, Lin PC, Song Z. The "less-is-more" in therapeutic antibodies: Afucosylated anti-cancer antibodies with enhanced antibody-dependent cellular cytotoxicity. **MAbs 2018**, 10(5)**:** 693-711.
34. Rogers KA, Huang Y, Ruppert AS, Awan FT, Heerema NA, Hoffman C*, et al.* Phase 1b study of obinutuzumab, ibrutinib, and venetoclax in relapsed and refractory chronic lymphocytic leukemia. **Blood 2018**, 132(15)**:** 1568-1572.
35. Sehn LH, Martelli M, Trněný M, Liu W, Bolen CR, Knapp A*, et al.* A randomized, open-label, Phase III study of obinutuzumab or rituximab plus CHOP in patients with previously untreated diffuse large B-Cell lymphoma: final analysis of GOYA. **J Hematol Oncol 2020**, 13(1)**:** 71.
36. Dammen-Brower K, Epler P, Zhu S, Bernstein ZJ, Stabach PR, Braddock DT*, et al.* Strategies for Glycoengineering Therapeutic Proteins. **Front Chem 2022**, 10**:** 863118.
37. Yoshimitsu M, Choi I, Kusumoto S, Shimokawa M, Utsunomiya A, Suehiro YD*, et al.* A phase 2 Trial of CHOP with Anti-CCR4 Antibody Mogamulizumab for older Patients with Adult T-

Cell Leukemia/Lymphoma. **Blood 2025**.

38. Shields RL, Namenuk AK, Hong K, Meng YG, Rae J, Briggs J*, et al.* High resolution mapping of the binding site on human IgG1 for Fc gamma RI, Fc gamma RII, Fc gamma RIII, and FcRn and design of IgG1 variants with improved binding to the Fc gamma R. **J Biol Chem 2001**, 276(9)**:** 6591-6604.
39. Schewe DM, Alsadeq A, Sattler C, Lenk L, Vogiatzi F, Cario G*, et al.* An Fc-engineered CD19 antibody eradicates MRD in patient-derived MLL-rearranged acute lymphoblastic leukemia xenografts. **Blood 2017**, 130(13)**:** 1543-1552.
40. Koerner SP, André MC, Leibold JS, Kousis PC, Kübler A, Pal M*, et al.* An Fc-optimized CD133 antibody for induction of NK cell reactivity against myeloid leukemia. **Leukemia 2017**, 31(2)**:** 459-469.
41. Lazar GA, Dang W, Karki S, Vafa O, Peng JS, Hyun L*, et al.* Engineered antibody Fc variants with enhanced effector function. **Proc Natl Acad Sci U S A 2006**, 103(11)**:** 4005-4010.
42. Markham A. Margetuximab: First Approval. **Drugs 2021**, 81(5)**:** 599-604.
43. Rugo HS, Im SA, Cardoso F, Cortes J, Curigliano G, Musolino A*, et al.* Margetuximab Versus Trastuzumab in Patients With Previously Treated HER2-Positive Advanced Breast Cancer (SOPHIA): Final Overall Survival Results From a Randomized Phase 3 Trial. **J Clin Oncol 2023**, 41(2)**:** 198-205.
44. Park HI, Yoon HW, Jung ST. The Highly Evolvable Antibody Fc Domain. **Trends Biotechnol 2016**, 34(11)**:** 895-908.
45. Levin D, Golding B, Strome SE, Sauna ZE. Fc fusion as a platform technology: potential for modulating immunogenicity. **Trends Biotechnol 2015**, 33(1)**:** 27-34.
46. Sondermann P, Huber R, Oosthuizen V, Jacob U. The 3.2-A crystal structure of the human IgG1 Fc fragment-Fc gammaRIII complex. **Nature 2000**, 406(6793)**:** 267-273.
47. Nimmerjahn F, Ravetch JV. Fcgamma receptors as regulators of immune responses. **Nat Rev Immunol 2008**, 8(1)**:** 34-47.
48. Younes A, Yasothan U, Kirkpatrick P. Brentuximab vedotin. **Nat Rev Drug Discov 2012**, 11(1)**:** 19-20.
49. Weiner GJ. Building better monoclonal antibody-based therapeutics. **Nat Rev Cancer 2015**, 15(6)**:** 361-370.
50. Stone CA, Jr., Spiller BW, Smith SA. Engineering therapeutic monoclonal antibodies. **J Allergy Clin Immunol 2024**, 153(3)**:** 539-548.
51. Yu X, Baruah K, Harvey DJ, Vasiljevic S, Alonzi DS, Song BD*, et al.* Engineering hydrophobic protein-carbohydrate interactions to fine-tune monoclonal antibodies. **J Am Chem Soc 2013**, 135(26)**:** 9723-9732.
52. Duncan AR, Woof JM, Partridge LJ, Burton DR, Winter G. Localization of the binding site for the human high-affinity Fc receptor on IgG. **Nature 1988**, 332(6164)**:** 563-564.
53. Wang Z, Hu N, Li X, Wang H, Ren C, Qiao C*, et al.* Selection and Characterization of FD164, a High-Affinity Signal Regulatory Protein α Variant with Balanced Safety and Effectiveness, from a Targeted Epitope Mammalian Cell-Displayed Antibody Library. **Mol Pharmacol 2021**, 100(3)**:** 193-202.
54. Wang Z, Hu N, Wang H, Wu Y, Quan G, Wu Y*, et al.* High-affinity decoy protein, nFD164, with an inactive Fc region as a potential therapeutic drug targeting CD47. **Biomed Pharmacother 2023**, 162**:** 114618.

55. Shields RL, Lai J, Keck R, O'Connell LY, Hong K, Meng YG*, et al.* Lack of fucose on human IgG1 N-linked oligosaccharide improves binding to human Fcgamma RIII and antibody-dependent cellular toxicity. **J Biol Chem 2002**, 277(30)**:** 26733-26740.
56. Olinger GG, Jr., Pettitt J, Kim D, Working C, Bohorov O, Bratcher B*, et al.* Delayed treatment of Ebola virus infection with plant-derived monoclonal antibodies provides protection in rhesus macaques. **Proc Natl Acad Sci U S A 2012**, 109(44)**:** 18030-18035.
57. Goede V, Fischer K, Busch R, Engelke A, Eichhorst B, Wendtner CM*, et al.* Obinutuzumab plus chlorambucil in patients with CLL and coexisting conditions. **N Engl J Med 2014**, 370(12)**:** 1101-1110.
58. Qiu X, Audet J, Lv M, He S, Wong G, Wei H*, et al.* Two-mAb cocktail protects macaques against the Makona variant of Ebola virus. **Sci Transl Med 2016**, 8(329)**:** 329ra333.
59. Tempel W, Karaveg K, Liu ZJ, Rose J, Wang BC, Moremen KW. Structure of mouse Golgi alpha-mannosidase IA reveals the molecular basis for substrate specificity among class 1 (family 47 glycosylhydrolase) alpha1,2-mannosidases. **J Biol Chem 2004**, 279(28)**:** 29774-29786.
60. Vallée F, Lipari F, Yip P, Sleno B, Herscovics A, Howell PL. Crystal structure of a class I alpha1,2-mannosidase involved in N-glycan processing and endoplasmic reticulum quality control. **Embo j 2000**, 19(4)**:** 581-588.
61. Ihara H, Ikeda Y, Toma S, Wang X, Suzuki T, Gu J*, et al.* Crystal structure of mammalian alpha1,6-fucosyltransferase, FUT8. **Glycobiology 2007**, 17(5)**:** 455-466.
62. García-García A, Ceballos-Laita L, Serna S, Artschwager R, Reichardt NC, Corzana F*, et al.* Structural basis for substrate specificity and catalysis of α1,6-fucosyltransferase. **Nat Commun 2020**, 11(1)**:** 973.
63. Liu H, Qiao C, Hu N, Wang Z, Wang J, Feng J*, et al.* High-Affinity Decoy PD-1 Mutant Screened from an Epitope-Specific Cell Library. **Engineering 2021**, 7(11)**:** 1557-1565.
64. Wang Z, Shi Z, Liao X, Quan G, Dong H, Zhao P*, et al.* Broad-Spectrum Engineered Multivalent Nanobodies Against SARS-CoV-1/2. **Adv Sci (Weinh) 2024**, 11(45)**:** e2402975.

Acknowledgements

We thank Shuimu BioSciences for assistance with X-ray data collection and structure determination. We acknowledge the DAKEWEI Flow Cytometry Core for cell sorting and analysis support. This work was supported by grants from the National Natural Science Foundation of China (Grant Number: 82204262).

Author Contributions

The study was conceived and supervised by the corresponding authors, Longlong Luo, Jiannan Feng, and Xiang Gao. Longlong Luo provided overall direction and oversight for the entire project from inception to completion. Jiannan Feng supervised the computational design strategy and the development of the MTIS paradigm. Xiang Gao guided the data interpretation, shaped the scientific discussion, and critically revised the manuscript.

Under this leadership, the project was executed by the co-first authors. Yangyihua Zhou and

Min Zhang performed the *in silico* design and algorithm development under the direction of Jiannan Feng. Yaowei Ma, Guojiang Chen and Yuting Zhang led the protein engineering and all *in vitro* characterization. Yangyihua Zhou, Chunxia Qiao and Xinying Li led the cellular and *in vivo* studies. Chaoyan Yao and Juan Tian performed immune-profiling analyses, and Ning Shi and Liang Zhang solved the crystal structure.

The manuscript was drafted by Yangyihua Zhou and Yi Zhou and was extensively revised and finalized under the guidance of Xiang Gao and Longlong Luo.

Yangyihua Zhou and Yaowei Ma contributed equally to this work. Longlong Luo, Jiannan Feng, and Xiang Gao are co-corresponding authors. Correspondence should be addressed to Longlong Luo (luolong_long@126.com), Jiannan Feng (fengjiannan1970@qq.com), and Xiang Gao (gaoxiang609@163.com), with lead correspondence directed to Longlong Luo.

Declaration of Competing Interests

The authors from the State Key Laboratory of National Security Specially Needed Medicines are inventors on a patent application covering the Fc_{95} platform and the MTIS design method (CN Patent Application No.: 202511569504X). The other authors declare no competing interests.

Data availability

Single-cell RNA sequencing data generated in this study have been deposited in the NCBI Sequence Read Archive (SRA) under BioProject accession PRJNA1371357 (sample accession numbers: SAMN53499638 and SAMN53499637).

Figures and Tables

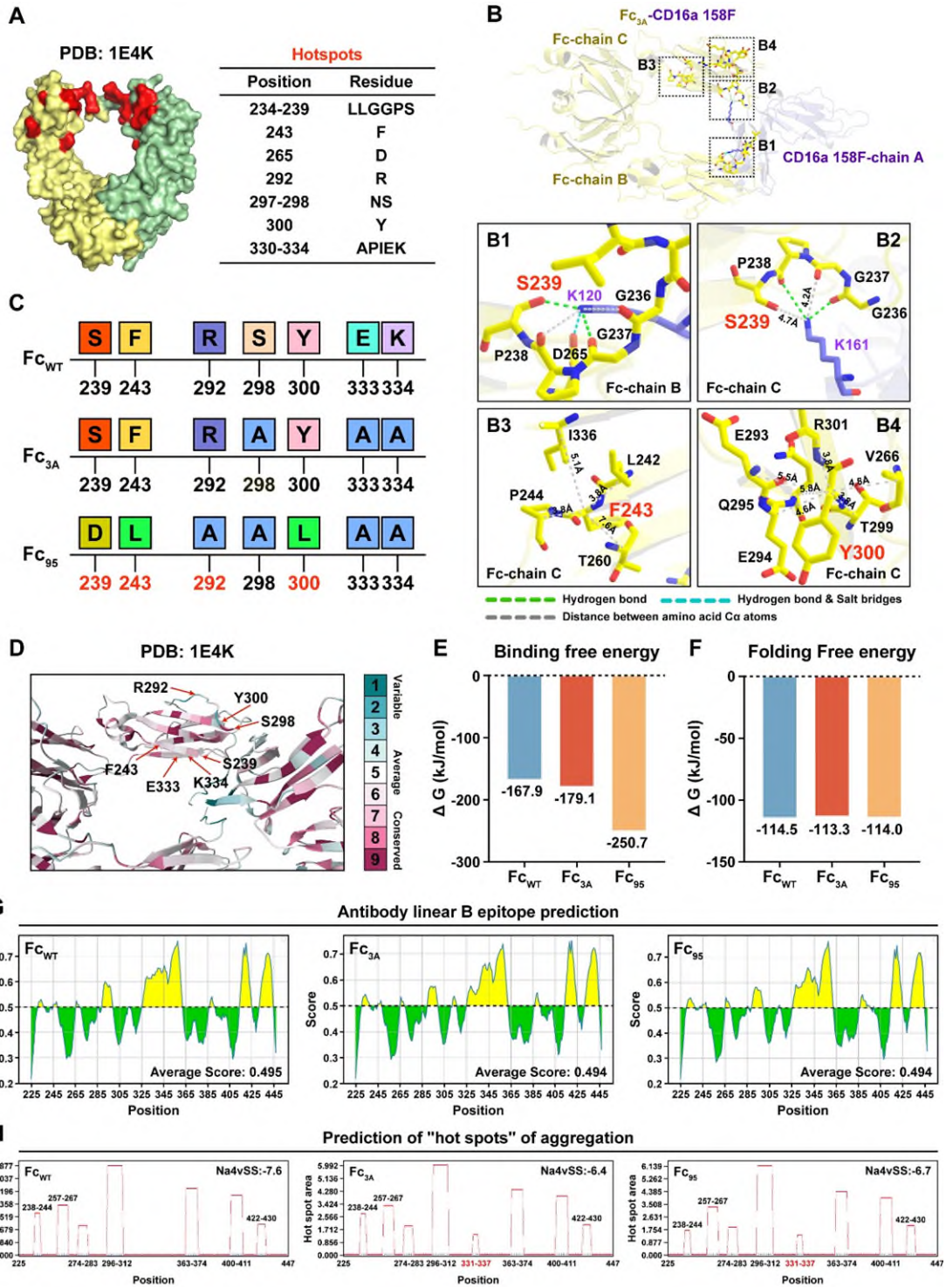

A
PDB: 1E4K
Hotspots
Position Residue
234-239 LLGGPS
243 F
265 D
292 R
297-298 NS
300 Y
330-334 APIEK
B
Fc3A-CD16a 158F
Fc-chain C
B4
B3
B2
B1
CD16a 158F-chain A
Fc-chain B
B1
S239
K120
G236
G237
P238
D265
Fc-chain B
B2
P238
G237
4.2Å
G236
S239
4.7Å
K161
Fc-chain C
B3
I336
5.1Å
L242
P244
3.8Å
F243
3.8Å
7.6Å
T260
Fc-chain C
B4
E293
R301
3.8Å
V266
5.5Å
5.8Å
4.8Å
Q295
4.6Å
3.8Å
T299
E294
Y300
Fc-chain C
Hydrogen bond
Hydrogen bond & Salt bridges
Distance between amino acid Cα atoms
C
FcWT S F R S Y E K
239 243 292 298 300 333 334
Fc3A S F R A Y A A
239 243 292 298 300 333 334
Fc95 D L A A L A A
239 243 292 298 300 333 334
D
PDB: 1E4K
R292
Y300
S298
F243
S239
E333
K334
Variable
Average
Conserved
E
Binding free energy
Δ G (kJ/mol)
-167.9
-179.1
-250.7
FcWT Fc3A Fc95
F
Folding Free energy
Δ G (kJ/mol)
-114.5
-113.3
-114.0
FcWT Fc3A Fc95
G
Antibody linear B epitope prediction
FcWT
Average Score: 0.495
Fc3A
Average Score: 0.494
Fc95
Average Score: 0.494
Score
Position
H
Prediction of "hot spots" of aggregation
FcWT
Na4vSS:-7.6
Fc3A
Na4vSS:-6.4
Fc95
Na4vSS:-6.7
Hot spot area
238-244
257-267
422-430
Position

Fig. 1. Rational design and *in silico* validation of the Fc_{95} variant via Microenvironment-Tuned Interface Sculpting (MTIS).

(A) Identification of the orthosteric binding sites for CD16a on the IgG1 Fc domain. The molecular surface of the Fc homodimer (PDB ID: 1E4K) is displayed with chains B and C in pale green and pale yellow. To clearly illustrate the binding interface, the CD16a receptor is not shown. Key interaction residues on the Fc domain (hotspots), constituting the engineering canvas, are highlighted in red and detailed in the adjacent table.

(B) Microenvironment analysis guiding rational mutations under the Physicochemical Matching principle. High-fidelity structural models (predicted by AlphaFold3) of the Fc_{3A} (yellow ribbon)-CD16a (purple ribbon) interface reveal local physicochemical liabilities. The analysis identified suboptimal packing of F243 in an aliphatic pocket and an energetic desolvation penalty for Y300, guiding their substitution with leucine (L). The S239D mutation was designed to create a new electrostatic interaction with K120/K161 on CD16a.

(C) Mutation map of the engineered Fc variants. Amino acid substitutions defining the 'primed' Fc_{3A} scaffold and the final Fc_{95} variant are shown. All positions adhere to the EU numbering scheme.

(D) Evolutionary conservation analysis validates site selection. Conservation scores for the Fc domain, obtained from the ConSurf-DB using the 1E4K structure as input, are mapped onto the surface. The color scale represents the evolutionary rate, from highly variable (cyan, grade 1) to strictly conserved (purple, grade 9). All four engineered residues (arrow pointing) are located in regions of intermediate-to-high variability (grades 3−7), confirming their suitability for modification.

(E) Predicted binding affinity enhancement for Fc_{95}. Binding free energies (ΔG) for Fc variants to CD16a were calculated from 100-ns molecular dynamics (MD) simulations. The results predict a substantial increase in affinity for Fc_{95}, validating the Functional Optimization pillar of the MTIS framework.

(F) Intrinsic stability is preserved in the Fc_{95} variant. The change in folding free energy ($\Delta\Delta G$) relative to wild-type (WT) was calculated for the Fc monomers. The negligible $\Delta\Delta G$ for Fc_{95} (<1 kJ/mol) indicates that the mutations do not compromise the protein's intrinsic stability, satisfying a key objective of the Structural Integrity pillar.

(G) *In silico* prediction of linear B-cell epitopes. Analysis using the Bepipred 2.0 tool (IEDB Analysis Resource) shows nearly identical average epitope propensity scores across the Fc sequence for all variants, suggesting no new linear epitopes were created.

(H) Aggregation propensity analysis indicates low risk for Fc_{95}. The normalized aggregation score (Na4vSS) was calculated using the AGGREGATE algorithm. A more negative score indicates lower aggregation propensity. The analysis shows that the modest aggregation risk inherited from the Fc_{3A} scaffold is partially mitigated in Fc_{95}, with all variants remaining in the low-risk category. The predicted aggregation-prone region (red bar) is highlighted.

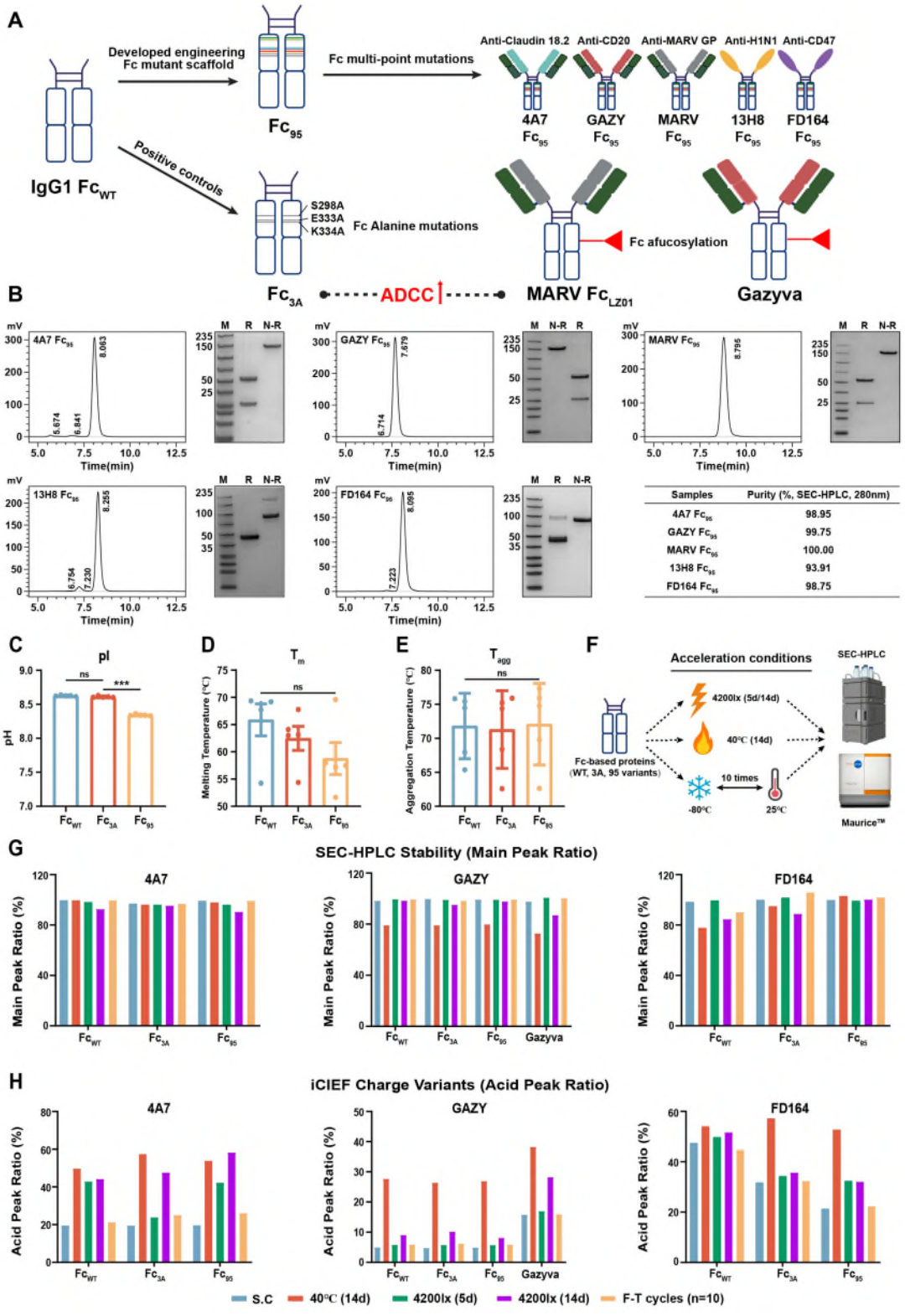

A
Developed engineering Fc mutant scaffold
Fc multi-point mutations
Anti-Claudin 18.2
Anti-CD20
Anti-MARV GP
Anti-H1N1
Anti-CD47
4A7 Fc95
GAZY Fc95
MARV Fc95
13H8 Fc95
FD164 Fc95
IgG1 FcWT
Positive controls
S298A
E333A
K334A
Fc Alanine mutations
Fc afucosylation
B
Fc3A
ADCC
MARV FcLZ01
Gazyva
Time(min)
Samples
Purity (%, SEC-HPLC, 280nm)
4A7 Fc95 98.95
GAZY Fc95 99.75
MARV Fc95 100.00
13H8 Fc95 93.91
FD164 Fc95 98.75
C
pI
D
Tm
Melting Temperature (℃)
E
Tagg
Aggregation Temperature (℃)
F
Acceleration conditions
SEC-HPLC
Fc-based proteins (WT, 3A, 95 variants)
4200lx (5d/14d)
40℃ (14d)
10 times
-80℃
25℃
Maurice™
G
SEC-HPLC Stability (Main Peak Ratio)
4A7
GAZY
FD164
Main Peak Ratio (%)
H
iCIEF Charge Variants (Acid Peak Ratio)
Acid Peak Ratio (%)
S.C
40℃ (14d)
4200lx (5d)
4200lx (14d)
F-T cycles (n=10)

Figure 2. The Fc_{95} scaffold is a versatile and robust engineering platform.

(A) Schematic overview of the engineering strategy. The enhanced-ADCC Fc_{95} scaffold was developed *via* multi-point mutations from a wild-type IgG1 Fc (Fc_{WT}), alongside an ADCC-positive Fc_{3A} control. To demonstrate versatility, the Fc_{95} scaffold was fused to five distinct targeting moieties: three full-length antibodies (anti-Claudin18.2, anti-CD20, anti-MARV GP), one nanobody (anti-H1N1 HA), and one receptor ectodomain (SIRPα targeting human CD47). Afucosylated antibodies (Gazyva, MARV Fc_{LZ01}) were included as benchmark control for ADCC enhancement.

(B) Representative SEC-HPLC profiles performed at 30°C and non-reducing (N-R)/reducing (R) SDS-PAGE gels of the five Fc_{95}-based proteins.

(C-E) The Fc_{95} scaffold possesses predictable and acceptable physicochemical properties. Bar graphs show a comparative analysis of **(C)** isoelectric point (pI), **(D)** thermal stability (T_m) and **(E)** aggregation onset temperature (T_{agg}) across all 15 engineered proteins (individual dots represent different constructs).

(F-H) The Fc_{95} scaffold demonstrates stability comparable to Fc_{WT} under accelerated stress conditions. **(F)** Schematic of the stress tests performed on the Fc-based variants. **(G)** Physical stability of 4A7 Fc_{95}, GAZY Fc_{95} and FD164 Fc_{95}, assessed by the main peak ratio in SEC-HPLC. **(H)** Chemical stability of the same variants, assessed by the change in acid peak ratio (**iCIEF**). **S.C:** Standard Conditions (e.g., 4°C, 14d).

Data in panels **C**−**E** are pooled from two independent experiments and presented as mean ± SEM. Data in panels **G** and **H** represent values from independent stress evaluations. Statistical significance in (**C**−**E**) was determined by one-way ANOVA; ns, not significant; ***$P < 0.001$.

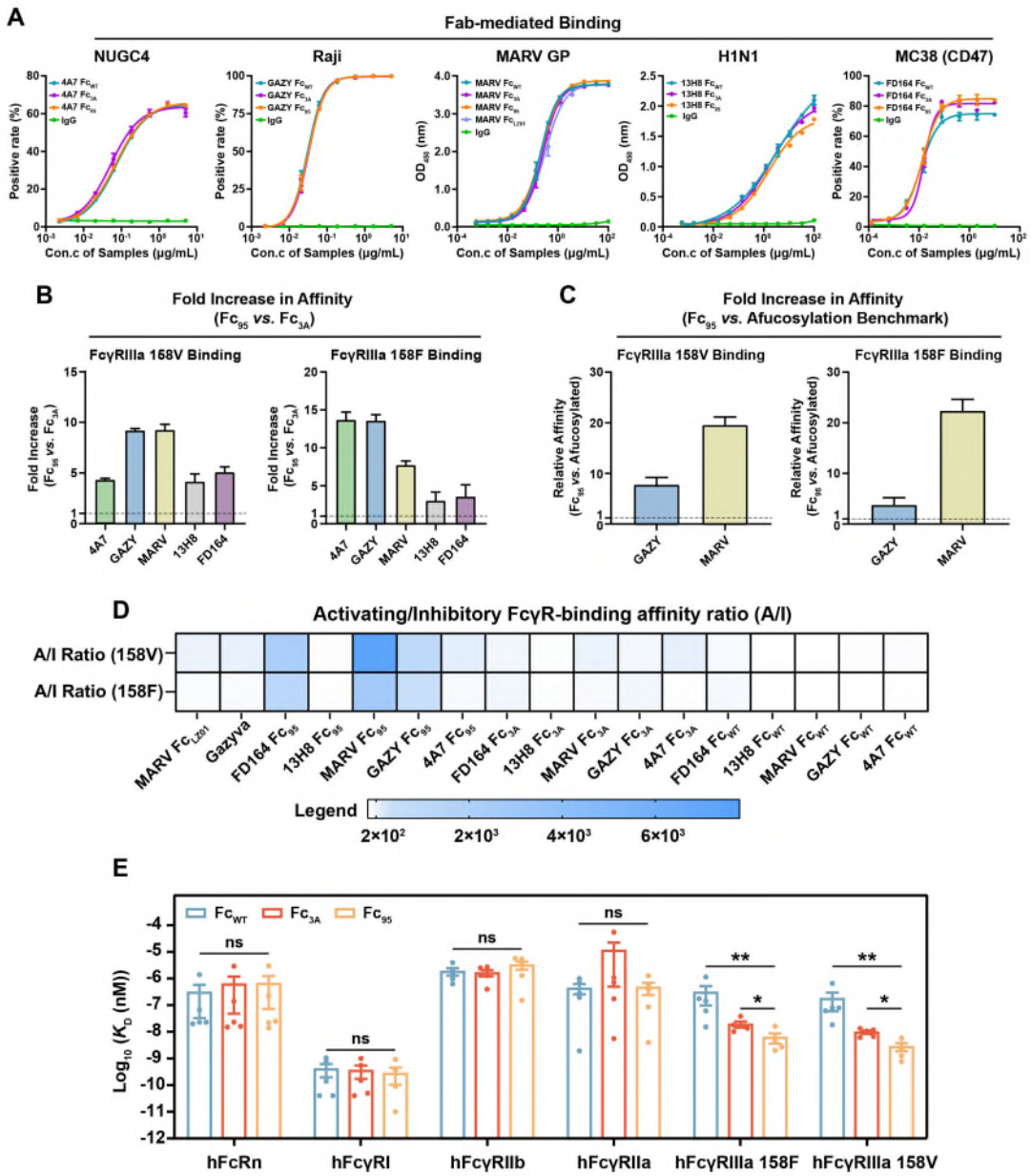

A
Fab-mediated Binding
NUGC4
Raji
MARV GP
H1N1
MC38 (CD47)
Positive rate (%)
OD450 (nm)
Con.c of Samples (μg/mL)
B
Fold Increase in Affinity
(Fc95 vs. Fc3A)
FcγRIIIa 158V Binding
FcγRIIIa 158F Binding
Fold Increase
4A7
GAZY
MARV
13H8
FD164
C
Fold Increase in Affinity
(Fc95 vs. Afucosylation Benchmark)
Relative Affinity
(Fc95 vs. Afucosylated)
D
Activating/Inhibitory FcγR-binding affinity ratio (A/I)
A/I Ratio (158V)
A/I Ratio (158F)
Gazyva
Legend
2×10²
2×10³
4×10³
6×10³
E
Log10 (KD (nM))
ns
**
*
hFcRn
hFcγRI
hFcγRIIb
hFcγRIIa
hFcγRIIIa 158F
hFcγRIIIa 158V

Figure 3. The Fc_{95} Platform Selectively Enhances FcγRIIIa Affinity While Preserving Key Binding Functions.

(A) Preservation of antigen binding. Fab-mediated binding curves for all five constructs, measured by flow cytometry or ELISA, show that Fc engineering did not alter antigen recognition, as the Fc_{WT}, Fc_{3A}, and Fc_{95} variants for each target exhibit identical binding profiles.

(B) Superiority over the conventional Fc_{3A} mutant. Fold-changes in binding affinity for FcγRIIIa (158V and 158F) of Fc_{95} variants, calculated relative to the Fc_{3A} mutants. A value >1 indicates higher affinity than Fc_{3A}. The Fc_{95} variants consistently demonstrate the greatest affinity enhancement.

(C) Superiority over the afucosylation benchmark. Fold-changes in binding affinity for FcγRIIIa (158V and 158F) of Fc_{95} variants relative to their respective afucosylated benchmarks (Gazyva and MARV Fc_{LZ01}). A value >1 indicates superiority over afucosylation.

(D) Enhanced Activating/Inhibitory (A/I) ratio. Heatmap of the A/I ratio (calculated as K_D of FcγRIIb / K_D of FcγRIIIa) for both 158V and 158F allotypes. Darker blue indicates a stronger pro-activating profile. Fc_{95} variants consistently exhibit the most favorable A/I ratios compared to Fc_{3A} and afucosylated formats.

(E) Platform-wide selectivity and consistency. Summary of mean binding affinities ($\log_{10} K_D$) across all five antibody constructs for the Fc_{WT}, Fc_{3A}, and Fc_{95} formats. Lower $\log_{10} K_D$ Values indicate higher binding affinity. Binding to a panel of human FcγRs and FcRn is shown. Fc_{95} selectively and significantly enhances affinity for the activating receptors FcγRIIIa-158V and -158F, while having no significant effect (ns) on FcγRIIa, FcγRI, FcRn or the inhibitory receptor FcγRIIb.

Data are representative of three independent experiments (**A–E**). Values are presented as mean ± standard deviation (SD) (**E**) of technical duplicates (**A–C**). Each dot within the bar represents the binding affinity value for one of the five target antibodies (**E**). Statistical significance was determined by one-way ANOVA (**E**). ns, not significant; $*P < 0.05$; $**P < 0.01$; $***P < 0.001$.

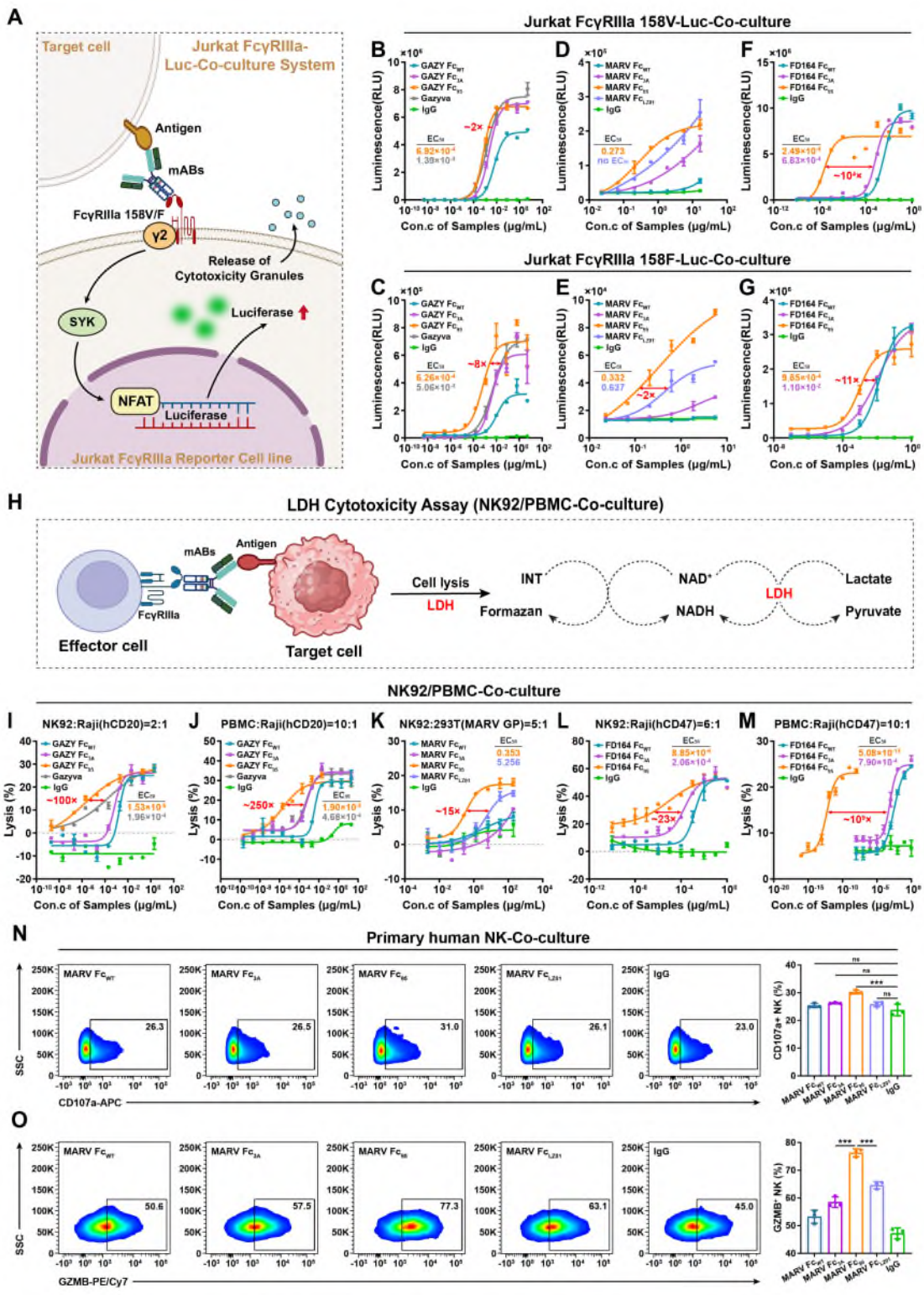

A
Target cell
Jurkat FcγRIIIa-Luc-Co-culture System
Antigen
mABs
FcγRIIIa 158V/F
γ2
Release of Cytotoxicity Granules
SYK
Luciferase
NFAT
Luciferase
Jurkat FcγRIIIa Reporter Cell line
Jurkat FcγRIIIa 158V-Luc-Co-culture
Jurkat FcγRIIIa 158F-Luc-Co-culture
Luminescence(RLU)
Con.c of Samples (μg/mL)
GAZY Fc
MARV Fc
FD164 Fc
Gazyva
IgG
H
LDH Cytotoxicity Assay (NK92/PBMC-Co-culture)
mABs
Antigen
FcγRIIIa
Effector cell
Target cell
Cell lysis
LDH
INT
Formazan
NAD+
NADH
LDH
Lactate
Pyruvate
NK92/PBMC-Co-culture
NK92:Raji(hCD20)=2:1
PBMC:Raji(hCD20)=10:1
NK92:293T(MARV GP)=5:1
NK92:Raji(hCD47)=6:1
PBMC:Raji(hCD47)=10:1
Lysis (%)
Con.c of Samples (μg/mL)
Primary human NK-Co-culture
SSC
CD107a-APC
CD107a+ NK (%)
GZMB-PE/Cy7
GZMB+ NK (%)

Figure 4. The Fc_{95} Platform Demonstrates Superior and Broad Effector Function *in vitro*.

(A) Schematic of the Jurkat FcγRIIIa reporter gene assay used to quantify ADCC activity.

(B–G) ADCC activity measured by the reporter assay using Jurkat cells expressing high-affinity FcγRIIIa 158V (B, D, F) or low-affinity FcγRIIIa 158F (C, E, G). The assay was performed with target cells and various antibody formats targeting **(B–C)** CD20 (GAZY), **(D–E)** Marburg virus glycoprotein (MARV GP), and **(F–G)** CD47 (FD164).

(H) Schematic of the primary cell co-culture cytotoxicity assay (LDH release assay).

(I–M) ADCC-mediated lysis of target cells by various effector cells. (I–J) Lysis of Raji (hCD20) target cells by NK92 effectors **(I)** or human PBMCs **(J)** mediated by anti-CD20 (GAZY) variants. **(K)** Lysis of 293T (MARV GP) target cells by NK92 effectors mediated by anti-MARV GP (MARV) variants. **(L–M)** Lysis of Raji (hCD47) target cells by NK92 effectors **(L)** or human PBMCs **(M)** mediated by anti-CD47 (FD164) variants.

Data are representative of three (**B–G**, **I–M**) or two (**N**, **O**) independent experiments. Values are presented as mean ± standard error of the mean (SEM) of technical duplicates (**B–G**, **I, J**, **L**, **M**) or triplicates (**K**, **N**, **O**). EC_{50} values are expressed in μg/mL. Statistical significance was determined by one-way ANOVA (N, O). ns, not significant; ***$P < 0.001$.

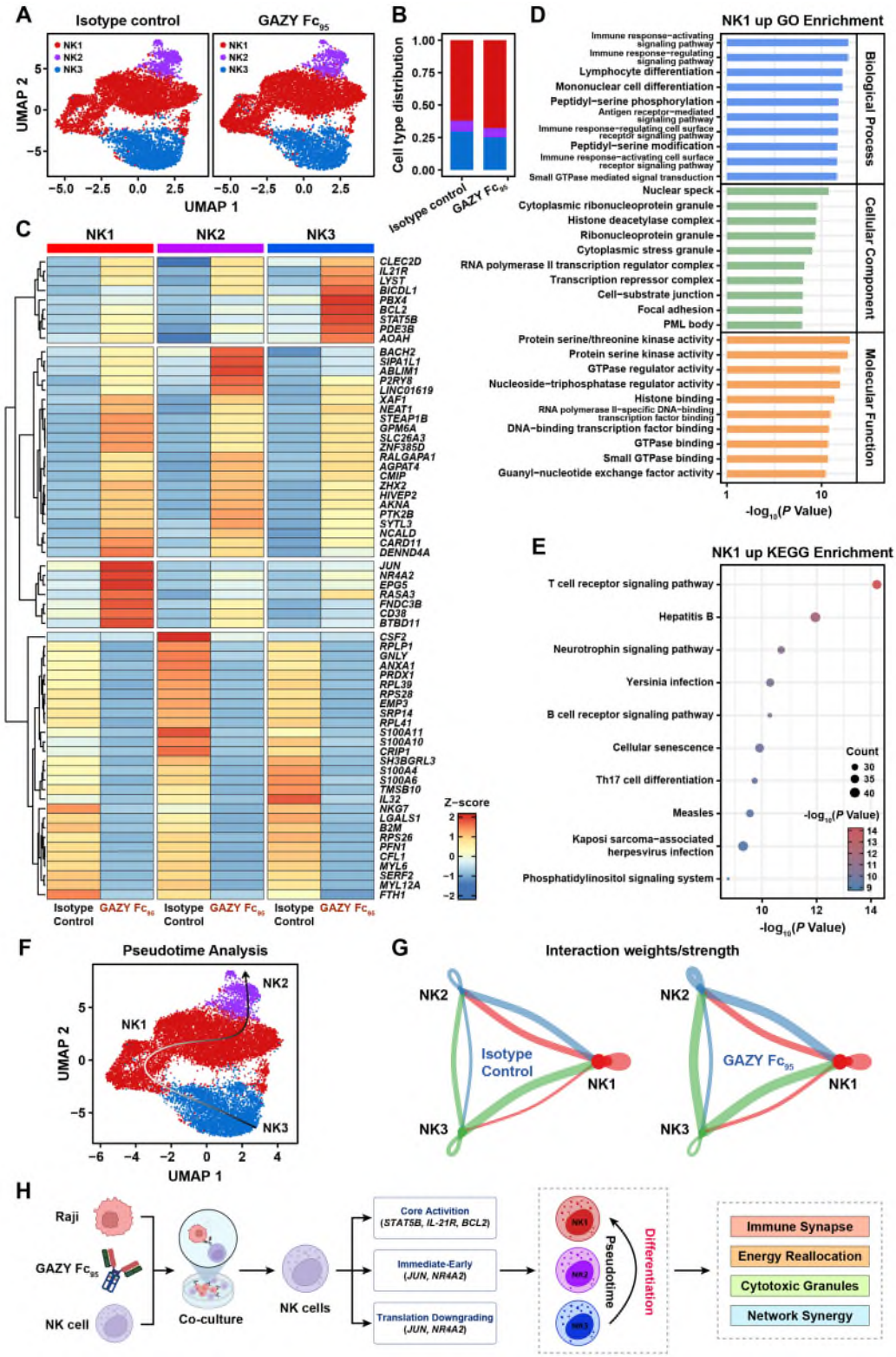

A
Isotype control
GAZY Fc95
NK1
NK2
NK3
UMAP 2
UMAP 1
B
Cell type distribution
Isotype control
GAZY Fc95
C
NK1
NK2
NK3
CLEC2D
IL21R
LYST
BICDL1
PBX4
BCL2
STAT5B
PDE3B
AOAH
BACH2
SIPA1L1
ABLIM1
P2RY8
LINC01619
XAF1
NEAT1
STEAP1B
GPM6A
SLC26A3
ZNF385D
RALGAPA1
AGPAT4
CMIP
ZHX2
HIVEP2
AKNA
PTK2B
SYTL3
NCALD
CARD11
DENND4A
JUN
NR4A2
EPG5
RASA3
FNDC3B
CD38
BTBD11
CSF2
RPLP1
GNLY
ANXA1
PRDX1
RPL39
RPS28
EMP3
SRP14
RPL41
S100A11
S100A10
CRIP1
SH3BGRL3
S100A4
S100A6
TMSB10
IL32
NKG7
LGALS1
B2M
RPS26
PFN1
CFL1
MYL6
SERF2
MYL12A
FTH1
Isotype Control
GAZY Fc95
Z-score
D
NK1 up GO Enrichment
Immune response-activating signaling pathway
Immune response-regulating signaling pathway
Lymphocyte differentiation
Mononuclear cell differentiation
Peptidyl-serine phosphorylation
Antigen receptor-mediated signaling pathway
Immune response-regulating cell surface receptor signaling pathway
Peptidyl-serine modification
Immune response-activating cell surface receptor signaling pathway
Small GTPase mediated signal transduction
Nuclear speck
Cytoplasmic ribonucleoprotein granule
Histone deacetylase complex
Ribonucleoprotein granule
Cytoplasmic stress granule
RNA polymerase II transcription regulator complex
Transcription repressor complex
Cell-substrate junction
Focal adhesion
PML body
Protein serine/threonine kinase activity
Protein serine kinase activity
GTPase regulator activity
Nucleoside-triphosphatase regulator activity
Histone binding
RNA polymerase II-specific DNA-binding transcription factor binding
DNA-binding transcription factor binding
GTPase binding
Small GTPase binding
Guanyl-nucleotide exchange factor activity
Biological Process
Cellular Component
Molecular Function
-log10(P Value)
E
NK1 up KEGG Enrichment
T cell receptor signaling pathway
Hepatitis B
Neurotrophin signaling pathway
Yersinia infection
B cell receptor signaling pathway
Cellular senescence
Th17 cell differentiation
Measles
Kaposi sarcoma-associated herpesvirus infection
Phosphatidylinositol signaling system
Count
-log10(P Value)
F
Pseudotime Analysis
NK1
NK2
NK3
UMAP 2
UMAP 1
G
Interaction weights/strength
NK2
Isotype Control
NK1
NK3
NK2
GAZY Fc95
NK1
NK3
H
Raji
GAZY Fc95
NK cell
Co-culture
NK cells
Core Activition (STAT5B, IL-21R, BCL2)
Immediate-Early (JUN, NR4A2)
Translation Downgrading (JUN, NR4A2)
Pseudotime
Differentiation
Immune Synapse
Energy Reallocation
Cytotoxic Granules
Network Synergy

Figure 5. Single-cell transcriptomic analysis reveals GAZY Fc_{95}-mediated NK cell reprogramming.

(A) UMAP visualization of integrated NK cells from anti-SEB isotype control (left) and GAZY Fc_{95}-treated (right) samples, colored by subset identity (NK1, red; NK2, purple; NK3, blue).

(B) Stacked bar plots showing the relative proportions of NK1, NK2, and NK3 subsets under each condition.

(C) Heatmap of the top 20 most upregulated genes per subset following GAZY Fc_{95} stimulation, with samples hierarchically clustered by expression similarity.

(D) Gene Ontology (GO) enrichment analysis of NK1-upregulated genes, grouped into Biological Process (BP, blue), Cellular Component (CC, green), and Molecular Function (MF, orange) categories.

(E) KEGG pathway enrichment of NK1-upregulated genes; bubble size denotes the number of genes per pathway, and bubble color encodes statistical significance ($-\log_{10} P$ value).

(F) UMAP maps of pseudotime trajectory reconstruction showing a progression from NK3 to NK1 states.

(G) Circo-style network diagrams depicting inferred inter-subset communication strength under isotype control (left) and GAZY Fc_{95} treatment (right). Line thickness represents interaction weight; node size reflects the relative abundance of each subset.

(H) Schematic model summarizing the multi-layered mechanisms by which GAZY Fc_{95} enhances NK cell cytotoxicity, including NK3-to-NK1 conversion, installation of a pan-subset activation program, trajectory-directed maturation supported by chaperones, and reinforcement of intercellular communication.

Single-cell RNA sequencing data generated in this study have been deposited in the NCBI Sequence Read Archive (SRA) under BioProject accession PRJNA1371357 (sample accession numbers: SAMN53499638 and SAMN53499637).

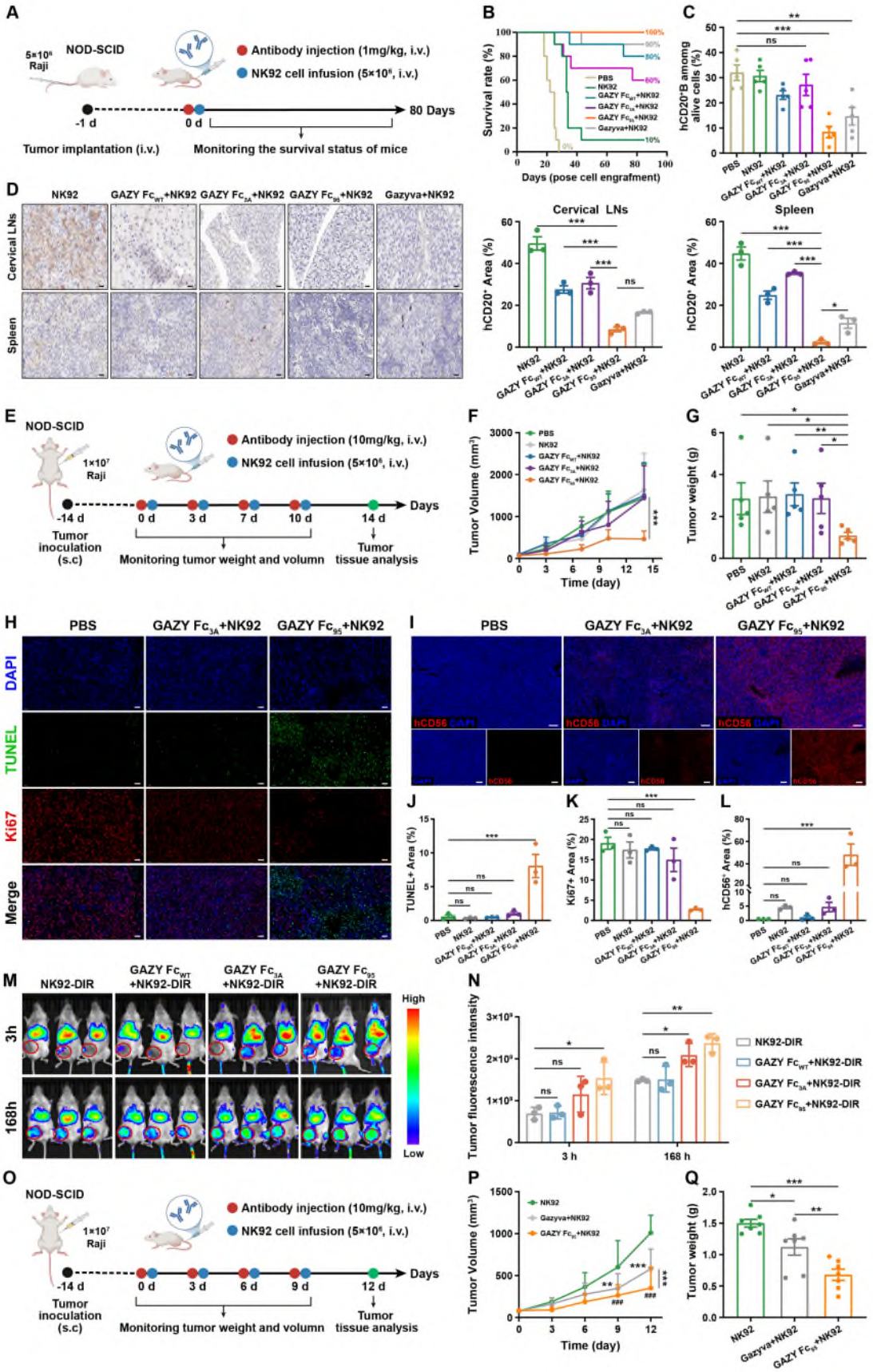

A
NOD-SCID
Antibody injection (1mg/kg, i.v.)
NK92 cell infusion (5×10⁶, i.v.)
80 Days
Tumor implantation (i.v.)
Monitoring the survival status of mice
B
Survival rate (%)
Days (pose cell engrafment)
PBS
NK92
GAZY Fc95+NK92
Gazyva+NK92
C
hCD20⁺B among alive cells (%)
D
NK92
GAZY Fc95+NK92
Gazyva+NK92
Cervical LNs
Spleen
Cervical LNs
Spleen
hCD20⁺ Area (%)
E
NOD-SCID
Antibody injection (10mg/kg, i.v.)
NK92 cell infusion (5×10⁶, i.v.)
Days
Tumor inoculation (s.c)
Monitoring tumor weight and volumn
Tumor tissue analysis
F
Tumor Volume (mm³)
Time (day)
G
Tumor weight (g)
H
PBS
GAZY Fc3A+NK92
GAZY Fc95+NK92
DAPI
TUNEL
Ki67
Merge
I
hCD56
J
TUNEL+ Area (%)
K
Ki67+ Area (%)
L
hCD56⁺ Area (%)
M
NK92-DIR
GAZY Fc95 +NK92-DIR
3h
168h
High
Low
N
Tumor fluorescence intensity
3 h
168 h
O
NOD-SCID
Antibody injection (10mg/kg, i.v.)
NK92 cell infusion (5×10⁶, i.v.)
Days
Tumor inoculation (s.c)
Monitoring tumor weight and volumn
Tumor tissue analysis
P
Tumor Volume (mm³)
Time (day)
Q
Tumor weight (g)

Figure 6. GAZY Fc_{95} Enhances Exogenous NK Cell-Mediated Anti-Tumor Responses in Immunodeficient Mice.

(A) Schematic of the disseminated Raji B cell lymphoma xenograft model used to evaluate systemic disease control.

(B) GAZY Fc_{95} prolongs survival in the disseminated Raji model. Kaplan-Meier survival analysis following a single administration of antibody (1 mg/kg) in combination with NK92 cells, n = 10/group.

(C) Rapid systemic clearance of circulating tumor cells by GAZY Fc_{95}. Quantification of circulating $hCD20^+$ Raji cells by flow cytometry 7 days post injection, n = 5/group. Representative dot plots for all treatment groups are shown in **Extended data Fig. 1**. Gating strategies for all groups are available in the Supplemental **Fig. S6A.**

(D) GAZY Fc_{95} effectively clears tumor burden from lymphoid organs. Representative immunohistochemistry (IHC) staining for $hCD20^+$ tumor cells in cervical lymph nodes and spleens 30 days post treatment, showing near-complete clearance in the GAZY Fc_{95} group. Scale bars, 20 μm.

(E) Schematic of the subcutaneous Raji xenograft model used to evaluate efficacy against established solid tumors.

(F) GAZY Fc_{95} imposes dominant control over solid tumor growth. Tumor growth curves for mice treated with antibody (10 mg/kg) and NK92 cells, n = 5/group.

(G) Superior efficacy of GAZY Fc_{95} confirmed by endpoint tumor weights, n = 5/group.

(H−I) GAZY Fc_{95} remodels the tumor microenvironment by driving NK cell infiltration and inducing a functional switch from proliferation to apoptosis. Representative immunofluorescence images of tumor sections showing **(H)** apoptosis (TUNEL, green) and proliferation (Ki67, red), and **(I)** tumor-infiltrating human NK cells (hCD56, red). Scale bars, 50 μm (**H**) and 100 μm (**I**).

(J−L) Quantification of immunofluorescence staining confirms the shift in the tumor microenvironment. Quantification of **(J)** $TUNEL^+$ apoptotic cells, **(K)** $Ki67^+$ proliferative cells, and **(L)** $hCD56^+$ NK cell density, n = 3 biological replicates.

(M−N) GAZY Fc_{95} drives rapid and sustained NK cell accumulation at the tumor site. **(M)** Representative IVIS imaging of mice bearing subcutaneous tumors injected with DIR-labeled

NK92 cells and indicated antibodies. **(N)** Quantification of tumor-localized fluorescence signal at 3 h and 168 h post injection, n = 3/group.

(O−Q) Head-to-head comparison demonstrates the therapeutic superiority of GAZY Fc_{95} over Gazyva. **(O)** Schematic of the therapeutic model. **(P)** Tumor growth curves and **(Q)** endpoint tumor weights showing significantly greater tumor control by GAZY Fc_{95}, n = 7/group.

Data in panels (**B**) are pulled from two independent experiments. Data are representative of two or three independent experiments and are mean ± standard error (**C, D, F, G, J−L, N, P, Q**). Each dot represents one mouse (**C, F, G, N, P, Q**). Statistical analysis was performed using two-way ANOVA with Tukey's multiple comparisons test (**F, P**), log-rank (Mantel-Cox) test (**B**) or ordinary one-way ANOVA with multiple comparisons test (**C, D, G, J−L, N, Q**), ns, not significant, $*P < 0.05$, $**P < 0.01$, $***P < 0.001$, $****P < 0.0001$.

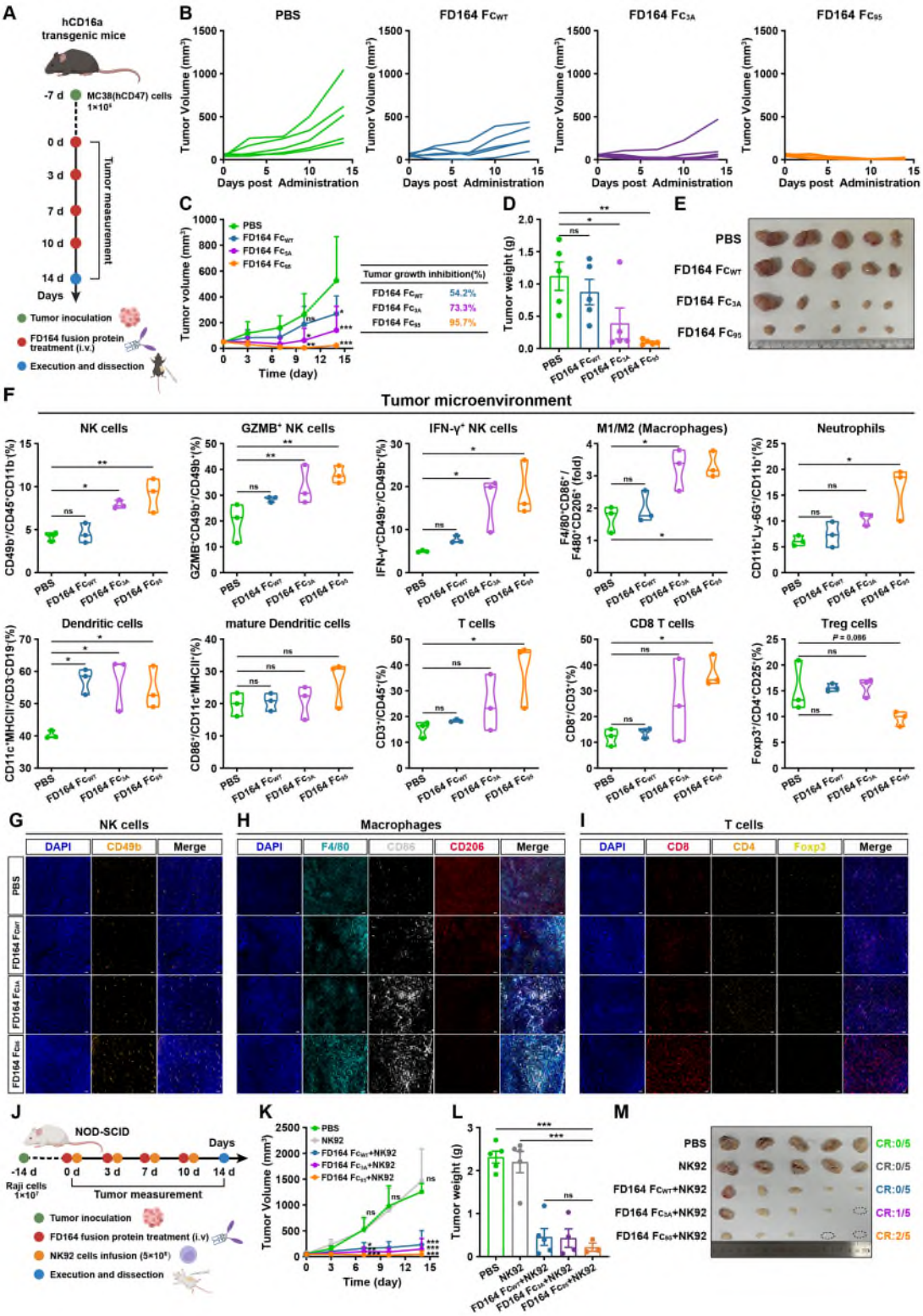

A
hCD16a transgenic mice
-7 d
MC38(hCD47) cells 1×10⁶
0 d
3 d
7 d
10 d
14 d
Days
Tumor measurement
Tumor inoculation
FD164 fusion protein treatment (i.v.)
Execution and dissection
B
PBS
FD164 FcWT
FD164 Fc3A
FD164 Fc95
Tumor Volume (mm³)
Days post Administration
C
Tumor volume (mm³)
Time (day)
Tumor growth inhibition(%)
FD164 FcWT 54.2%
FD164 Fc3A 73.3%
FD164 Fc95 95.7%
D
Tumor weight (g)
E
F
Tumor microenvironment
NK cells
GZMB⁺ NK cells
IFN-γ⁺ NK cells
M1/M2 (Macrophages)
Neutrophils
Dendritic cells
mature Dendritic cells
T cells
CD8 T cells
Treg cells
G
NK cells
DAPI
CD49b
Merge
H
Macrophages
F4/80
CD86
CD206
I
T cells
CD8
CD4
Foxp3
J
NOD-SCID
-14 d
Raji cells 1×10⁷
0 d
3 d
7 d
10 d
14 d
Days
Tumor measurement
Tumor inoculation
FD164 fusion protein treatment (i.v)
NK92 cells infusion (5×10⁶)
Execution and dissection
K
PBS
NK92
FD164 FcWT+NK92
FD164 Fc3A+NK92
FD164 Fc95+NK92
Tumor Volume (mm³)
Time (day)
L
Tumor weight (g)
M
PBS
NK92
FD164 FcWT+NK92
FD164 Fc3A+NK92
FD164 Fc95+NK92
CR:0/5
CR:0/5
CR:0/5
CR:1/5
CR:2/5

Figure 7. The Superior Anti-Tumor Efficacy of FD164 Fc_{95} is Driven by its Unique Ability to Orchestrate a Comprehensive Innate and Adaptive Immune Assault.

(A) Schematic of the *in vivo* efficacy study in hCD16a transgenic mice using the MC38 colon adenocarcinoma model.

(B–E) FD164 Fc_{95} treatment results in profound tumor growth inhibition. **(B)** Tumor growth curves for individual mice. **(C)** Mean tumor growth curves with calculated Tumor Growth Inhibition (TGI) percentages. **(D)** Endpoint tumor weights at day 14. **(E)** Representative images of explanted tumors. n=5/group.

(F) Quantification of tumor-infiltrating immune populations by flow cytometry. Violin plots show the percentage or ratio of key innate and adaptive immune cells, including total NK cells, activated ($GZMB^+$, IFN-γ^+) NK cells, M1/M2 macrophage ratio, neutrophils, dendritic cells (DCs), mature DCs, total T cells, $CD8^+$ T cells, and regulatory T cells (Tregs). Representative dot plots for all conditions are shown in **Extended data Fig. 2**. Gating strategies for all groups are available in the Supplemental **Fig. S7C–E.**

(G–I) Representative immunofluorescence images visualizing immune cell infiltration and state within the tumor microenvironment. **(G)** NK cell infiltration, stained for DAPI (blue) and CD49b (Orange). **(H)** Macrophage populations, stained for DAPI (blue), pan-macrophage marker F4/80 (cyan), M1 marker CD86 (white), and M2 marker CD206 (red). **(I)** T-cell populations, stained for DAPI (blue), cytotoxic T cells (CD8, red), helper T cells (CD4, orange), and regulatory T cells (Foxp3, yellow). Scale bars, 100 μm.

(J–M) An *in vivo* study in immunodeficient NOD-SCID mice to isolate the contribution of NK cell-mediated activity. **(J)** Schematic of the subcutaneous Raji xenograft model with co-injected NK92 cells. **(K)** Tumor growth curves. **(L)** Endpoint tumor weights. **(M)** Representative images of explanted tumors with noted Complete Regression (CR) rates. n=5/group.

All data are representative of two independent experiments and are mean ± standard error (**B–E, F–I, K–M**). Each dot represents one mouse (**C, D, F, K, L**). Statistical analysis was performed using two-way ANOVA with Tukey's multiple comparisons test (**C, K**) or ordinary one-way ANOVA with multiple comparisons test (**D, L, F**), ns, not significant, $*P < 0.05$, $**P < 0.01$, $***P < 0.001$, $****P < 0.0001$.

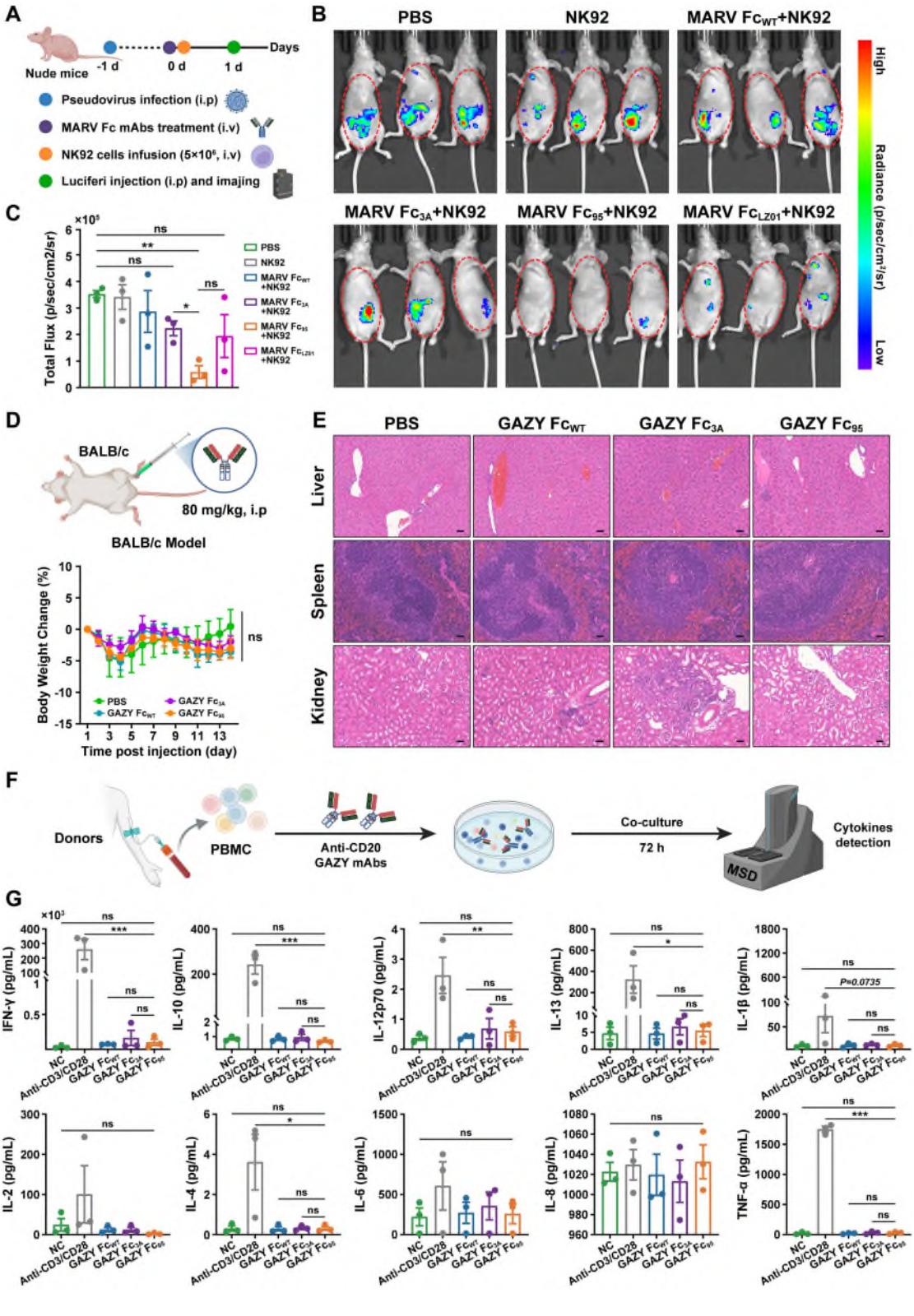

A
Nude mice
-1 d
0 d
1 d
Days
Pseudovirus infection (i.p)
MARV Fc mAbs treatment (i.v)
NK92 cells infusion (5×10⁶, i.v)
Luciferi injection (i.p) and imajing
B
PBS
NK92
MARV FcWT+NK92
MARV Fc3A+NK92
MARV Fc95+NK92
MARV FcLZ01+NK92
High
Radiance (p/sec/cm²/sr)
Low
C
Total Flux (p/sec/cm2/sr)
PBS
NK92
MARV FcWT +NK92
MARV Fc3A +NK92
MARV Fc95 +NK92
MARV FcLZ01 +NK92
D
BALB/c
80 mg/kg, i.p
BALB/c Model
Body Weight Change (%)
Time post injection (day)
PBS
GAZY Fc3A
GAZY FcWT
GAZY Fc95
E
PBS
GAZY FcWT
GAZY Fc3A
GAZY Fc95
Liver
Spleen
Kidney
F
Donors
PBMC
Anti-CD20
GAZY mAbs
Co-culture
72 h
MSD
Cytokines
detection
G
IFN-γ (pg/mL)
IL-10 (pg/mL)
IL-12p70 (pg/mL)
IL-13 (pg/mL)
IL-1β (pg/mL)
IL-2 (pg/mL)
IL-4 (pg/mL)
IL-6 (pg/mL)
IL-8 (pg/mL)
TNF-α (pg/mL)
P=0.0735
NC
Anti-CD3/CD28
GAZY FcWT
GAZY Fc3A
GAZY Fc95

Figure 8. The Fc_{95} platform combines potent antiviral efficacy with a favorable safety profile.

(A−C) The Fc_{95} platform confers superior antiviral potency in a stringent Marburg pseudovirus challenge model. Mice were treated with 10 mg/kg of the indicated MARV antibody variants (Fc_{WT}, Fc_{3A}, Fc_{LZ01}, Fc_{95}) or a vehicle control 24 hours post-infection. **(A)** A schematic of the experimental timeline. **(B)** Representative bioluminescence images captured by an IVIS imaging system on day 1, showing viral load. **(C)** Quantification of total radiance from each treatment group (n=3). Only the MARV Fc_{95} group achieved a profound and statistically significant reduction in viral load compared to the control.

(D−G) The Fc_{95} platform demonstrates a robust safety and low immunotoxicity profile. **(D)** Body weight changes in BALB/c mice (n=3 per group) following a single high-dose (80 mg/kg) intraperitoneal injection of the indicated GAZY antibody variants or PBS, showing no treatment-related adverse effects.

(E) Representative H&E staining of liver, spleen, and kidney sections from mice in (**D**), collected on day 14. The GAZY Fc_{95} group shows a clean histopathological profile comparable to controls, whereas the GAZY Fc_{3A} group exhibits signs of mild spleen inflammation and renal tubular atrophy. Scale bars, 50 μm.

(F−G) *In vitro* cytokine release from human PBMCs of three healthy donors incubated for 72 hours with 1000 nM of the indicated GAZY Fc variants. The concentrations of IFN-γ, IL-10, IL-12p70, IL-13, IL-1β, IL-2, IL-4, IL-6, IL-8 and TNF-α in the supernatant were quantified. GAZY Fc_{95} did not induce significant cytokine release, showing a profile indistinguishable from the NC (negative control, PBS). Anti-CD3/CD28 served as the positive control.

Data are mean ± standard error (**C, D, G**), represent two independent experiments (**B−E**) or three donors (**G**), and were analyzed by one-way ANOVA (**C, G**) or two-way ANOVA (**D**), ns, no significant, $*P < 0.05$, $**P < 0.01$, $***P < 0.001$.

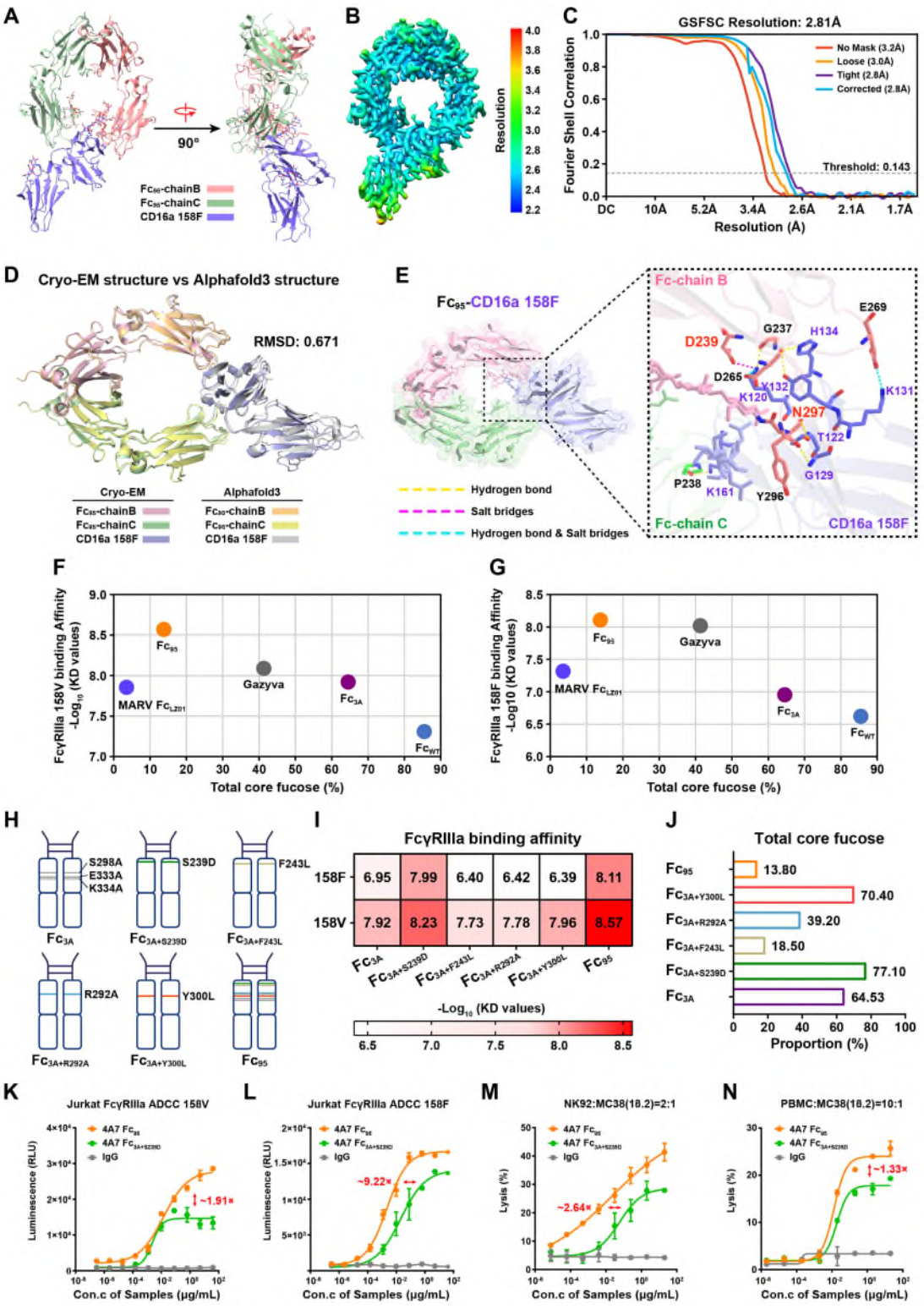

A
90°
Fc95-chainB
Fc95-chainC
CD16a 158F
B
Resolution
C
GSFSC Resolution: 2.81Å
No Mask (3.2Å)
Loose (3.0Å)
Tight (2.8Å)
Corrected (2.8Å)
Threshold: 0.143
Fourier Shell Correlation
Resolution (Å)
D
Cryo-EM structure vs Alphafold3 structure
RMSD: 0.671
Cryo-EM
Alphafold3
E
Fc95-CD16a 158F
Fc-chain B
Fc-chain C
CD16a 158F
Hydrogen bond
Salt bridges
Hydrogen bond & Salt bridges
F
FcγRIIIa 158V binding Affinity -Log10 (KD values)
Total core fucose (%)
MARV FcLZ01
Gazyva
G
FcγRIIIa 158F binding Affinity -Log10 (KD values)
H
S298A
E333A
K334A
S239D
F243L
R292A
Y300L
I
FcγRIIIa binding affinity
158F
158V
-Log10 (KD values)
J
Total core fucose
Proportion (%)
K
Jurkat FcγRIIIa ADCC 158V
Luminescence (RLU)
Con.c of Samples (μg/mL)
~1.91×
L
Jurkat FcγRIIIa ADCC 158F
~9.22×
M
NK92:MC38(18.2)=2:1
Lysis (%)
~2.64×
N
PBMC:MC38(18.2)=10:1
~1.33×
4A7 Fc95
4A7 Fc3A+S239D
IgG

Figure 9. The Fc_{95} Variant Achieves Synergistic CD16a Engagement Through Direct Interface Optimization and Concurrently Enhanced Glycan Microenvironment.

(A) Orthogonal views of the 2.81 Å Cryo-EM structure of the Fc_{95}-CD16a 158F complex. Fc_{95} chain C is shown in green, chain B in red, and CD16a 158F in purple.

(B) The Cryo-EM density map of the complex, colored according to local resolution values (in Å).

(C) Gold-Standard Fourier Shell Correlation (GSFSC) curves for the Cryo-EM reconstruction. The global resolution at the FSC=0.143 criterion is indicated by the horizontal line.

(D) Superposition of the experimental Cryo-EM structure and the AlphaFold3-predicted model. The root-mean-square deviation (RMSD) for the interface atoms is 0.671 Å.

(E) Close-up view of the engineered interface. Key interactions are shown, where hydrogen bonds are indicated by yellow dashed lines, salt bridges by magenta dashed lines, and interactions with both hydrogen bond and salt bridge character by cyan dashed lines.

(F−G) Binding affinity versus core fucose content for a panel of Fc variants. The binding affinity ($-Log_{10}(KD)$) for CD16a allotypes 158V **(F)** and 158F **(G)** is plotted on the y-axis against the total core fucose percentage on the x-axis. Each point represents a different Fc variant as labeled.

(H) Schematic diagram illustrating the mutational path from the Fc_{3A} precursor to the Fc_{95} variant.

(I) Heatmap of binding affinities for Fc variants. KD values for binding to CD16a allotypes 158F and 158V are shown. Color intensity corresponds to the KD value as indicated by the scale bar.

(J) Quantification of core fucose content for Fc variants. The bar chart shows the percentage of total core fucose for each construct as labeled.

(K−L) Jurkat reporter cell assays measuring FcγRIIIa activation by antibody variants in the presence of target cells. Effector cells expressed either the high-affinity 158V (**K**) or low-affinity 158F (**L**) variant of FcγRIIIa.

(M−N) Cytotoxicity assays using NK92 cells (**M**) or primary human PBMCs (**N**) as effectors. Dose–response curves for Fc_{95} are shifted upward and leftward relative to $Fc_{3A+S239D}$, indicating enhanced killing potency.

Data (**F, G, I, J, K−N**) are representative of three independent experiments, are mean ± standard error (**K−N**) of duplicates (**K−N**), and were analyzed by non-linear regression (four-parameter logistic fit) (**K−N**).

Supplementary Materials for

Fc_{95}, a next-generation Fc variant, achieves exceptional ADCC potency by linking affinity enhancement to intrinsic afucosylation.

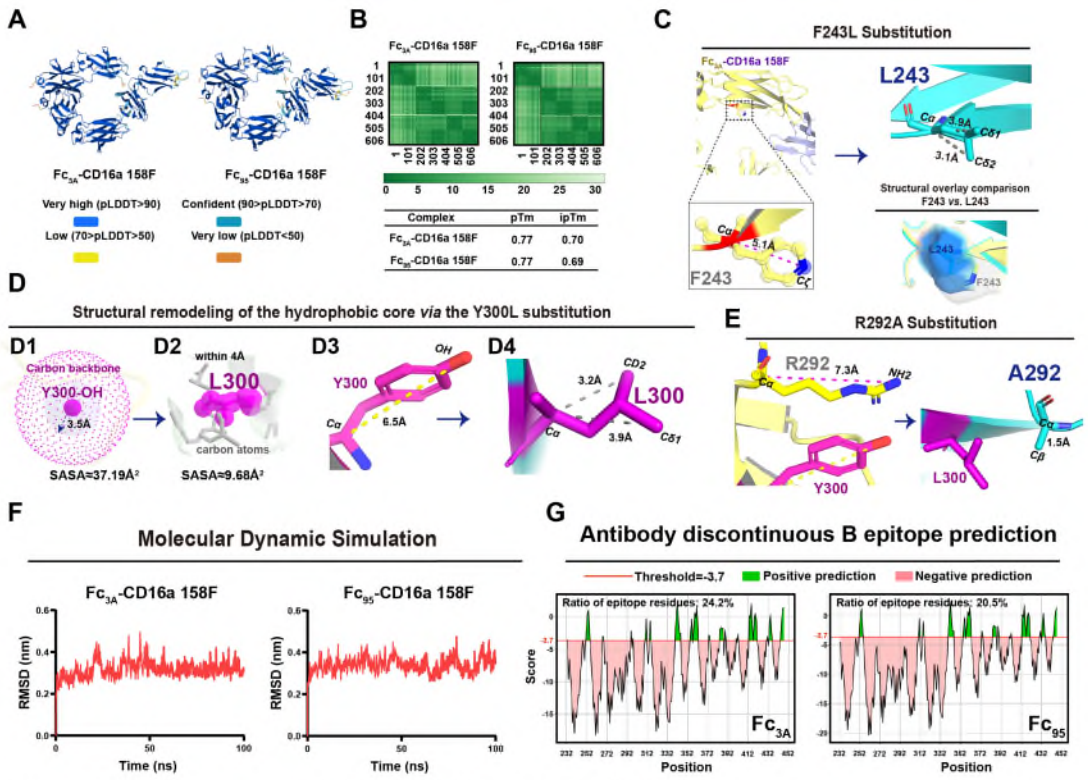
Authors: Yangyihua Zhou, et al.

*Corresponding authors. Email: luolong_long@126.com (L.L.L.);

fengjiannan1970@qq.com (J.N.F); gaoxiang609@163.com (X.G.).

This supplementary file includes:

Supplementary Text
Figs. S1 to S9
Tables S1 to S4



H Antibody MHC I epitope prediction

	Variants	Position	Peptide	Allele	Median binding percentile (%Rank)
	Fc_{WT}		LLGGPSVFL		0.19
1	Fc_{3A}	234-242	LLGGPSVFL	HLA-A*02:01	0.19
	Fc_{95}		LLGGPDVFL		0.25
	Fc_{WT}		ALPAPIEKT		1.1
2	Fc_{3A}	327-335	ALPAPIAAT	HLA-A*02:01	0.92
	Fc_{95}		ALPAPIAAT		0.92
	Fc_{WT}		EQYNSTYRV		1.2
3	Fc_{3A}	294-302	EQYNATYRV	HLA-A*02:01	1.4
	Fc_{95}		EQYNATLRV		1.5
	Fc_{WT}		KALPAPIEK		>2
4	Fc_{3A}	326-334	KALPAPIAA	HLA-A*02:01	1.7
	Fc_{95}		KALPAPIAA		1.7

Strong binder:
< %Rank 0.5
Weak binder:
0.5 ≤ %Rank < 2
Non-binder:
≥ %Rank 2

I Antibody MHC II epitope prediction

	Variants	Position	Peptide	Allele	Median binding percentile (%Rank)
	Fc_{WT}		QYNSTYRVVSVLTVL		3.4
1	Fc_{3A}	295-309	QYNATYRVVSVLTVL	HLA-DRB1*07:01	4.0
	Fc_{95}		QYNATLRVVSVLTVL		>10
	Fc_{WT}		DGVEVHNAKTKPREE		>10
2	Fc_{3A}	280-294	DGVEVHNAKTKPREE	HLA-DRB1*07:01	>10
	Fc_{95}		DGVEVHNAKTKPAEE		8.2

Strong binder:
< %Rank 2
Weak binder:
2 ≤ %Rank < 10
Non-binder:
≥ %Rank 10

Fig. S1. Extended *in silico* characterization and developability assessment of Fc variants.

(A−B) High-confidence structural models from AlphaFold3. **(A)** Per-residue confidence scores (pLDDT) are mapped onto the predicted structures of the Fc_{3A}-CD16a (left) and Fc_{95}-CD16a (right) complexes. Blue indicates very high confidence (pLDDT > 90). **(B)** Predicted Aligned Error (PAE) maps for the same complexes confirm high-accuracy modeling of the inter-domain orientation (dark green indicates low error).

(C) Structural Rationale for the F243L Substitution. (Left) Geometric measurement of the Fc_{3A} F243 side chain. The planar aromatic ring extends 5.1 Å from Cα to Cζ. (Right, Top) The substituted L243 side chain adopts a compact branched conformation, with Cα–Cδ1 and Cα–Cδ2 distances of 3.9 Å and 3.1 Å, respectively. (Right, Bottom) Structural superposition of Fc_{3A} (yellow) and Fc_{95} (marine) at the 243 locus (only Fc regions shown). Semi-transparent gray surface: F243; solid marine surface: L243.

(**D**) Rational optimization of the Y300 microenvironment in the Fc variant. (**D1**) Structural evidence for the unsatisfied polar group at Y300. A 3.5 Å radius probe sphere (light blue, semi-transparent) centered on the Y300 hydroxyl oxygen (magenta) shows no hydrogen bond donors or acceptors (N/O atoms) within reactive distance. (**D2**) Structural validation of the Y300L mutation. Magenta spheres: engineered L300 side chain, packed within a hydrophobic cage formed by 12 proximal carbon atoms (grey sticks) within 4 Å. White semi-transparent surface: solvent-excluded boundary. (**D3**) Y300 side chain extends 6.5 Å from Cα to the terminal hydroxyl group. (**D4**) L300 side chain adopts a compact branched conformation, with Cα–Cδ1 and Cα–Cδ2 distances of 3.9 Å and 3.2 Å, respectively.

(**E**) Geometric and Volumetric Truncation at the 292-locus. (Left) Structural extension of the R292 (*Cα* to terminal *NH2*: 7.3 Å). (Right) Radical side-chain truncation in the Fc_{95} variant (R292A), reducing the extension to 1.5 Å (Cα to Cβ).

(F) Fc_{95}-CD16a complex shows high stability in MD simulations. Root-mean-square deviation (RMSD) of the complex backbone atoms is plotted over a 100-ns trajectory. The Fc_{95} complex (right) achieves a more stable, lower-RMSD equilibrium than the Fc_{3A} complex (left).

(G) Reduced conformational B-cell epitope profile predicted for Fc_{95}. Discontinuous epitope prediction using the ElliPro tool in the IEDB resource calculates the percentage of surface residues likely to be part of an epitope. The lower score for Fc_{95} suggests a potentially reduced

immunogenic risk.

(H−I) T-cell epitope liability assessment reveals no new predicted risks. Predicted binding of neo-epitopes to representative MHC class I (**H**, *HLA-A02*01)* and class II *(***I**, *HLA-DRB1*07*01) alleles was performed using the IEDB Analysis Resource. Tables show peptides spanning the mutation sites with altered binding affinity (percentile rank, %Rank). A lower %Rank indicates stronger binding. The analysis confirms that no new high-affinity binders were introduced in Fc_{95} (MHC-I threshold: %Rank < 2.0; MHC-II threshold: %Rank < 10.0). %Rank refers to the Median binding percentile.

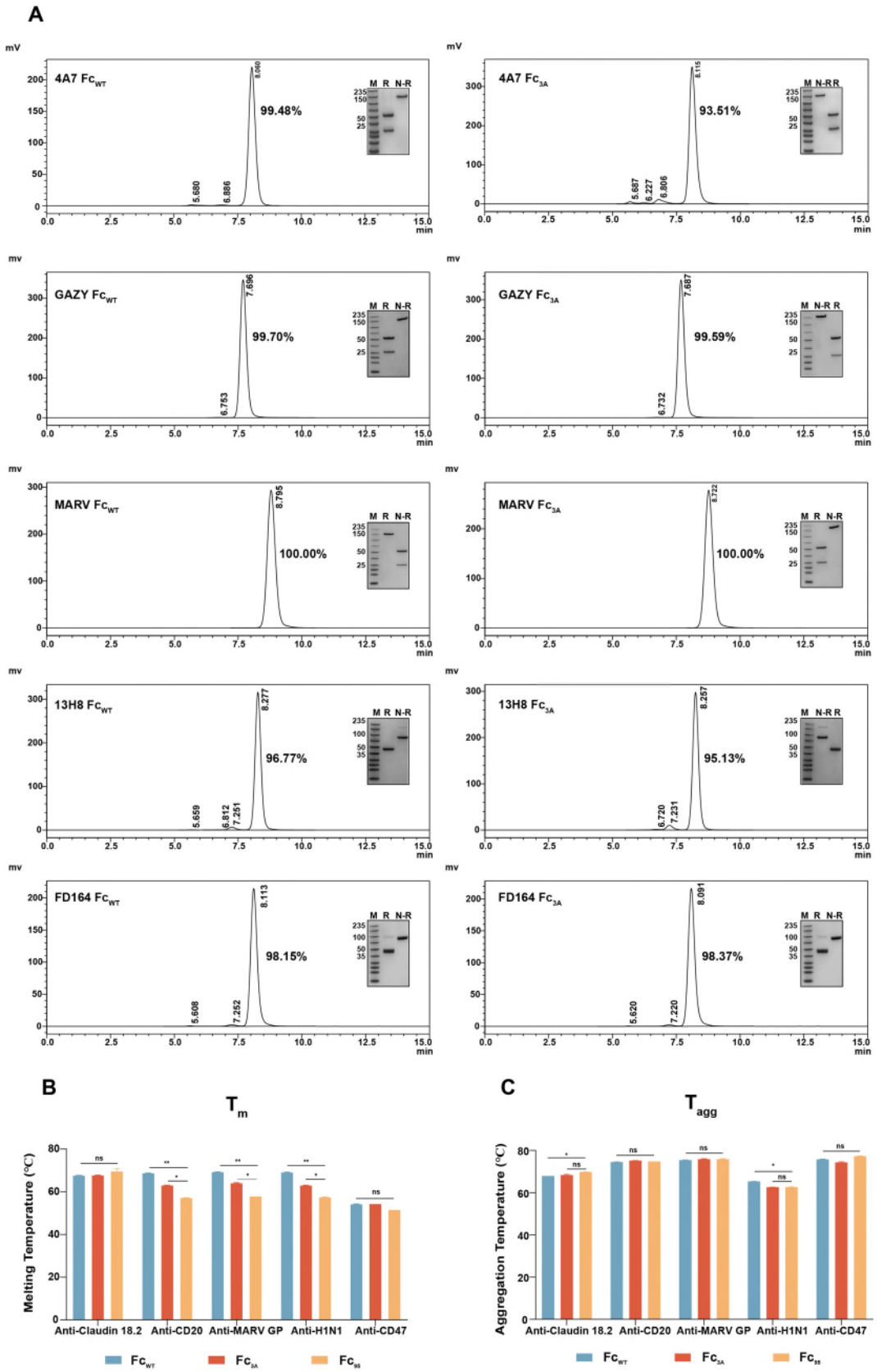
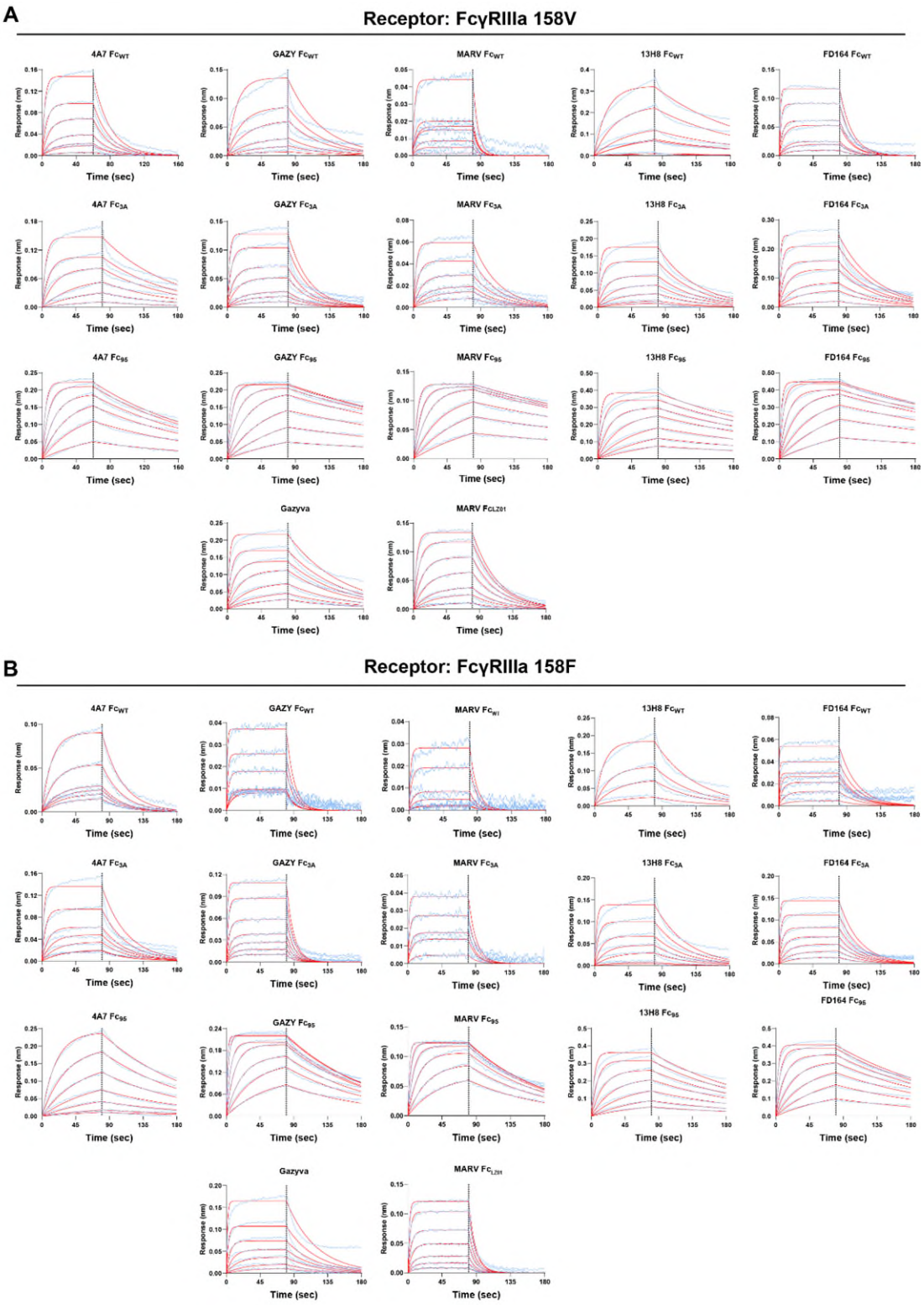

A
4A7 Fc$_{WT}$
99.48%
4A7 Fc$_{3A}$
93.51%
GAZY Fc$_{WT}$
99.70%
GAZY Fc$_{3A}$
99.59%
MARV Fc$_{WT}$
100.00%
MARV Fc$_{3A}$
100.00%
13H8 Fc$_{WT}$
96.77%
13H8 Fc$_{3A}$
95.13%
FD164 Fc$_{WT}$
98.15%
FD164 Fc$_{3A}$
98.37%
M R N-R
M N-R R
mV
mv
min
B
T_m
Melting Temperature (℃)
C
T_{agg}
Aggregation Temperature (℃)
Anti-Claudin 18.2
Anti-CD20
Anti-MARV GP
Anti-H1N1
Anti-CD47
Fc$_{WT}$
Fc$_{3A}$
Fc$_{95}$

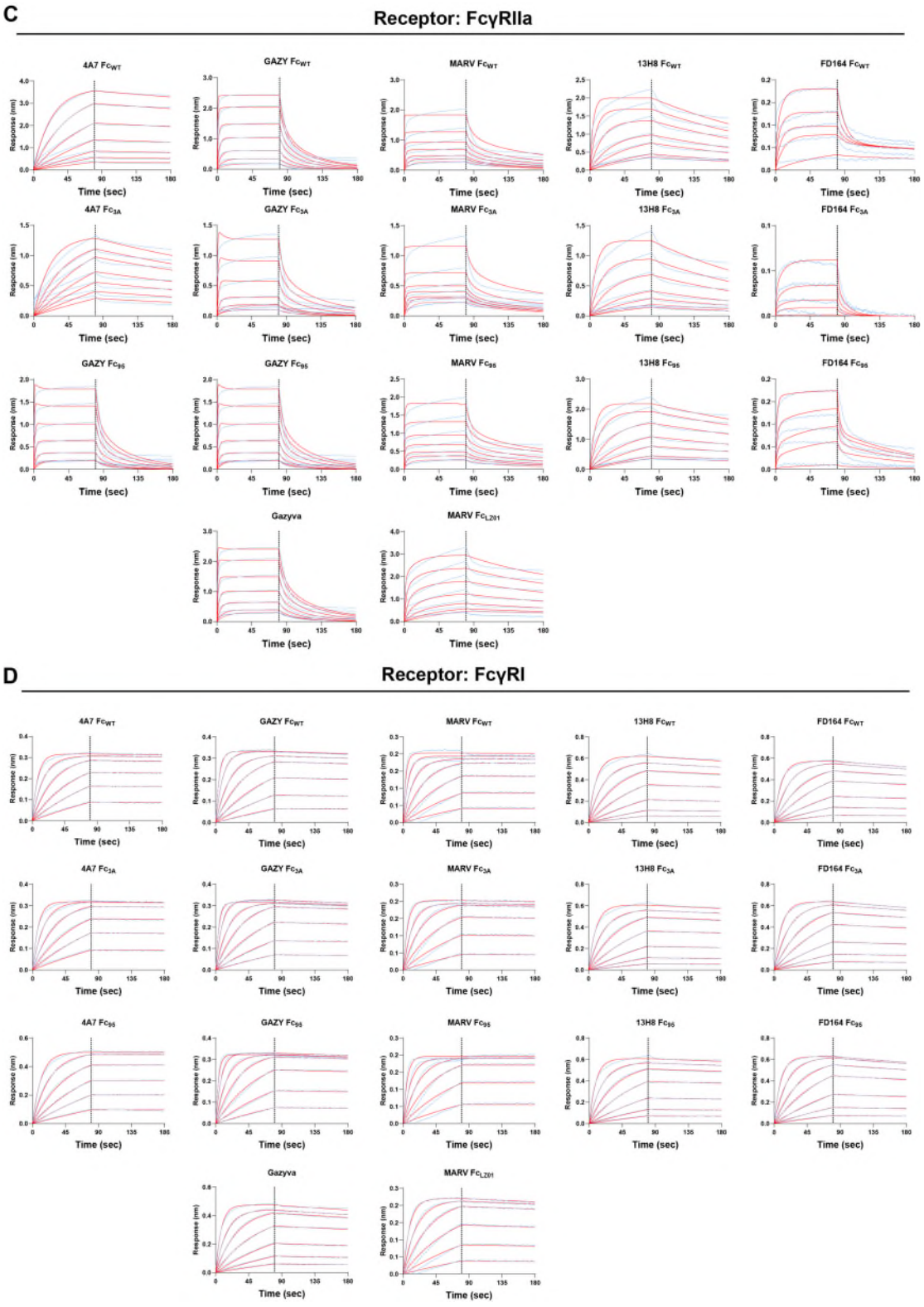
Figure S2. Characterization of all engineered proteins.

(A) Representative SDS-PAGE (non-reducing, N-R; reduced, R) and SEC-HPLC analyses (run at 30°C) for all 15 engineered proteins. The data confirm high purity (>90%) and correct molecular weights for all constructs, as listed in Table S1.

(B−C) Detailed comparison of thermal stability (T_m, **B**) and aggregation onset temperature (T_{agg}, **C**) for five representative antibody backbones expressing the indicated Fc variants (WT, 3A, and 95). The backbones target Claudin 18.2 (4A7), CD20 (GAZY), MARV GP (MARV), H1N1 (13H8), and CD47 (FD164), respectively.

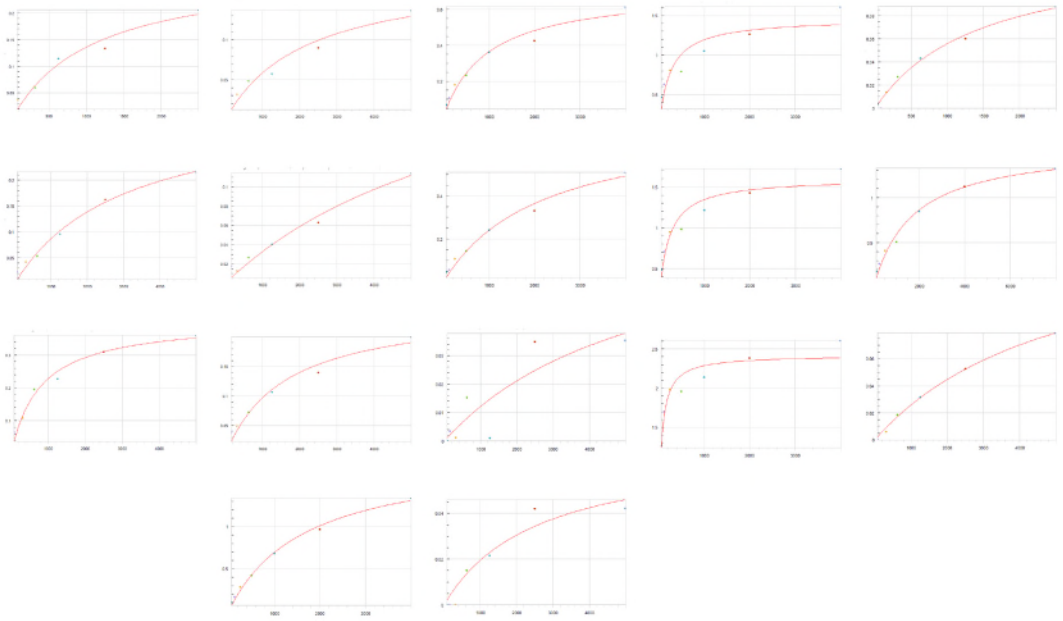
Data in (**B**, **C**) are presented as mean ± SEM from three independent experiments. Statistical significance was determined by two-way ANOVA; ns, not significant, $*P < 0.05$, $**P < 0.01$, $***P < 0.001$.


A
Receptor: FcγRIIIa 158V
4A7 FcWT
GAZY FcWT
MARV FcWT
13H8 FcWT
FD164 FcWT
4A7 Fc3A
GAZY Fc3A
MARV Fc3A
13H8 Fc3A
FD164 Fc3A
4A7 Fc95
GAZY Fc95
MARV Fc95
13H8 Fc95
FD164 Fc95
Gazyva
MARV FcLZ01
B
Receptor: FcγRIIIa 158F
4A7 FcWT
GAZY FcWT
MARV FcWT
13H8 FcWT
FD164 FcWT
4A7 Fc3A
GAZY Fc3A
MARV Fc3A
13H8 Fc3A
FD164 Fc3A
4A7 Fc95
GAZY Fc95
MARV Fc95
13H8 Fc95
FD164 Fc95
Gazyva
MARV FcLZ01
Response (nm)
Time (sec)


C
Receptor: FcγRIIa
4A7 FcWT
GAZY FcWT
MARV FcWT
13H8 FcWT
FD164 FcWT
4A7 Fc3A
GAZY Fc3A
MARV Fc3A
13H8 Fc3A
FD164 Fc3A
GAZY Fc95
GAZY Fc95
MARV Fc95
13H8 Fc95
FD164 Fc95
Gazyva
MARV FcLZ01
Response (nm)
Time (sec)
D
Receptor: FcγRI
4A7 FcWT
GAZY FcWT
MARV FcWT
13H8 FcWT
FD164 FcWT
4A7 Fc3A
GAZY Fc3A
MARV Fc3A
13H8 Fc3A
FD164 Fc3A
4A7 Fc95
GAZY Fc95
MARV Fc95
13H8 Fc95
FD164 Fc95
Gazyva
MARV FcLZ01
Response (nm)
Time (sec)

E

Receptor: FcγRIIb



F

Receptor: FcRn

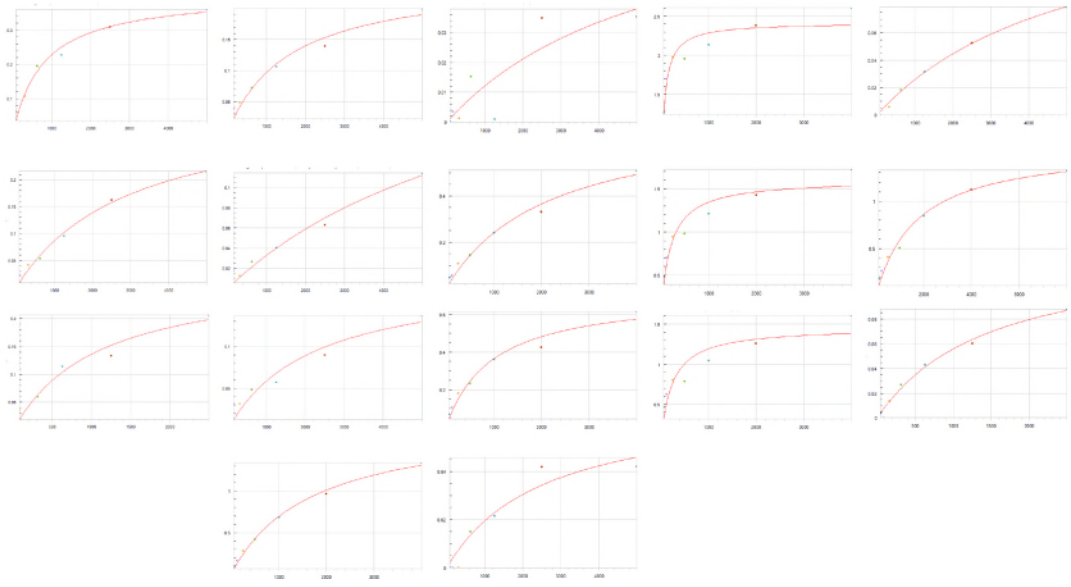


Figure S3. The Fc_{95} Platform Selectively Enhances FcγRIIIa Affinity While Preserving Key Binding Functions.

(A) BLI Sensorgrams for FcγRIIIa (158V) Binding.

(B) BLI Sensorgrams for FcγRIIIa (158F) Binding.

(C) BLI Sensorgrams for FcγRIIa Binding.

(D) BLI Sensorgrams for FcγRI Binding.

(E) Steady-state binding curves for FcγRIIb Binding.

(F) Steady-state binding curves for hFcRn Binding.

Data (**A**−**F**) represent two independent experiments.

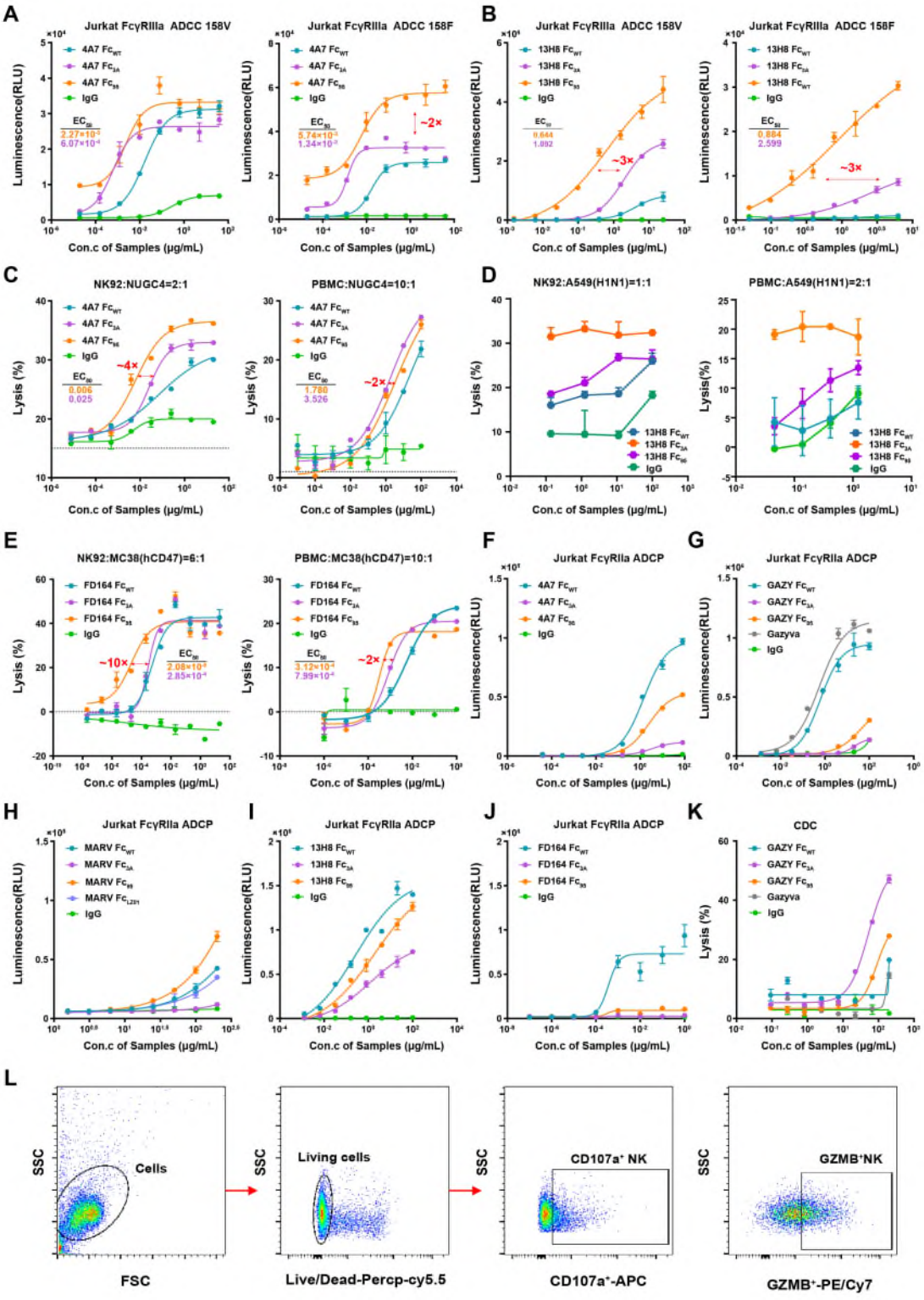

A
Jurkat FcγRIIIa ADCC 158V
Jurkat FcγRIIIa ADCC 158F
Luminescence(RLU)
Con.c of Samples (μg/mL)
4A7 Fc$_{WT}$
4A7 Fc$_{3A}$
4A7 Fc$_{95}$
IgG
~2×
B
Jurkat FcγRIIIa ADCC 158V
Jurkat FcγRIIIa ADCC 158F
13H8 Fc$_{WT}$
13H8 Fc$_{3A}$
13H8 Fc$_{95}$
IgG
~3×
C
NK92:NUGC4=2:1
PBMC:NUGC4=10:1
Lysis (%)
~4×
~2×
D
NK92:A549(H1N1)=1:1
PBMC:A549(H1N1)=2:1
E
NK92:MC38(hCD47)=6:1
PBMC:MC38(hCD47)=10:1
FD164 Fc$_{WT}$
FD164 Fc$_{3A}$
FD164 Fc$_{95}$
~10×
F
Jurkat FcγRIIa ADCP
G
Gazyva
GAZY Fc$_{WT}$
GAZY Fc$_{3A}$
GAZY Fc$_{95}$
H
MARV Fc$_{WT}$
MARV Fc$_{3A}$
MARV Fc$_{95}$
MARV Fc$_{L234}$
I
J
K
CDC
L
SSC
FSC
Cells
Living cells
Live/Dead-Percp-cy5.5
CD107a⁺ NK
CD107a⁺-APC
GZMB⁺NK
GZMB⁺-PE/Cy7

Figure S4. Supplementary Data Supporting the Broad Effector Function of the Fc_{95} Platform.

(A−B) ADCC reporter gene assays using Jurkat cells expressing FcγRIIIa 158V (left) or 158F (right). Activity was assessed for **(A)** anti-Claudin18.2 (4A7) variants and **(B)** anti-H1N1 (13H8) variants.

(C−E) Cell-mediated cytotoxicity assays. **(C)** Lysis of NUGC4 target cells by NK92 cells (left) or PBMCs (right) mediated by anti-Claudin18.2 (4A7) variants. **(D)** Lysis of A549 (H1N1) target cells by NK92 cells (left) or PBMCs (right) mediated by anti-H1N1 (13H8) variants. **(E)** Lysis of MC38 (hCD47) target cells by NK92 cells (left) or PBMCs (right) mediated by anti-CD47 (FD164) variants.

(F-J) Antibody-dependent cellular phagocytosis (ADCP) activity measured using an FcγRIIa reporter assay for **(F)** 4A7 variants, **(G)** GAZY variants, **(H)** MARV variants, **(I)** 13H8 variants and (J) FD164 variants.

(K) Complement-dependent cytotoxicity (CDC) assay showing lysis of Raji cells mediated by anti-CD20 (GAZY) variants. All data are presented as mean ± SEM.

(**L**) Gating strategy for the functional assessment of primary human NK cells by flow cytometry, corresponding to data in **Fig. 4N−O**.

Data (**A–K**) are representative of three independent experiments. Values are presented as mean ± SEM of technical duplicates (**A–E**, **G**, **H**, **J**, **K**) or triplicates (**F**, **I**). Data were analyzed by non-linear regression (four-parameter logistic fit) (**A–C**, **E–K**).

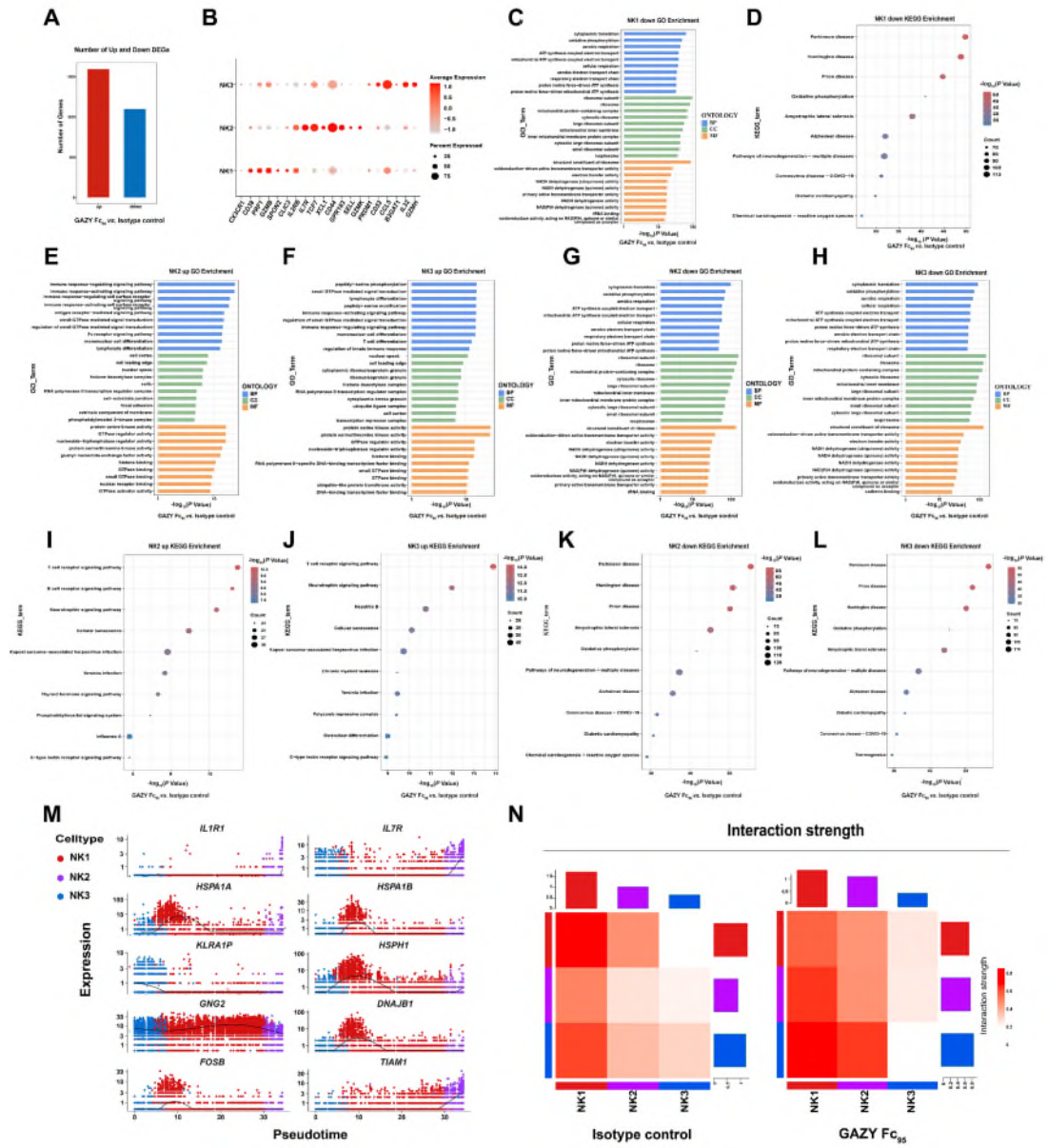

A
B
C
D
E
F
G
H
I
J
K
L
M
N
Number of Up and Down DEGs
Number of Genes
up
down
GAZY Fc95 vs. Isotype control
NK3
NK2
NK1
Average Expression
Percent Expressed
CXCR1 CD8A PECAM1 SPON2 CCL5 IL2RB CLTA TOX KLF2 CD44 SPN SELL CD96 PRDM1 CD53 CCL4 KLRG1 KLF3 GZMA
NK1 down GO Enrichment
GO_Term
ONTOLOGY
BP
CC
MF
-log10(P Value)
NK1 down KEGG Enrichment
KEGG_term
Count
Parkinson disease
Huntington disease
Prion disease
Oxidative phosphorylation
Amyotrophic lateral sclerosis
Alzheimer disease
Pathways of neurodegeneration - multiple diseases
Coronavirus disease - COVID-19
Thermogenesis
Chemical carcinogenesis - reactive oxygen species
NK2 up GO Enrichment
NK3 up GO Enrichment
NK2 down GO Enrichment
NK3 down GO Enrichment
NK2 up KEGG Enrichment
NK3 up KEGG Enrichment
NK2 down KEGG Enrichment
NK3 down KEGG Enrichment
Celltype
NK1
NK2
NK3
Expression
IL1R1
IL7R
HSPA1A
HSPA1B
KLRA1P
HSPH1
GNG2
DNAJB1
FOSB
TIAM1
Pseudotime
Interaction strength
Isotype control
GAZY Fc95

Figure S5. Extended data analysis related to GAZY Fc_{95}-engineered antibody-mediated NK cell reprogramming.

(A) Bar chart showing the number of significantly upregulated and downregulated genes in NK cells after GAZY Fc_{95} stimulation compared with anti-SEB isotype control.

(B) Dot plot showing expression levels and percentages of cells expressing representative marker genes across NK1, NK2, and NK3 subsets.

(C–D) GO **(C)** and KEGG **(D)** enrichment analyses of downregulated genes in NK1 cells.

(E–F) GO enrichment analyses of upregulated **(E)** and downregulated **(F)** genes in NK2 cells.

(G–H) GO enrichment analyses of upregulated **(G)** and downregulated **(H)** genes in NK3 cells.

(I–J) KEGG enrichment analyses of upregulated **(I)** and downregulated **(J)** pathways in NK2 cells.

(K–L) KEGG enrichment analyses of upregulated **(K)** and downregulated **(L)** pathways in NK3 cells.

(M) Expression dynamics of 10 representative genes (*IL1R1, IL7R, HSPA1A, HSPA1B, KLRA1P, HSPH1, GNG2, DNAJB1, FOSB, TIAM1*) plotted along pseudotime, with cells colored by subset identity (NK1, red; NK2, purple; NK3,blue).

(N) Heatmaps showing inter-subset communication strength under control and GAZY Fc_{95} conditions; color intensity represents normalized interaction weight.

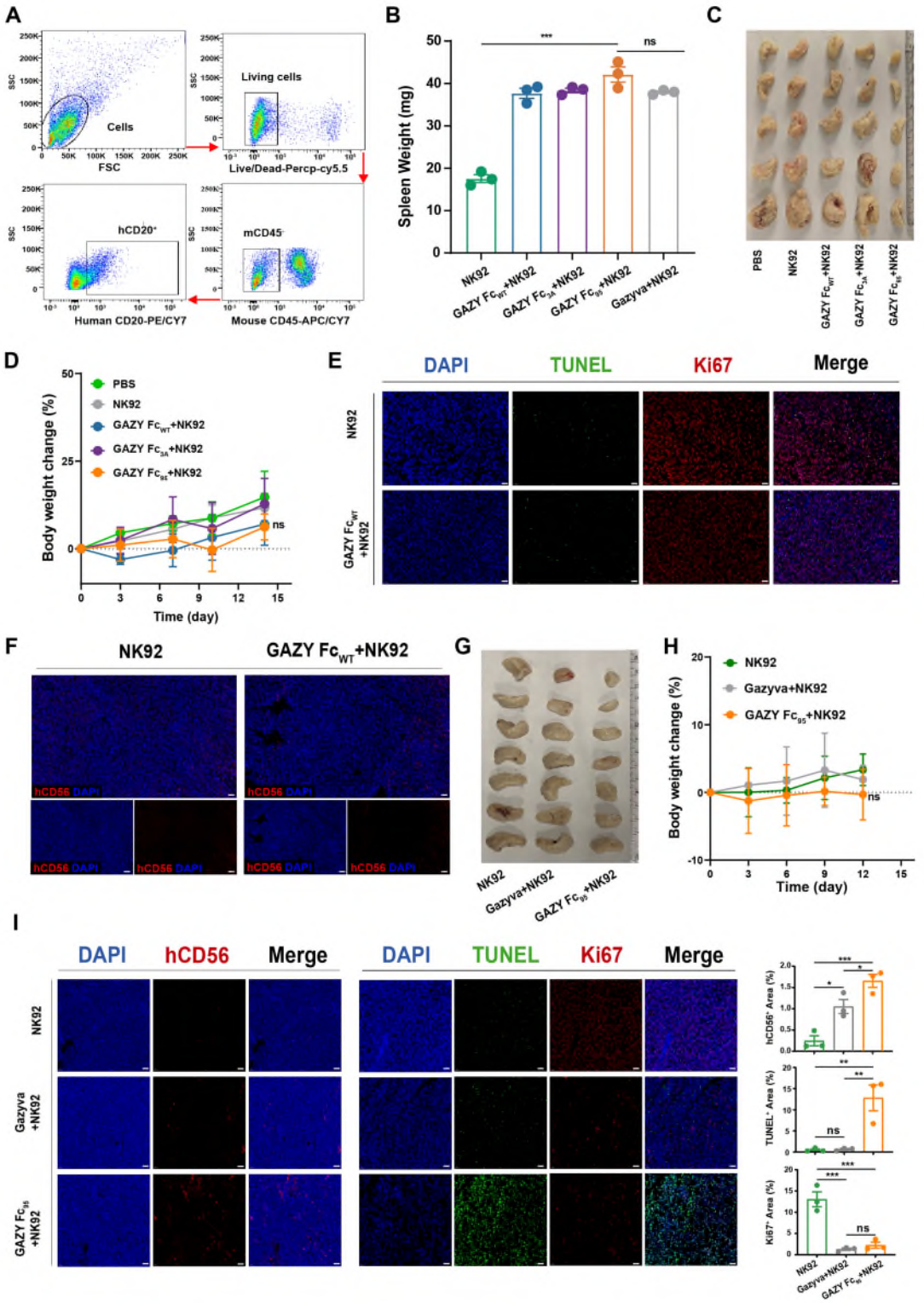

A
Cells
FSC
SSC
Living cells
Live/Dead-Percp-cy5.5
hCD20+
Human CD20-PE/CY7
mCD45-
Mouse CD45-APC/CY7
B
Spleen Weight (mg)
***
ns
NK92
GAZY Fc$_{WT}$+NK92
GAZY Fc$_{3A}$+NK92
GAZY Fc$_{95}$+NK92
Gazyva+NK92
C
PBS
NK92
GAZY Fc$_{WT}$+NK92
GAZY Fc$_{3A}$+NK92
GAZY Fc$_{95}$+NK92
D
Body weight change (%)
PBS
NK92
GAZY Fc$_{WT}$+NK92
GAZY Fc$_{3A}$+NK92
GAZY Fc$_{95}$+NK92
ns
Time (day)
E
DAPI
TUNEL
Ki67
Merge
NK92
GAZY Fc$_{WT}$+NK92
F
NK92
GAZY Fc$_{WT}$+NK92
hCD56 DAPI
G
NK92
Gazyva+NK92
GAZY Fc$_{95}$+NK92
H
NK92
Gazyva+NK92
GAZY Fc$_{95}$+NK92
Body weight change (%)
ns
Time (day)
I
DAPI
hCD56
Merge
DAPI
TUNEL
Ki67
Merge
NK92
Gazyva +NK92
GAZY Fc$_{95}$ +NK92
hCD56$^+$ Area (%)
TUNEL$^+$ Area (%)
Ki67$^+$ Area (%)
ns
NK92
Gazyva+NK92
GAZY Fc$_{95}$+NK92

Figure S6. Supplementary Data Supporting the *In Vivo* Mechanism of GAZY Fc_{95} with Co-administered NK Cells.

(A) Gating strategy for quantifying circulating $hCD20^+$ Raji cells by flow cytometry, corresponding to data in Fig. 6C.

(B) spleen weights 30 days post treatment from the disseminated lymphoma model. The increased spleen mass in all antibody-NK92 combination groups, relative to controls, reflects robust, antibody-mediated immune engagement, n = 3.

(C) Representative images of excised tumors from the subcutaneous model, visually corresponding to endpoint tumor weights in Fig. 6G.

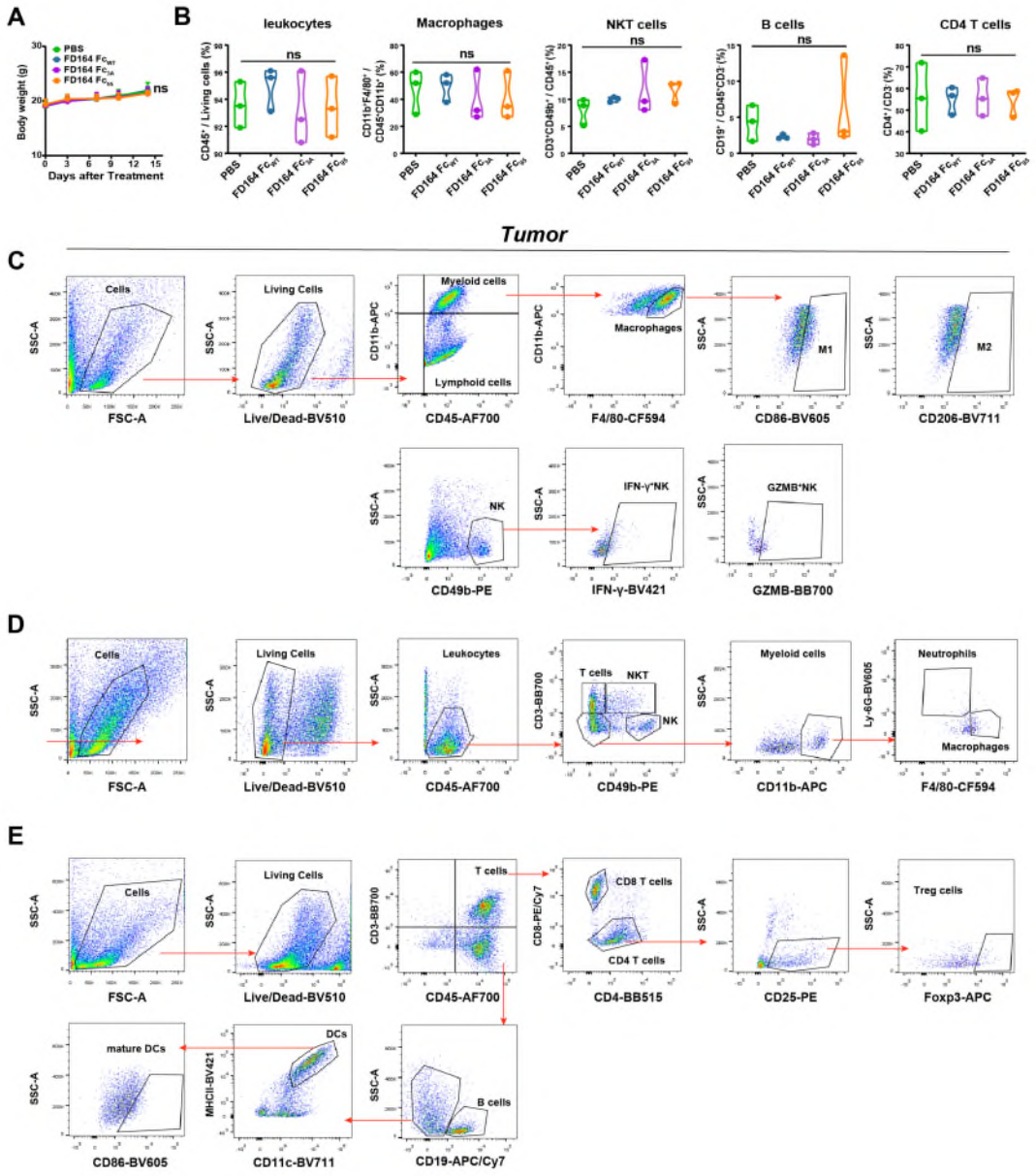
(D) Treatment with GAZY Fc_{95} and NK92 cells is well-tolerated. Body weights of mice during the subcutaneous tumor study show no signs of toxicity, n = 5/group.

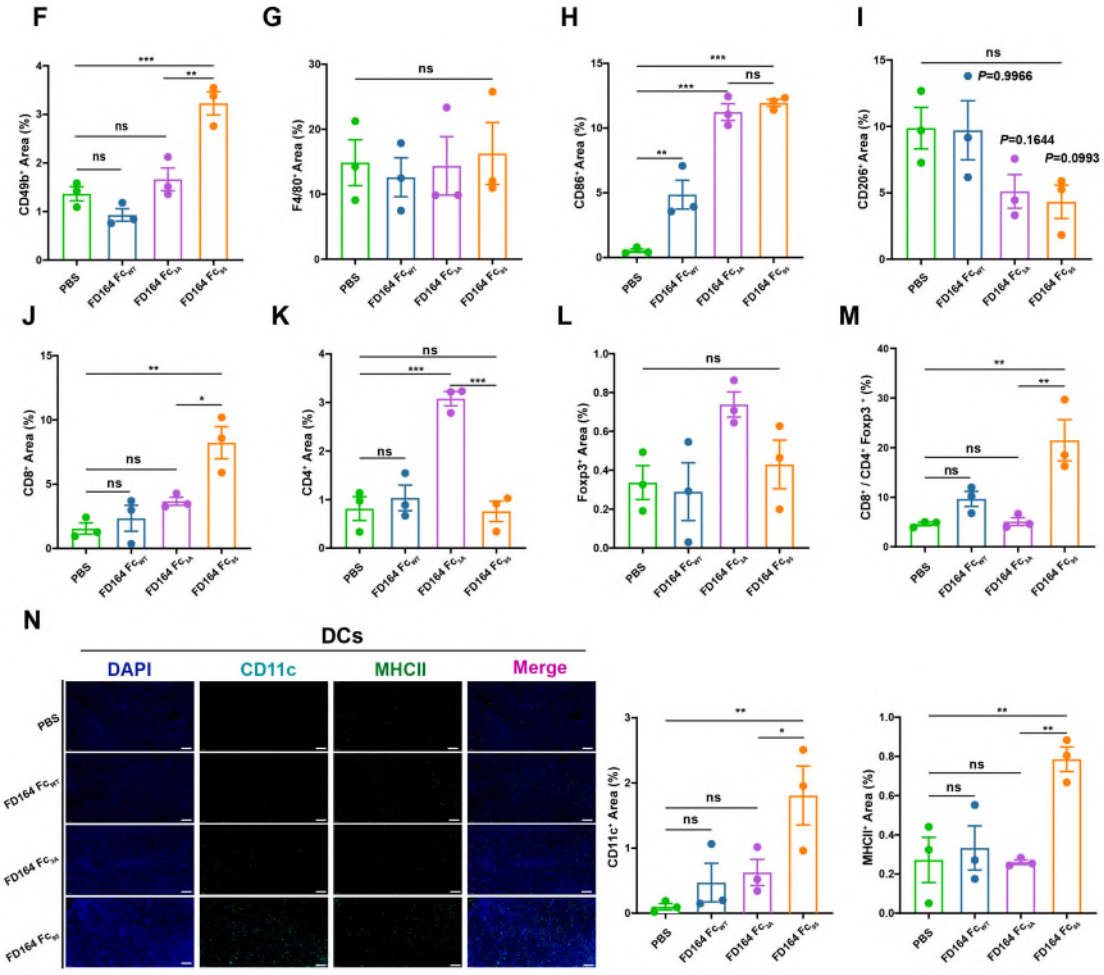
(E−F) Immunofluorescence analysis of control groups highlights the unique activity of GAZY Fc_{95}. **(E)** Representative images showing limited apoptosis (TUNEL) and high proliferation (Ki67) in tumors from NK92-only and GAZY Fc_{WT}+NK92 groups. **(F)** Corresponding images showing sparse $hCD56^+$ NK cell infiltration in control groups, providing a baseline for the massive influx seen in Fig. 6I. Scale bars, 50 μm (**E**) and 100 μm (**F**).

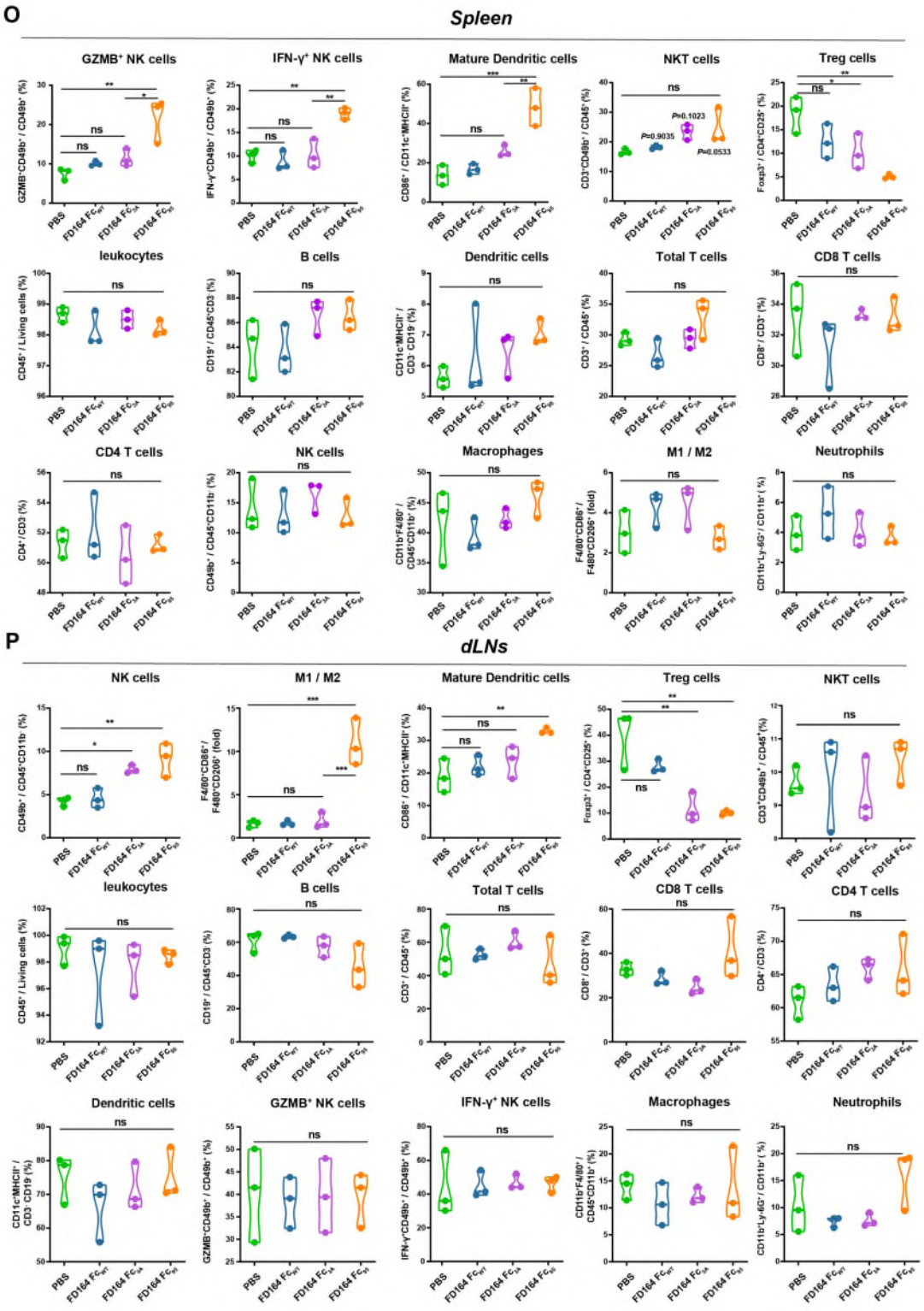
(G) Representative images of excised tumors corresponding to Fig. 6Q demonstrating the dominant monotherapy efficacy of GAZY Fc_{95}, n=7/group.

(H) Treatment with GAZY Fc_{95} and NK92 cells is well-tolerated. Body weights of mice during the subcutaneous tumor study in **Fig. 6O−Q** show no signs of toxicity, n = 7/group.

(I) Representative immunofluorescence images and corresponding quantification from tumor sections related to **Fig. 6O−Q**. Left panels show tumor-infiltrating human NK cells (hCD56, red). Right panels show apoptosis (TUNEL, green) and proliferation (Ki67, red). Scale bars, 100 μm (left panels) and 50 μm (right panels). Data (**A−I**) are representative of two or three independent experiments. Statistical analysis was performed using ordinary one-way ANOVA with multiple comparisons test (**B**, **I**) or two-way ANOVA test (**D**, **H**), ns, not significant, $*P < 0.05$, $**P < 0.01$, $***P < 0.001$, $****P < 0.0001$.


A
B
leukocytes
Macrophages
NKT cells
B cells
CD4 T cells
ns
PBS
FD164 Fc$_{wt}$
FD164 Fc$_{LA}$
FD164 Fc$_{SA}$
Body weight (g)
Days after Treatment
CD45$^+$ / Living cells (%)
CD11b$^+$F4/80$^+$ / CD45$^+$CD11b$^+$ (%)
CD3$^+$CD49b$^+$ / CD45$^+$ (%)
CD19$^+$ / CD45$^+$CD3$^-$ (%)
CD4$^+$/ CD3$^+$ (%)
Tumor
C
Cells
Living Cells
Myeloid cells
Lymphoid cells
Macrophages
M1
M2
NK
IFN-γ$^+$NK
GZMB$^+$NK
SSC-A
FSC-A
Live/Dead-BV510
CD11b-APC
CD45-AF700
F4/80-CF594
CD86-BV605
CD206-BV711
CD49b-PE
IFN-γ-BV421
GZMB-BB700
D
Leukocytes
T cells
NKT
NK
Neutrophils
Ly-6G-BV605
CD3-BB700
E
CD8 T cells
CD4 T cells
Treg cells
mature DCs
DCs
B cells
CD8-PE/Cy7
CD4-BB515
CD25-PE
Foxp3-APC
MHCII-BV421
CD11c-BV711
CD19-APC/Cy7


F
G
H
I
J
K
L
M
N
DCs
DAPI
CD11c
MHCII
Merge
PBS
FD164 FcWT
FD164 FcYA
FD164 FcYS
CD49b+ Area (%)
F4/80+ Area (%)
CD86+ Area (%)
CD206+ Area (%)
CD8+ Area (%)
CD4+ Area (%)
Foxp3+ Area (%)
CD8+ / CD4+ Foxp3 + (%)
CD11c+ Area (%)
MHCII+ Area (%)
ns
P=0.9966
P=0.1644
P=0.0993


O
Spleen
GZMB+ NK cells
IFN-γ+ NK cells
Mature Dendritic cells
NKT cells
Treg cells
leukocytes
B cells
Dendritic cells
Total T cells
CD8 T cells
CD4 T cells
NK cells
Macrophages
M1 / M2
Neutrophils
P
dLNs
NK cells
M1 / M2
Mature Dendritic cells
Treg cells
NKT cells
leukocytes
B cells
Total T cells
CD8 T cells
CD4 T cells
Dendritic cells
GZMB+ NK cells
IFN-γ+ NK cells
Macrophages
Neutrophils
PBS
FD164 Fcwt
FD164 FcLA
FD164 FcLS
ns

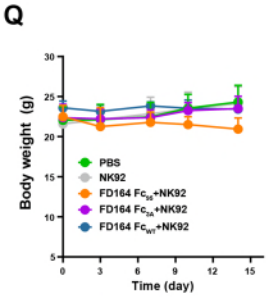


Figure S7. Comprehensive immunophenotyping reveals the systemic and intratumoral impact of FD164 Fc$_{95}$, confirming its excellent safety profile, related to Figure 7.

(A) Body weight changes in hCD16a transgenic mice during the treatment regimen, confirming the excellent tolerability of all tested therapeutics.

(B) Flow cytometry analysis showing no significant inter-group differences in the overall tumor infiltration of total lymphocytes (CD45$^+$), total macrophages, NKT cells, B cells, or CD4$^+$ T cells.

(C−E) Representative gating strategies for flow cytometry analysis of **(C)** NK cells and macrophages, **(D)** NKT cells and neutrophils and **(E)** T cells, B cells, and dendritic cells (DCs) within the Tumor Microenvironment (TME).

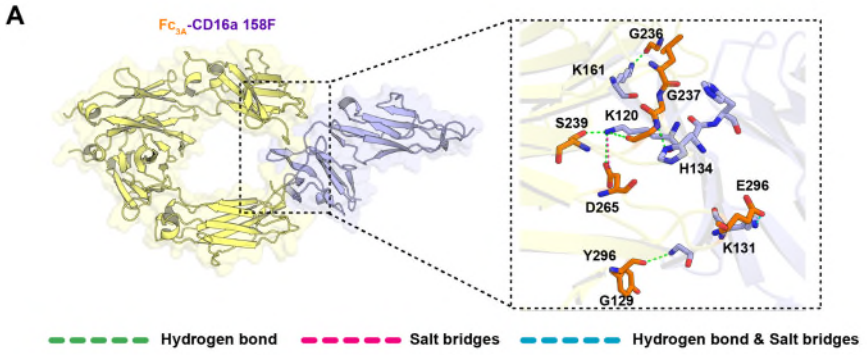
(F−M) Quantification of immunofluorescence staining for immune cell populations within the TME. Quantification of: **(F)** CD49b$^+$ NK cells, **(G)** total macrophages, **(H)** CD86$^+$ M1-like macrophages, **(I)** CD206$^+$ M2-like macrophages, **(J)** CD8$^+$ T cells, **(K)** CD4$^+$ T cells, and **(L)** Foxp3$^+$ Tregs. **(M)** The calculated ratio of CD8$^+$ T cells to Tregs. n = 3 biological replicates.

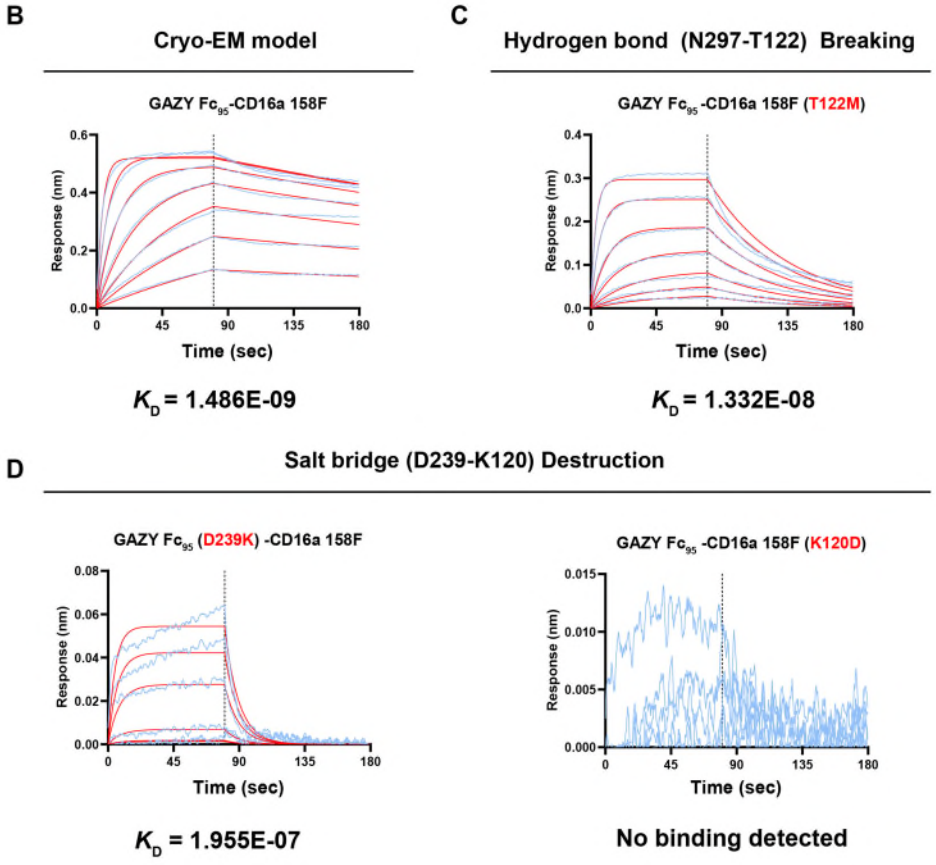
(N) Representative immunofluorescence images (left) and quantification (right) of tumor sections showing CD11c$^+$ and MHCII$^+$ dendritic cells.

(O−P) Systemic immune profiling of secondary lymphoid organs. Analysis of key immune cell populations in **(O)** the spleen and **(P)** tumor-draining lymph nodes (dLNs), demonstrating systemic immune activation and Treg depletion by FD164 Fc$_{95}$. Representative dot plots are shown for experimental groups with significant immune cell remodeling in **Extended data Fig. 3 and Extended data Fig. 4**. The gating strategies for immune subsets in the spleen and dLNs are consistent with those described for the TME (**Fig. S7C−E**).

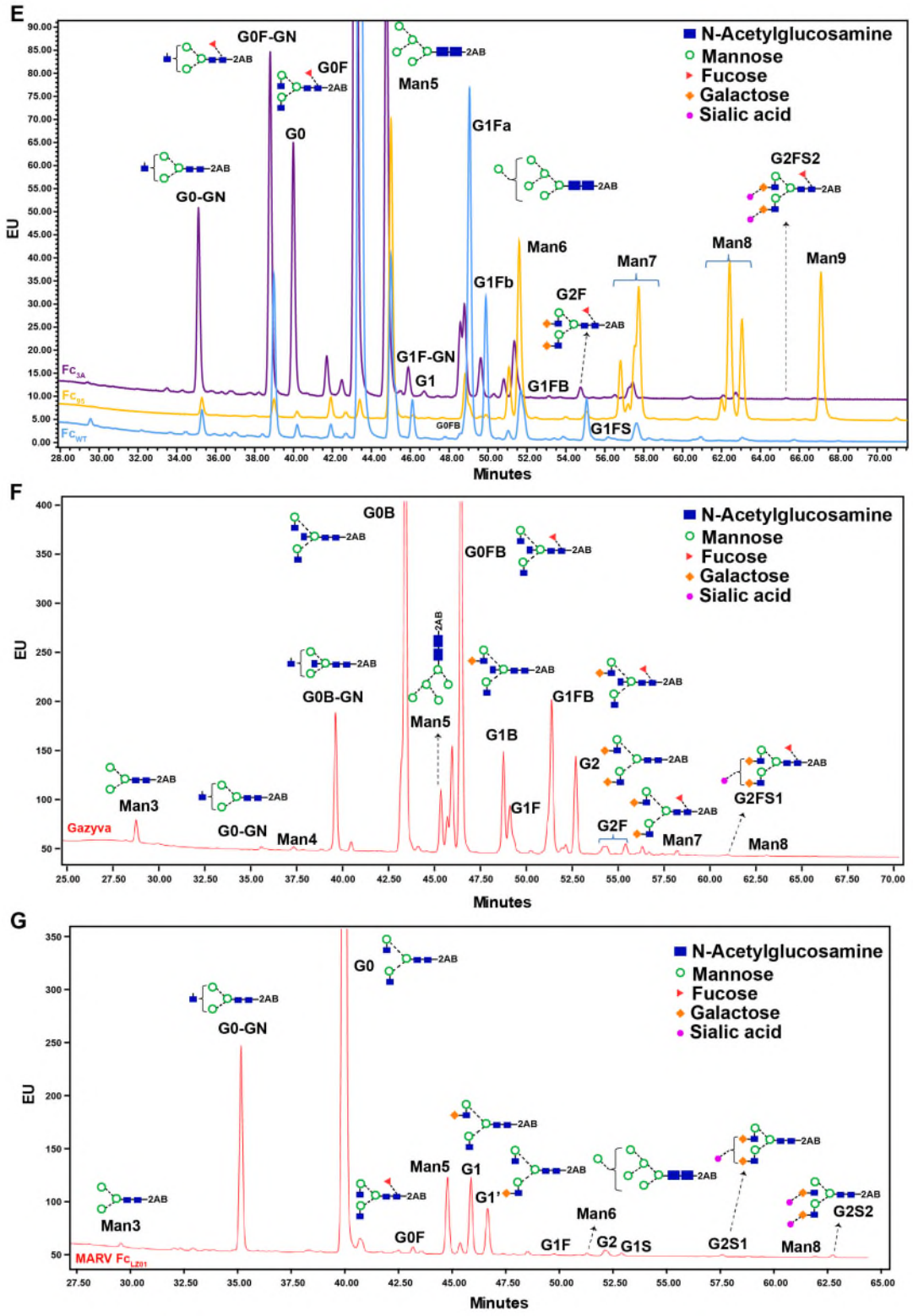
(Q) Body weight changes in immunodeficient mice bearing Raji tumors and co-injected with human NK92 cells, confirming the safety of the treatment in this isolated therapeutic setting.

Data (**A, B, F−Q**) are representative of two independent experiments and are mean ± standard error (**A, B, F−P**) of triplicates (**F−N**). Each dot represents one mouse (**A, B, O−Q**). Statistical analysis was performed using two-way ANOVA with Tukey's multiple comparisons test (**A, Q**) or ordinary one-way ANOVA with multiple comparisons test (**B, L, F**), ns, not significant, $*P < 0.05$, $**P < 0.01$, $***P < 0.001$.


A
Fc3A-CD16a 158F
G236
K161
G237
S239
K120
H134
E296
D265
K131
Y296
G129
Hydrogen bond
Salt bridges
Hydrogen bond & Salt bridges


B
Cryo-EM model
GAZY Fc95-CD16a 158F
Response (nm)
Time (sec)
KD = 1.486E-09
C
Hydrogen bond (N297-T122) Breaking
GAZY Fc95-CD16a 158F (T122M)
Response (nm)
Time (sec)
KD = 1.332E-08
D
Salt bridge (D239-K120) Destruction
GAZY Fc95 (D239K) -CD16a 158F
Response (nm)
Time (sec)
KD = 1.955E-07
GAZY Fc95-CD16a 158F (K120D)
Response (nm)
Time (sec)
No binding detected

1805


E
N-Acetylglucosamine
Mannose
Fucose
Galactose
Sialic acid
G0F-GN
G0F
G0
G0-GN
Man5
G1Fa
G2FS2
Man6
Man7
Man8
Man9
G1Fb
G2F
G1F-GN
G1
G1FB
G0FB
G1FS
EU
Minutes
F
G0B
G0FB
G0B-GN
Man5
G1FB
G1B
G2
G2FS1
Man3
G0-GN
Man4
G1F
G2F
Man7
Man8
Gazyva
Minutes
G
G0
G0-GN
Man3
Man5
G1
G1'
G0F
Man6
G1F
G2
G1S
G2S1
Man8
G2S2
MARV Fc
Minutes

1806
1807

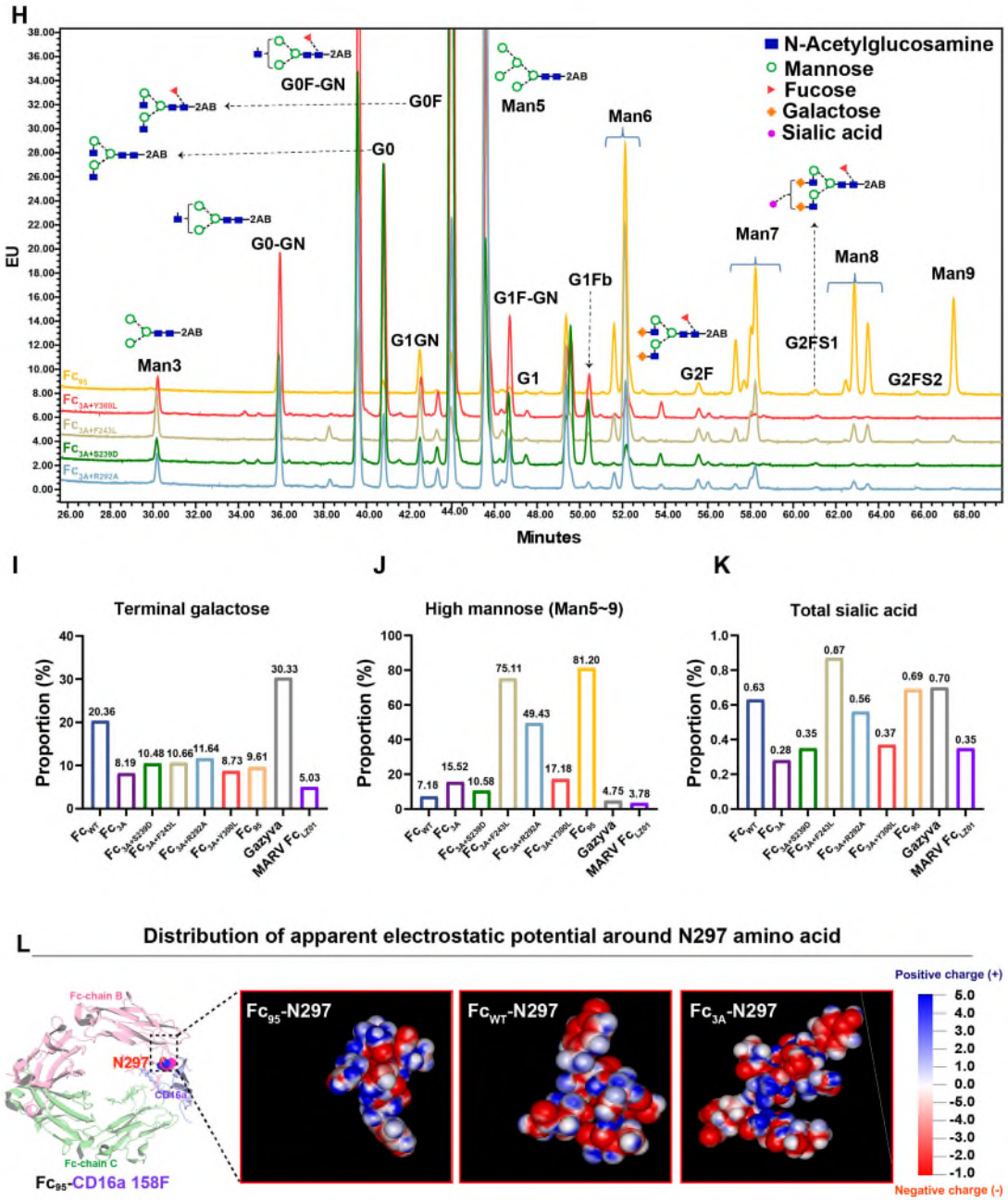

H
N-Acetylglucosamine
Mannose
Fucose
Galactose
Sialic acid
EU
Minutes
G0F-GN
G0F
G0
Man5
Man6
G0-GN
G1GN
G1F-GN
G1Fb
Man7
Man8
Man9
Man3
G1
G2F
G2FS1
G2FS2
I
Terminal galactose
Proportion (%)
20.36
8.19
10.48
10.66
11.64
8.73
9.61
30.33
5.03
J
High mannose (Man5~9)
7.18
15.52
10.58
75.11
49.43
17.18
81.20
4.75
3.78
K
Total sialic acid
0.63
0.28
0.35
0.87
0.56
0.37
0.69
0.70
0.35
Gazyva
MARV FC_L2H1
L
Distribution of apparent electrostatic potential around N297 amino acid
Fc-chain B
Fc-chain C
N297
CD16a
Fc95-CD16a 158F
Fc95-N297
FcWT-N297
Fc3A-N297
Positive charge (+)
Negative charge (-)

Figure S8. Supporting Data for the Design, Validation, and Mechanistic Analysis of Fc_{95}.

(A) Computationally predicted model of the Fc_{3A}-CD16a complex using AlphaFold3. Fc_{3A} is colored yellow and CD16a is colored light blue. The inset shows a close-up view of the interface, with predicted hydrogen bonds and salt bridges indicated by green and magenta dashed lines, respectively.

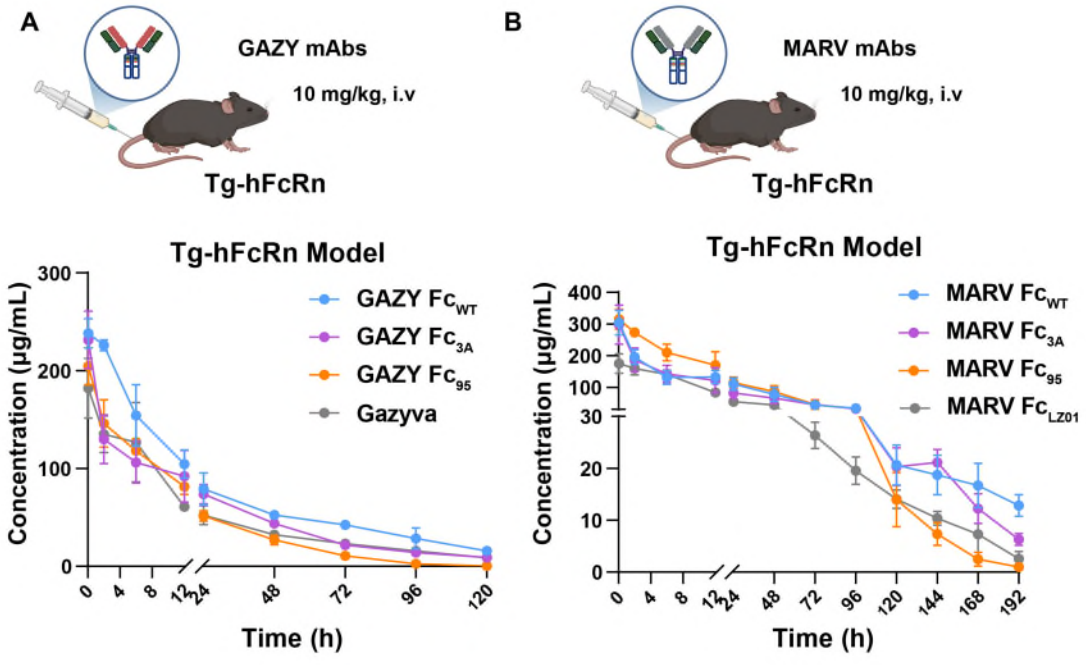
(**B**–**D**) BLI sensorgrams validating key interactions in the Fc_{95}-CD16a 158F interface. (**B**) Representative BLI sensorgrams of Fc_{95} binding to Fc_{95}–CD16a 158F (K_D = 1.49E-09 M); (**C**) T122M mutation on Fc_{95}–CD16a 158F disrupts the N297-T122 hydrogen bond, reducing affinity ~10-fold (1.33E-08 M); (**D**) D239K mutation on Fc_{95} disrupts the S239D-K120 salt bridge, reducing affinity ~100-fold (2.00E-07 M) (left), reciprocal K120D mutation on CD16a nearly abolishes detectable binding (right).

(**E**–**H**) Representative HILIC-UPLC chromatograms of N-glycans released from the indicated Fc variants: (**E**) WT, 3A, and 95 scaffolds; (**F**) Gazyva; (**G**) MARV Fc_{LZ01}; (**H**) $Fc_{3A+S239D}$, $Fc_{3A+F243L}$, $Fc_{3A+R292A}$, $Fc_{3A+Y300L}$, Fc_{95}. Peaks corresponding to major glycan species are labeled.

(**I**–**K**) Quantitative analysis of specific glycan features for a panel of Fc variants, including WT, 3A, 95, Gazyva, MARV Fc_{LZ01}, and four additional mutants (S239D, F243L, R292A, Y300L). (**I**) Terminal galactosylation levels (percentage of total glycans). (**J**) High-mannose type glycans. (**K**) Sialic acid content.

(L) Distribution of surface electrostatic potential within 5 Å of the N297 amino acid. (Left): Structural overview of the Fc_{95}-CD16a 158F complex. (Right) Zoomed-in views (5 Å radius) of the N297 microenvironment for Fc_{95}, Fc_{WT}, and Fc_{3A}. Surfaces are colored by potential according to the scale bar (blue: positive; red: negative; white: neutral).

Data are representative of three independent experiments (**B**–**D, I**–**K**).



Parameters	GAZY Fc$_{WT}$	GAZY Fc$_{3A}$	GAZY Fc$_{95}$	Gazyva
Half-life ($T_{1/2}$), h	47.13	47.47^{ns}	36.95*	45.85^{ns}
Cmax, μg/mL	304.07	298.01^{ns}	314.96^{ns}	180.67**
AUC (0~∞), μg×h/mL	10269.06	9924.15^{ns}	8907.27^{ns}	6022.15**

Parameters	MARV Fc$_{WT}$	MARV Fc$_{3A}$	MARV Fc$_{95}$	MARV Fc$_{LZ01}$
Half-life ($T_{1/2}$), h	47.67	42.83^{ns}	36.53*	40.89*
Cmax, μg/mL	238.94	231.39^{ns}	204.71^{ns}	182.12**
AUC (0~∞), μg×h/mL	7189.14	5317.10^{ns}	4511.70*	3856.99**

Figure S9. Pharmacokinetic profiles of Fc$_{95}$ variants in Tg-hFcRn mice.

(**A**–**B**) Serum concentration-time curves of (**A**) GAZY-based and (**B**) MARV-based Fc variants following a single intravenous dose (10 mg/kg) in Tg-hFcRn transgenic mice.

Data (**A, B**) are representative of two independent experiments, are mean ± standard error (n=4 mice per group), and were analyzed by one-way ANOVA with multiple comparisons test, ns, not significant, *P < 0.05, **P < 0.01, ***P < 0.001.

Table S1. Expression yields and purification summary for all 15 antibodies

Samples	Targets	Total expression amount (mg/L)	Concentration (mg/mL)
4A7 Fc_{WT}	Claudin 18.2	118.6	3.56
4A7 Fc_{3A}		240.0	11.24
4A7 Fc_{95}		962.2	7.76
GAZY Fc_{WT}	CD20	396.3	3.17
GAZY Fc_{3A}		368.0	3.20
GAZY Fc_{95}		334.7	2.91
MARV Fc_{WT}	Marburg G Protein	438.8	3.10
MARV Fc_{3A}		363.0	3.51
MARV Fc_{95}		353.4	3.30
13H8 Fc_{WT}	Influenza hemagglutinin stem (H1N1)	438.6	2.46
13H8 Fc_{3A}		527.6	3.38
13H8 Fc_{95}		475.9	2.95
FD164 Fc_{WT}	CD47	624.1	4.09
FD164 Fc_{3A}		742.3	4.03
FD164 Fc_{95}		679.0	4.56

Table S2

KD for FcγR of Fc variants						
Fc variants	K_D for FcγRIIIa^{158V} (mol/L)	K_D for FcγRIIIa^{158F} (mol/L)	K_D for FcγRIIa (mol/L)	K_D for FcγRIIb (mol/L)	K_D for FcγRI (mol/L)	K_D for hFcRn (mol/L)
4A7 Fc_{WT}	7.890E-08	1.763E-07	1.926E-09	3.907E-06	4.398E-11	2.3E-08
4A7 Fc_{3A}	1.202E-08	1.122E-07	5.558E-09	2.719E-06	3.960E-11	2.3E-08
4A7 Fc_{95}	2.692E-09	7.762E-09	3.991E-09	3.676E-06	1.000E-12	2.5E-08
GAZY Fc_{WT}	6.164E-08	1.441E-07	7.065E-07	2.200E-06	1.444E-10	2.3E-08
GAZY Fc_{3A}	1.172E-08	3.852E-08	1.087E-06	2.493E-06	1.498E-10	1.5E-08
GAZY Fc_{95}	1.254E-09	2.723E-09	5.636E-07	1.314E-06	8.569E-11	1.4E-08
MARV Fc_{WT}	7.915E-08	6.122E-08	1.956E-07	9.681E-07	3.771E-11	2.0E-08
MARV Fc_{3A}	6.737E-09	1.632E-08	1.745E-07	1.286E-06	5.204E-11	1.6E-08
MARV Fc_{95}	7.572E-10	2.009E-09	8.651E-08	5.674E-06	9.080E-12	2.2E-08
13H8 Fc_{WT}	6.547E-07	1.145E-06	2.828E-07	6.285E-07	7.622E-10	6.6E-08
13H8 Fc_{3A}	1.347E-08	1.359E-08	7.041E-07	3.985E-07	5.512E-10	1.4E-07
13H8 Fc_{95}	3.700E-09	6.009E-09	3.928E-07	1.526E-07	3.718E-10	2.3E-07
FD164 Fc_{WT}	1.838E-08	1.525E-08	9.992E-07	1.581E-06	1.056E-09	1.4E-06
FD164 Fc_{3A}	1.064E-08	1.024E-08	5.524E-05	1.336E-06	1.004E-09	2.9E-06
FD164 Fc_{95}	2.256E-09	4.052E-09	1.279E-06	5.377E-06	9.153E-10	3.0E-06
Gazyva	8.146E-09	7.536E-09	4.668E-07	9.606E-07	5.771E-10	1.5E-07
MARV Fc_{LZ01}	1.395E-08	4.817E-08	8.017E-08	2.688E-06	2.039E-10	1.5E-08

Table S3. Quantitative histopathological scores of organ lesions.

Tissues (liver, spleen, kidney) were collected from mice at the study endpoint (as described in Figure 8D), fixed in 10% neutral buffered formalin, and embedded in paraffin. Sections were stained with Hematoxylin and Eosin (H&E) for histopathological evaluation. A board-certified pathologist, who was blinded to the experimental groups, performed the scoring.

Scoring Criteria:

Score	**Grade**	**Pathological Description**	**Tissue Area Affected**
0	Normal	No observable pathological changes.	N/A
1	Minimal (+)	Focal and minimal inflammatory cell infiltration.	<5%
2	Mild (++)	Multifocal inflammation and occasional necrosis.	5−25%
3	Moderate (+++)	Diffuse, significant inflammatory damage with noticeable necrosis.	25−50%
4	Severe (++++)	Extensive damage with confluent necrosis or architectural distortion.	>50%

Table Content: The table displays the individual scores for each animal (n=3 per group).

Liver			
	Pathological changes		
Samples	Hepatocyte edema	Inflammatory cell infiltration	Congestion
PBS	+	-	-
GAZY Fc_{WT}	++	-	+++
GAZY Fc_{3A}	++	-	++
GAZY Fc_{95}	++	-	+

Spleen		
	Pathological changes	
Samples	Inflammatory cell infiltration	Congestion
PBS	+	-
GAZY Fc_{WT}	++	-
GAZY Fc_{3A}	+++	+
GAZY Fc_{95}	++	-

1889

Kidney			
	Pathological changes		
Samples	Inflammatory cell infiltration	Renal tubular atrophy	Congestion
PBS	-	-	-
GAZY Fc_{WT}	+	-	-
GAZY Fc_{3A}	+	+	-
GAZY Fc_{95}	-	-	-

1890

1891

1892

1893

1894

1895

1896

1897

1898

1899

1900

1901

1902

1903

Table S4 Quantitative analysis of N-glycan species for Fc-engineered constructs.

Antibody variants	Core fucose (%)	Terminal galactose (%)	High mannose (%)	Total sialic acid (%)
Fc_{WT}	85.47	20.36	7.18	0.63
Fc_{3A}	64.53	8.19	15.52	0.28
Fc_{95}	13.85	9.61	81.2	0.69
Gazyva	41.3	30.33	4.75	0.7
MARV Fc_{LZ01}	3.78	5.03	3.48	0.35
$Fc_{3A+S239D}$	77.13	10.48	10.58	0.35
$Fc_{3A+F243L}$	18.52	10.66	75.11	0.87
$Fc_{3A+R292A}$	39.2	11.64	49.43	0.56
$Fc_{3A+Y300L}$	70.4	8.73	17.18	0.37

Note on Fc variants: Fc_{WT} and Fc_{3A} are fully fucosylated IgG1 (produced in standard CHO-S cells). Gazyva and MARV Fc_{LZ01} serve as afucosylated benchmarks (produced in FUT8-KO CHO-S cells). Fc_{95} is a sequence-engineered variant with an intrinsically low-fucose profile (~13.85%).

Supplementary Files

This is a list of supplementary files associated with this preprint. Click to download.

- SupplementaryTables.pdf
- Extendeddatafigures.docx
- Unprocessedoriginalimages.pdf